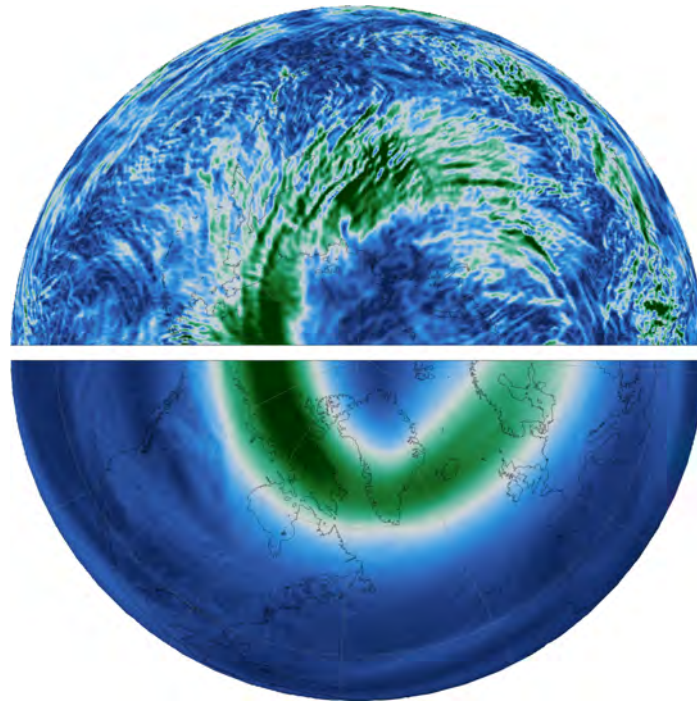# The Role of Inertia-Gravity Waves in the Atmospheric Energy Spectrum

Insights from Global Storm-Resolving Simulations

## Yanmichel Alejandro Morfa Avalos

Hamburg 2024

## Hinweis

## Anschrift / Address

## *Notice*

## *Layout*

## *Copyright*

# The Role of Inertia-Gravity Waves in the Atmospheric Energy Spectrum

Insights from Global Storm-Resolving Simulations

## Yanmichel Alejandro Morfa Avalos

Hamburg 2024

# Yanmichel Alejandro Morfa Avalos

aus Cienfuegos, Kuba

Max-Planck-Institut für Meteorologie
The International Max Planck Research School on Earth System Modelling (IMPRS-ESM)
Bundesstrasse 53
20146 Hamburg

Tag der Disputation: 12. Oktober 2023

Folgende Gutachter empfehlen die Annahme der Dissertation:
Prof. Dr. Claudia Stephan
Prof. Dr. Bjorn Stevens

Vorsitzender des Promotionsausschusses:
Prof. Dr. Hermann Held

Dekan der MIN-Fakultät:
Prof. Dr.-Ing. Norbert Ritter

In loving memory of Dr. Mario Carnesoltas Calvo

$(1948 - 2022)$



To my dear friend Mayito, in recognition of more than five decades of commendable work in advancing the field of atmospheric physics and inspiring me and several generations of meteorologists in Cuba.

# ABSTRACT

This dissertation investigates atmospheric kinetic energy spectra of horizontal and vertical motions and their relationships in global storm-resolving simulations. The kinetic energy spectrum of horizontal motions as a function of horizontal wavenumber $\kappa$ obeys canonical power laws. The synoptic scales ($\sim$ 10,000–1,000 km) are characterized by a rapid decrease of kinetic energy with horizontal wavenumber ($\kappa$) towards smaller scales following a $\kappa^{-3}$ power law, governed by quasigeostrophic (QG) turbulence theory, which predicts an upscale kinetic energy cascade with baroclinic instability acting as the primary energy source. At mesoscales (scales $\lesssim$ 600 km), the spectrum transitions to a shallower $\kappa^{-5/3}$ regime. However, the cause of the shallower mesoscale spectrum remains elusive and has motivated intensive research in the last decades. In contrast, vertical kinetic energy has been discussed much less, as measuring vertical velocity remains challenging. Several studies have reported vertical kinetic energy spectra almost white in horizontal wavenumber space with evidence of two maxima at synoptic scales ($\sim$ 2000 km) and mesoscales ($\sim$ 10 km), leaving the explanation of these maxima open.

The relationship between energy spectra of horizontal and vertical motions is investigated in global storm-resolving simulations from the DYAMOND experiment. The consistency of these relationships with linear inertia-gravity wave (IGW) theory is tested by diagnosing wind fluctuations associated with IGW modes. The results from partitioning the global circulation into IGW and balanced modes suggest vertical kinetic energy spectra are explained, to a good approximation, exclusively by horizontal winds associated with IGW fluctuations over a wide range of horizontal scales. Furthermore, it is shown that hydrostatic IGW polarization relations provide a quantitative prediction of the spectral slopes of vertical kinetic energy at large scales and mesoscales, where the intrinsic frequencies are inferred from the linearized vorticity equation. Moreover, model differences in the vertical velocity spectrum at mesoscales are explained consistently by the properties of resolved IGWs. Our results suggest that IGW modes dominate the vertical kinetic energy spectra at most horizontal scales, whereas an incompressible, isotropic scaling of the continuity equation captures the relationship between horizontal and vertical kinetic energy spectra at small scales.

The second part of this dissertation delves into the role of IGWs in the energy transfer processes shaping the mesoscale energy spectrum by investigating the spectral energy budget with unprecedented high resolution. We explore the different hypotheses to explain the mesoscale spectrum: direct forcing due to IGWs, a downscale cascade mediated by weakly nonlinear IGWs, strongly stratified turbulence, or interactions between IGWs and the mean flow. The analysis of energy conversions and vertical fluxes within the upper troposphere and the lower stratosphere reveals that these two layers exhibit different dynamics at mesoscales. The lower stratosphere is mainly energized by direct forcing due to vertically propagating IGWs, with a negligible HKE cascade and only a small direct forcing due to conversion from available potential energy to

divergent kinetic energy. The primary contribution to the mesoscale energy spectrum in the troposphere is from spectral transfers across scales, while the direct forcing of IGWs is limited. However, the normal mode decomposition of the atmospheric circulation into linear Rossby waves and IGWs suggests that interactions between IGWs and the balanced flow explain the nonlinear downscale energy cascade at mesoscales. This result aligns with the hypotheses that explain the downscale cascade based on triad interactions between vortical and gravity wave modes. Furthermore, it is shown that interacting wave modes do not contribute to the downscale energy transfer, challenging the hypothesis that the downscale cascade is due to weakly nonlinearly interacting IGWs.

## ZUSAMMENFASSUNG

Diese Dissertation untersucht atmosphärische kinetische Energiespektren horizontaler und vertikaler Bewegungen und ihre Beziehungen in globalen sturmauflösenden Simulationen. Das kinetische Energiespektrum horizontaler Bewegungen als Funktion der horizontalen Wellenzahl $\kappa$ gehorcht kanonischen Potenzgesetzen. Die synoptischen Skalen ($\sim$ 10.000–1.000 km) sind durch einen schnellen Abfall der kinetischen Energie mit der horizontalen Wellenzahl ($\kappa$) zu kleineren Längenskalen hin gekennzeichnet, der einem Potenzgesetz von $\kappa^{-3}$ folgt, wie beschrieben durch quasigeostrophische (QG) Turbulenztheorie, die eine kinetische Aufwärtskaskade vorhersagt, mit barokliner Instabilität als primärer Energiequelle. Auf Mesoskalen (Maßstäbe $\lesssim$ 600 km) geht das Spektrum in einen flacheren $\kappa^{-5/3}$-Bereich über. Die Ursache des flacheren mesoskaligen Spektrums bleibt jedoch unklar und hat in den letzten Jahrzehnten zu intensiver Forschung geführt. Im Gegensatz dazu wurde die vertikale kinetische Energie viel weniger diskutiert, da die Messung der vertikalen Geschwindigkeit weiterhin eine Herausforderung darstellt. Mehrere Studien haben berichtet, dass vertikale kinetische Energiespektren im horizontalen Wellenzahlraum fast weiß sind, mit Hinweisen auf zwei Maxima auf synoptischen Skalen ($\sim$ 2000 km) und Mesoskalen ($\sim$ 10 km), wobei die Erklärung dieser Maxima offen bleibt.

Der Zusammenhang zwischen Energiespektren horizontaler und vertikaler Bewegungen wird in globalen sturmauflösenden Simulationen des DYAMOND-Experiments untersucht. Die Konsistenz dieser Beziehungen mit der linearen IGW-Theorie wird durch die Diagnose von Windschwankungen im Zusammenhang mit IGW-Modi getestet. Die Ergebnisse der Zerlegung der globalen Zirkulation in IGW- und balancierte Modi legen nahe, dass vertikale kinetische Energiespektren in guter Näherung ausschließlich durch horizontale Winde erklärt werden, die mit IGW-Fluktuationen über einen weiten Bereich horizontaler Skalen verbunden sind. Darüber hinaus wird gezeigt, dass hydrostatische IGW-Polarisationsbeziehungen eine quantitative Vorhersage der spektralen Steigungen der vertikalen kinetischen Energie auf großen Skalen und Mesoskalen ermöglichen, wobei die Eigenfrequenzen aus der linearisierten Vorticity-Gleichung abgeleitet werden. Darüber hinaus werden Modellunterschiede im vertikalen Geschwindigkeitsspektrum auf Mesoskalen konsistent durch die Eigenschaften aufgelöster IGWs erklärt. Unsere Ergebnisse legen nahe, dass IGW-Moden die vertikalen kinetischen Energiespektren auf den meisten horizontalen Skalen dominieren, wohingegen eine

inkompressible, isotrope Skalierung der Kontinuitätsgleichung die Beziehung zwischen horizontalen und vertikalen kinetischen Energiespektren auf kleinen Skalen erfasst.

Der zweite Teil dieser Dissertation befasst sich mit der Rolle von IGWs bei den Energieübertragungsprozessen, die das mesoskalige Energiespektrum prägen, indem das atmosphärische spektrale Energiebudget mit noch nicht da gewesener horizontaler Auflösung untersucht wird. Wir untersuchen die verschiedenen Hypothesen, um das mesoskalige Spektrum zu erklären: direkter Antrieb aufgrund von IGWs, eine durch schwach nichtlineare IGWs vermittelte Abwärtskaskade, stark geschichtete Turbulenz oder Wechselwirkungen zwischen IGWs und der mittleren Strömung. Die Analyse der Energieumwandlungen und vertikalen Flüsse innerhalb der oberen Troposphäre und der unteren Stratosphäre zeigt, dass diese beiden Schichten auf Mesoskalen unterschiedliche Dynamik aufweisen. Die untere Stratosphäre wird hauptsächlich durch direkten Antrieb aufgrund sich vertikal ausbreitender IGWs mit Energie versorgt, mit einer vernachlässigbaren HKE-Kaskade und nur einem geringen direkten Antrieb aufgrund der Umwandlung von verfügbarer potenzieller Energie in divergente kinetische Energie. Der Hauptbeitrag zum mesoskaligen Energiespektrum in der Troposphäre erfolgt durch skalenübergreifende Spektralübertragungen, während der direkte Antrieb von IGWs begrenzt ist. Die Normalmoden-Zerlegung der atmosphärischen Zirkulation in lineare Rossby-Wellen und IGWs legt jedoch nahe, dass Wechselwirkungen zwischen IGWs und der balancierten Strömung die nichtlineare Energiekaskade auf der Mesoskala erklären. Dieses Ergebnis stimmt mit den Hypothesen überein, die die Abwärtskaskade basierend auf Triadenwechselwirkungen zwischen Wirbel- und Schwerewellenmodi erklären. Darüber hinaus wird gezeigt, dass wechselwirkende Wellenmoden nicht zur Abwärtskaskade beitragen, was die Hypothese in Frage stellt, dass die Abwärtskaskade auf schwach nichtlinear interagierende IGWs zurückzuführen ist.

# CONTENTS

## ACRONYMS

**DYAMOND** DYnamics of the Atmospheric general circulation Modeled On Non-hydrostatic Domains

**ICON** ICOsahedral Nonhydrostatic model

**GEOS** Goddard Earth Observing System

**NICAM** Nonhydrostatic ICosahedral Atmospheric Model

**ERA5** Fifth-generation ECMWF Atmospheric Reanalysis

**IFS** Integrated Forecasting System

# LIST OF PUBLICATIONS

Morfa, Yanmichel A. and Claudia C. Stephan (2023). "The Relationship between Horizontal and Vertical Velocity Wavenumber Spectra in Global Storm-Resolving Simulations." In: *Journal of the Atmospheric Sciences* 80.4, pp. 1087 –1105. DOI: https://doi.org/10.1175/JAS-D-22-0105.1. URL: https://journals.ametsoc.org/view/journals/atsc/80/4/JAS-D-22-0105.1.xml.

Morfa, Yanmichel A. and Claudia C. Stephan (to be submitted). "Spectral Energy Budget of the Atmosphere in Global Storm-Resolving Simulations." In: *Journal of the Atmospheric Sciences*.

# 1 | INTRODUCTION

*Mathematicians seem to have no difficulty
creating new concepts faster than the old ones
become well-understood.*

— Edward Lorenz (1991)

## 1.1 THE SPECTRUM OF HORIZONTAL KINETIC ENERGY

Atmospheric motions span a wide range of horizontal scales, from large-scale geostrophically balanced flows and long atmospheric waves to three-dimensional turbulent dissipation scales. The kinetic energy spectrum of horizontal motions as a function of horizontal wavenumber $\kappa$ obeys canonical power laws (Gage, 1979; VanZandt, 1982; Nastrom and Gage, 1985). This spectrum consists of a shallow-sloped region at global scales ($\sim$ 40,000–10,000 km), a steeper-sloped $\kappa^{-3}$ regime at synoptic scales, and the mesoscale regime, where the spectrum transitions to a shallower slope that closely approximates a power law of $\kappa^{-5/3}$ at scales of $\sim$ 600 km (Nastrom et al., 1984; Nastrom and Gage, 1985; Lindborg, 1999). The canonical shape of the atmospheric kinetic energy spectrum is illustrated in Fig. 1.1. The prevailing explanation for what shapes the $\kappa^{-3}$ portion rests on applications of quasigeostrophic (QG) turbulence theory, which shows that this region of the spectrum is consistent with a downscale enstrophy cascade (Charney, 1971). The cause of the $\kappa^{-5/3}$ dependence of the horizontal kinetic energy spectrum within the mesoscales (scales $\lesssim$ 600 km) in the upper troposphere and lower stratosphere is still uncertain. The shape of atmospheric energy spectra is not just of theoretical interest but has practical implications for atmospheric predictability. Lorenz (1969) proposed that a turbulent flow with $\kappa^{-5/3}$ has a finite predictability limit, which means that more accurate knowledge of the initial state cannot improve forecasts significantly. However, if the mechanism underlying the energy spectrum is linear gravity waves, predictability may not be limited by power-law characteristics alone (Malardel and Wedi, 2016) since linear gravity waves do not propagate errors in the same way as turbulent flows (Callies et al., 2014). Another practical implication is that the small-scale end of the mesoscale is not resolved in numerical weather prediction models; therefore, part of the cascade must be parameterized. However, parameterizations require an understanding of the dynamics, which needs to be improved.

The competing hypotheses to explain the mesoscale spectrum generally fall into two main categories: First, the mesoscale is treated as an inertial subrange with the existence of an energy cascade. However, the underlying dynamics of this cascade still

need to be fully understood. Dewan (1979) first suggested that a superposition of weakly nonlinear Inertia-Gravity Waves (IGWs) dominates the mesoscale energy. Later, Dewan (1997) proposed that wave saturation and cascade can explain the spectral slopes of horizontal and vertical velocity fluctuations and those of temperature and density. Conversely, other studies interpreted the mesoscale range to be predominantly turbulent. Gage (1979) first proposed two-dimensional turbulence (2DT) to explain the $\kappa^{-5/3}$ power law in lower stratospheric horizontal wavenumber spectra via an upscale energy cascade. Lilly (1983) later predicted that the three-dimensional isotropic turbulence roughly divides equally into waves and 2DT in the presence of strong stratification and suggested that deep convection may be a viable source for the inverse cascade. However, many attempts to simulate an inverse energy cascade in stratified turbulence have failed (e.g., Waite and Bartello, 2004; Lindborg, 2006). Waite and Bartello (2004) found that vortical energy transfers forward in significant quantities rather than cascading upscale. Later Tung and Orlando (2003), introduced the idea of a double downscale enstrophy and energy cascade as a result of QG turbulence, where the downscale cascade is "hidden" by the dominant upscale cascade at large scales and shows up at a particular wavenumber (see Fig. 1.1). Lindborg (2006) introduced the hypothesis of stratified turbulence with a forward (downscale) energy cascade supported by idealized simulations. The second type of hypothesis suggests that the mesoscale is energized due to a direct forcing of gravity waves, with no explicit mention of a cascade, where the geostrophic flow and IGWs do not interact strongly (Callies et al., 2014; Callies et al., 2016). IGWs are ubiquitous and can be generated by various processes, e.g., deep moist convection, orography, baroclinic jet streams, and frontal systems (Fritts and Alexander, 2003), and then dissipated on small scales by shear instabilities (Dewan, 1997). Although a single mechanism is unlikely to dominate the mesoscale dynamics in the entire vertical extent of the atmosphere, explanations that solely rely on IGWs are more likely to be applicable in the stratosphere. Recent studies point to the non-universality of mesoscale dynamics and the associated horizontal kinetic energy spectrum based on the height dependence of the relative magnitudes of rotational and divergent kinetic energies (Bierdel, 2017).

An alternative interpretation of the shape of the mesoscale energy spectrum is that it emerges from interactions between different dynamics of balanced circulations and IGWs; however, there is still debate about whether these interactions are weakly (Dewan and Good, 1986) or strongly nonlinear (Li and Lindborg, 2018). Lelong and Riley (1991) identified that resonant triadic interaction involving two wave modes and a geostrophic mode could facilitate a downscale energy cascade, where the rotational mode is left unaffected, thus acting as a catalyst. Bartello (1995) suggested that this wave-vortex resonant interaction provides the mechanism for geostrophic adjustment via a downscale cascade of wave energy. The numerical evidence of the downscale cascade-based hypothesis dominating the tropospheric mesoscale is increasing (Cho and Lindborg, 2001; Augier and Lindborg, 2013; Li et al., 2023). A possible explanation by Kafiabad et al. (2019) suggests that the scattering of IGWs by a stationary turbulent geostrophic flow, which results in a cascade of IGW energy to small scales producing a $\kappa^{-2}$ scaling, nearly consistent with observed atmospheric mesoscale spectrum. Cox et al. (2023) recently showed that such a $\kappa^{-2}$ spectrum also arises even when the assumption of stationarity is relaxed, i.,e for a more realistic, slowly evolving background flow. A

complete explanation for the mesoscale spectrum ultimately requires separating the flow into waves and vortices, but how?
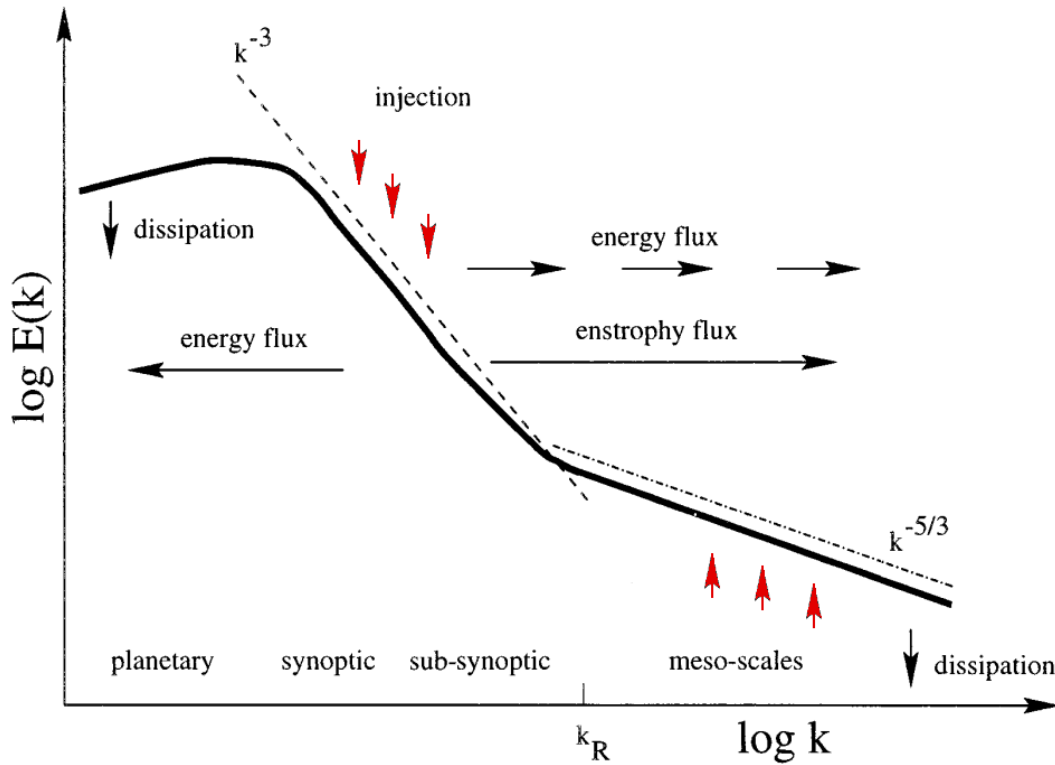


**Figure 1.1:** Schematic of canonical atmospheric kinetic energy spectra. Horizontal arrows denote horizontal energy fluxes by different mechanisms (see text). Red upward/downward arrows denote local energy injection. The Rossby deformation wavenumber is shown as $\kappa_R$, which closely approximates the transition scale to the mesoscale regime. Modified from Tung and Orlando (2003)

## 1.2 UNTANGLING WAVES AND TURBULENCE

The governing equations of atmospheric motions, including the effects of rotation and stratification, have two distinct linear modes of motion: IGWs and vortices (Waite, 2020). IGWs are higher-frequency motions propagating in a stably stratified fluid with time scales of the order of hours. In contrast, weather systems in the atmosphere, with an evolutionary time scale of several days, are a familiar example of geostrophic turbulence. The atmospheric variability is often investigated by performing a time-scale separation of the circulation into fast and slow dynamics. The fast dynamics are considered unbalanced since they are mainly associated with wave-like motions. The standard definition of a balanced flow imposes a functional relation between the three-dimensional velocity field and the mass field (McIntyre, 2015), with the well-known quasigeostrophic balance as a prime example. The fast variables will generally comprise both slow and fast (unbalanced) dynamical components. The time-scale separation is only asymptotic since balanced and unbalanced motions can become strongly coupled. An example of such coupling relation is the well-known

quasigeostrophic omega equation (e.g., Holton, 2004), which relates the vertical velocity (and thus the horizontal divergence, a fast variable) to the slow dynamics. However, the degree of separation of the fast and slow dynamics in realistic regimes can be remarkable (Stephan et al., 2021b). The spatial scale separation between balanced and unbalanced motions is a much more challenging problem given their complex multiscale nature (McIntyre, 2008; Young, 2021).

Linear methods for identifying waves and vortices include Helmholtz decomposition (explained in more detail in section 2.2.2) of the circulation and separating the velocity and temperature into linear wave and vortical modes, e.g., Bartello (1995). Further, linear normal mode function (NMF) decompositions separate the flow into IGWs and Rossby waves (e.g., Kasahara and Puri, 1981; Žagar et al., 2015). Linear decompositions of the mesoscale spectrum have been performed for models (e.g., Skamarock et al., 2014) and one-dimensional aircraft data (Callies et al., 2016; Li and Lindborg, 2018). According to these studies, the mesoscale energy spectrum in the upper troposphere has an equal amount of linear wave and vortical energy, which rules out the possibility of a cascade that relies solely on waves (Li and Lindborg, 2018). However, linear decompositions are limited in accurately untangling waves from turbulence mainly because waves can have divergent and rotational components, and nonlinear high-order balances might be relevant. For example, QG vortices have a small balanced ageostrophic flow, which linear methods incorrectly attribute to waves.

The interpretation of the mesoscale spectrum in the lower stratosphere based on linear wave-vortex decompositions of the circulation reveals a clear picture: IGWs dominate the spectrum at these altitudes over the balanced rotational modes, corroborated by studies that explicitly diagnose linear IGWs modes based on normal-mode function decomposition (Kitamura and Matsuda, 2010; Terasaki et al., 2011; Žagar et al., 2015) or use divergent kinetic energy to approximate IGWs in the mesoscale (Callies et al., 2014; Skamarock et al., 2014; Bierdel et al., 2016). However, caution must be taken due to the linearity of these decompositions because nonlinear balances of the ageostrophic flow can cause a non-negligible fraction of energy to project onto linear IGW modes. Wang and Bühler (2020) incorporated weakly nonlinear ageostrophic corrections into the linear wave-vortex decomposition from one-dimensional aircraft measurements using a statistical QG omega equation and showed that the wave interpretation of the lower stratosphere is reliable since the IGW modes are robust to nonlinear effects. The interpretation of wave-vortex decompositions in the troposphere is more controversial than in the stratosphere and requires further attention (Waite, 2020); nevertheless, recent evidence points away from the wave-based cascade since balanced rotational modes are of equal or higher importance than IGWs (Callies et al., 2014; Skamarock et al., 2014; Hamilton et al., 2008; Lindborg, 2015). This equipartition of wave and vortex energy is predicted by strongly stratified turbulence (Lindborg, 2006). However, numerical evidence shows that the kinetic-to-potential energy ratio deviates from expectations based on waves or turbulence theories alone, suggesting other types of motion as the dominant mesoscale mechanism. As argued by Wang and Bühler (2020), understanding the vertical velocity spectrum might be the definitive clue to solving the riddle of the mesoscale energy spectrum.

## 1.3 THE SPECTRUM OF VERTICAL KINETIC ENERGY

Vertical motions play a crucial role in atmospheric dynamics and are essential for understanding the conversion mechanism between potential and kinetic energies maintaining the large-scale atmospheric circulation (Lorenz, 1960; Chen and Wiin-nielsen, 1975). Although the magnitude of mean vertical motion is small compared to horizontal motions on most scales, it is crucial in determining cloud formation likelihood (Vogel et al., 2020; George et al., 2021). For example, vertical transport of momentum and moisture is essential in determining cloud field properties on tens to hundreds of kilometers scales. For this reason, it is desirable to understand how vertical velocity variance is distributed across horizontal scales. Compared to the horizontal kinetic energy spectrum, the distribution of vertical kinetic energy with horizontal scales has been studied much less and has not been observed beyond a few tens of kilometers (Bacmeister et al., 1996; Callies et al., 2016; Schumann, 2019). The main reason is the need for observations with sufficient spatial coverage of the mesoscales and the prevalence of significant measurement uncertainties. As pointed out by Bony and Stevens (2019), measuring large-scale vertical motions in the atmosphere remains one of the greatest observational challenges in atmospheric science.

Several numerical studies have reported broadband horizontal spectra of the vertical velocity field almost flat in wavenumber space (Terasaki et al., 2009; Skamarock et al., 2014). Observational evidence further shows vertical kinetic energy spectra relatively flat at mesoscales with a local maximum at scales of about 10 km (Schumann, 2019). A random spatial distribution of updrafts/downdrafts has an associated spectrum that roughly corresponds to the spectrum of white noise. However, convective updrafts do not occur in isolation and might only account for the vertical kinetic energy magnitude at small scales, which means that the explanation of the relative flatness of the spectra across multiple scales is much more complex. Furthermore, the energy exchange between horizontal and vertical motions might be more critical for the kinetic energy spectra than small-scale sources such as moist convection or sinks of kinetic energy through turbulent dissipation.

### 1.3.1 Large scales

Global storm-resolving simulations show that the vertical velocity spectrum peaks at synoptic scales (Terasaki et al., 2009; Skamarock et al., 2014; Polichtchouk et al., 2022). Skamarock et al., 2014 suggested that the synoptic-scale peak in the vertical kinetic energy spectra is related to vertical motions associated with large-scale waves. Possible explanations include vertical motions associated with spontaneously generated large-scale IGWs from imbalances around the balanced flow through geostrophic adjustment, orographically generated waves, and mid-latitude baroclinic waves. Polichtchouk et al., 2022 revealed that most of the large-scale vertical velocity variance is owing to the extratropical region based on global simulations. However, validating this feature with observations is unattainable. Section 3.4.1 attempts to explain the large-scale features of the vertical velocity spectrum from the perspective of linear wave theory and QG scaling arguments.

### 1.3.2 Mesoscales

Bony and Stevens (2019) observed long-lived wave-like variability in vertical profiles of mesoscale divergence computed from dropsonde measurements of horizontal winds over the tropical Atlantic during the NARVAL2 campaign. Later, the EUREC$^4$A campaign of 2020 (Stevens et al., 2021) included an extensive radio-sounding network composed of a station on the island of Barbados and four ships (Stephan et al., 2021a). These studies diagnosed vertical velocities averaged at scales of approximately 200 km by solving mass continuity. They found variability in vertical motion on vertical scales from 1 to 2 km and surprisingly large amplitudes four times larger than estimates of radiatively driven subsidence (defined as $w = \dot{Q}/\Delta\Gamma$, where $\Delta\Gamma$ is the difference between the actual and dry adiabatic lapse rates, and $\dot{Q}$ is the clear-sky atmospheric radiative cooling), a conventional assumption in the tropics. The large spatiotemporal variability of vertical motions has been reproduced from high-resolution simulations and demonstrated to agree with the observations (Bony and Stevens, 2019). Figure 1.2 illustrates vertical profiles of large-scale mass divergence and vertical velocity during the NARVAL2 measurements calculated from limited-area simulations with ICON using 1.25 km resolution described by Klocke et al. (2017). Note that the amplitude of the horizontal divergence increases with height above 500 hPa, which could be consistent with the growth of wave amplitudes with altitude due to energy conservation (Fritts and Alexander, 2003).
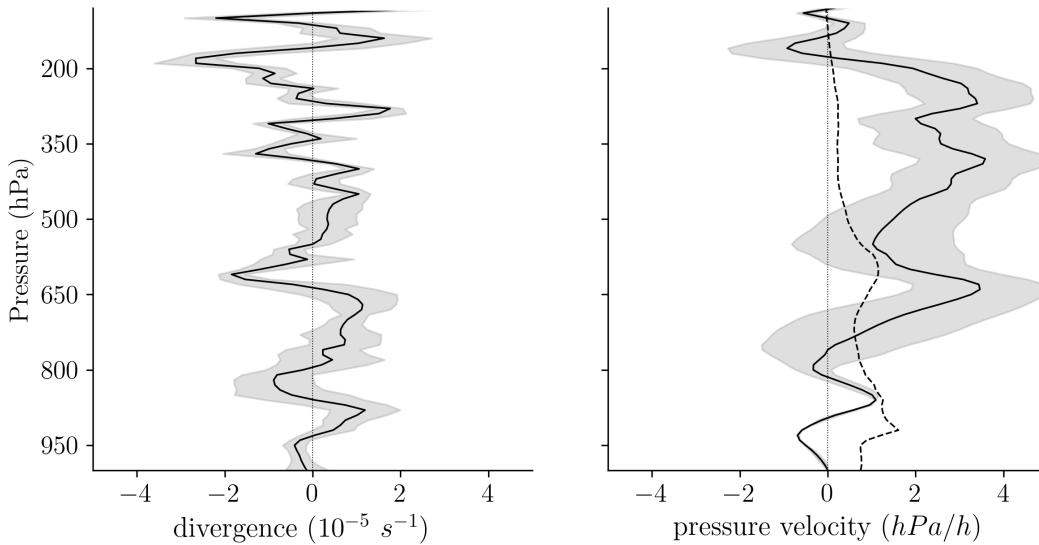


**Figure 1.2:** Time-averaged vertical profiles of (left) large-scale mass divergence and (right) vertical velocity estimated from NARVAL2 simulation with ICON corresponding to August 12, 2016. The dashed line represents the radiatively driven vertical velocity. The shading represents the temporal standard deviation.

Craig and Selz (2018a) suggests that the weak temperature gradient approximation has the potential to define a balance principle for the mesoscale, where heat sources directly force the divergent flow, most importantly convection, giving the dominant contribution to the vertical velocity spectrum. Numerical studies of the response of the stratified atmosphere to heating (Alexander and Holton, 2004; Holton et al., 2002) suggest that many of these features could be compatible with large-scale IGWs. Stephan

and Mariaccia (2021a) demonstrated that observed divergence magnitudes during EUREC[4]A scaled consistently with the wavenumber dependence of the global IGW energy spectrum. Linear gravity wave theory provides predictions of the relationships between the horizontal and vertical motion spectra in the horizontal wavenumber domain. Since the relationship between the shapes and magnitude of the spectra of horizontal and vertical motions are known in the context of IGW theory (Dewan, 1997), the consistency of vertical velocity spectrum with the known horizontal velocity spectrum becomes a test of the concept that IGWs dominate the mesoscale spectrum (Nastrom and Gage, 1985). Ecklund et al. (1986) showed that the vertical velocity frequency spectra under low horizontal wind conditions represent a nearly universal spectrum of IGWs unambiguously. The relationships between these spectra in the horizontal wavenumber domain were tested recently by Schumann (2019), using aircraft observations. They showed that the vertical and horizontal kinetic energy spectra are linked kinematically, where an incompressible, isotropic scaling of the continuity equation captures this relationship at mesoscales. These results suggest that energy exchange between horizontal and vertical motions is far more critical for the mesoscale spectrum than small-scale turbulent dissipation. Similar models of the vertical kinetic energy spectrum have been discussed in previous studies (e.g., Peltier et al., 1996; Tong and Nguyen, 2015). Schumann (2019) argued that the magnitude of vertical velocity spectra is inconsistent with the prediction of IGW theory; however, a limitation of these results is that the IGW energy is approximated using the divergent component of the flow, which results in the underestimation of the IGW energy. Chapter 3 investigates the relationship between horizontal and vertical motion spectra using global storm-resolving simulations from different state-of-the-art GCMs by explicitly diagnosing the associated vertical velocities of IGWs and Rossby waves.

## 1.4 RESEARCH QUESTIONS AND OBJECTIVES

This dissertation poses the following research questions:

1. **What is the role of IGWs in the dynamic coupling of horizontal and vertical velocity wavenumber spectra?**

   Several numerical studies have revealed the energy spectrum of vertical velocity to be broadband and nearly flat across horizontal wavenumber space, with evidence of two maxima at synoptic scales and mesoscales (Terasaki et al., 2009; Skamarock et al., 2014). Observational evidence has corroborated the mesoscale vertical kinetic energy spectrum peaking at the smallest resolved scales (Schumann, 2019). The shape of the vertical velocity spectrum has implications for the vertical transport of energy and momentum; however, the cause of its spectral characteristics remains unclear. Linear gravity wave theory predicts the relationship between the shapes and magnitude of the spectra of horizontal and vertical motions. Chapter 3 investigates whether different kilometer-scale global GCMs agree on the predictions of two simplified semi-empirical models linking vertical and horizontal motion spectra at large scales and mesoscales through IGW polarization and dispersion relations. The resolved vertical velocity spectrum is compared to the vertical velocity spectrum associated with the

balanced flow that projects onto the low-frequency linear Rossby modes and the unbalanced component related to IGWs. The vertical motions associated with balanced and unbalanced circulations are explicitly diagnosed from horizontal winds of the inverse fields calculated using the normal mode decomposition described by Žagar et al. (2015). Furthermore, we examine whether resolved IGWs' properties are relevant for the dynamic coupling of vertical and horizontal motion spectra. To investigate this coupling at mesoscales, we build on the work of Schumann (2019), who introduced a hypothesis that connects vertical and horizontal divergent motions by mass continuity at mesoscales and converges toward locally isotropic gravity wave or turbulence dynamics at small scales.

2. **What is the role of resolved IGWs in the energy transfer processes shaping the mesoscale energy spectrum in global storm-resolving simulations?**

Numerical and observational evidence points to the dominant role of IGWs in the dynamics of the mesoscale energy spectrum in the stratosphere. In contrast, the mesoscale spectrum in the free troposphere seems consistent with a downscale kinetic energy cascade; however, the underlying mechanisms remain unclear. Some studies suggest that the downscale cascade emerges from interactions between rotational and gravity wave modes; however, there is still debate about whether these interactions are weakly (Dewan and Good, 1986) or strongly nonlinear (Li and Lindborg, 2018). Chapter 4 addresses this question by systematically investigating the dynamics that shape the horizontal kinetic energy spectrum in different kilometer-scale global GCMs. For this purpose, we compute resolved mesoscale fluxes and energy transfers employing the formulation of the spectral energy budget developed by Augier and Lindborg (2013). The contributions of rotational and divergent modes to the spectral budget of kinetic energy are investigated following the methodology proposed by Li et al. (2023). The analysis presented here does not suffer from the limitations of previous studies of resolved mesoscale fluxes with coarser resolutions, which could not resolve mesoscale dynamics, especially gravity waves. Furthermore, we explore the impact of resolved gravity waves on the mesoscale spectral energy transfers.

# 2 | DATA AND METHODS

## 2.1 DYAMOND

To investigate the dynamics of horizontal and vertical kinetic energy spectra, we analyze numerical outputs from high-resolution global simulations of four different model members of the DYnamics of the Atmospheric general circulation Modeled On Non-hydrostatic Domains (DYAMOND) experiment (Stevens et al., 2019). The DYAMOND experiment is the first intercomparison project of global storm-resolving models (GSRMs) which consists of two phases of simulations, referred to as "summer" and "winter" respectively, each spanning forty days and forty nights. The horizontal grid spacing of the models is < 5 km. Most DYAMOND models solve the Navier-Stokes system of compressible equations, except for the IFS (Integrated Forecasting System), which uses primitive hydrostatic equations. The numerical methods employed by the different models to solve their governing equations depend on the choice of the grid and the time integration methods and therefore vary considerably. The advantage of using DYAMOND-type models is that these models are global while resolving deep convection explicitly. Figure 2.1 shows a snapshot of ICON simulations with 2.5 km resolution corresponding to the winter experiment; notably, the simulated cloud fields exhibit rich mesoscale variability and a high degree of realism.

We use numerical outputs from the ICOsahedral Nonhydrostatic model (ICON) model (Zängl et al., 2015), the Goddard Earth Observing System (GEOS) (Putman and Suarez, 2011), the Nonhydrostatic ICosahedral Atmospheric Model (NICAM) (Satoh et al., 2008), and the Integrated Forecasting System (IFS) (Wedi, 2014) with horizontal resolutions of 2.5, 3.3, 3.5, and 4.0 km, respectively. Detailed information about the model configurations can be found in Stevens et al. (2019). We analyze winter simulations initialized at 0000 UTC on January 20, 2020. Our analysis period spans 12 days, starting February 1, 2020. We use 6-hourly outputs ten days after initialization to exclude the model spin-up period. This period well exceeds previous estimates of spin-up time based on numerical models and theory (Skamarock, 2004; Hamilton et al., 2008) and ensures that the energy spectra are in equilibrium. Preparing the numerical

outputs of the models for analysis consists of averaging the models' three-dimensional wind fields within a target grid cell. The target grid is a regular Gaussian grid with 8192 by 4096 grid cells in the zonal and meridional direction, corresponding to a horizontal grid spacing of approximately 4.88 km at the Equator. In the analysis of section 3.2, no vertical interpolation of model outputs is performed before the kinetic energy spectra computation. Instead, we select the model levels closest to the level of interest, a reasonable approximation in the stratosphere, where model levels correspond to constant height surfaces in ICON and NICAM and constant pressure surfaces in IFS and GEOS. As noted by Skamarock et al. (2014), kinetic energy spectra computed on surfaces of constant height and pressure have the same qualitative character.

To explore the resolved energy fluxes at mesoscales in chapter 4, we analyzed a set of DYAMOND high-resolution simulations with ICON and the IFS models initialized on January 20, 2020, with horizontal resolutions of approximately 2.5 and 4.0 km, respectively. The analysis fields consist of 3-hourly outputs of instantaneous horizontal and vertical velocities, temperature, and dynamic tendencies corresponding



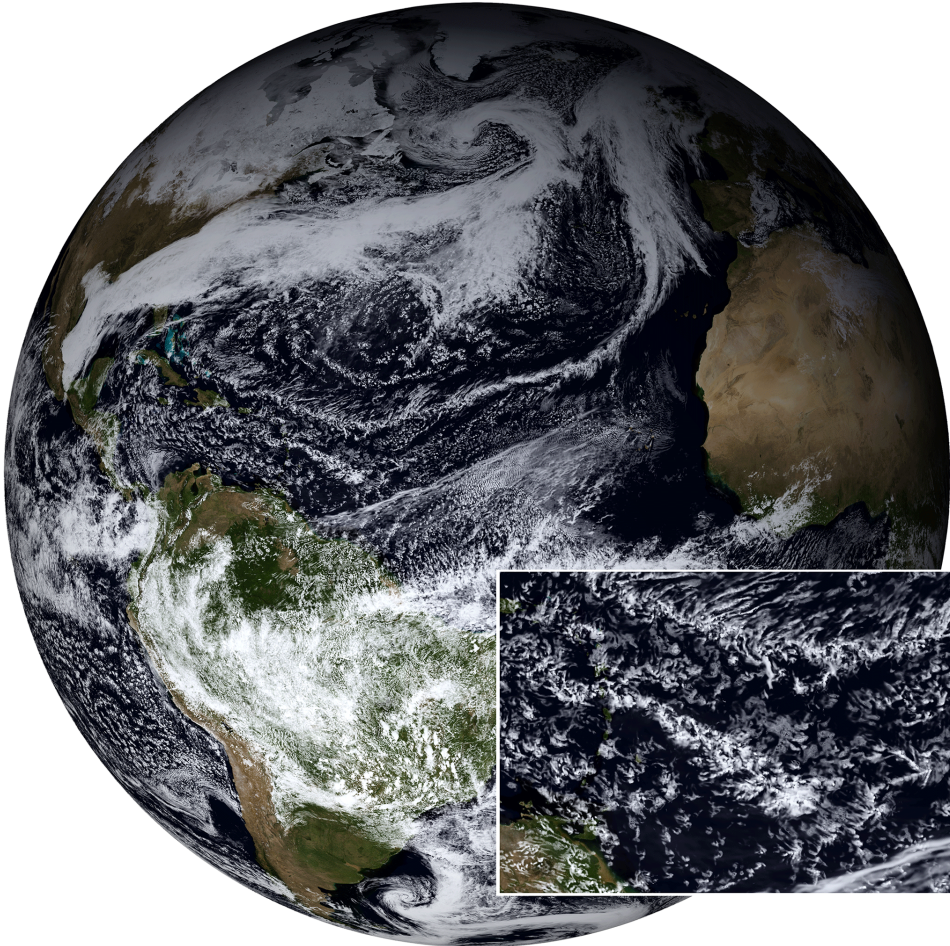**Figure 2.1:** Global storm-resolving simulation performed by ICON with 2.5 km horizontal resolution corresponding to DYAMOND-Winter for the EUREC$^4$A period. The Snapshot was taken on February 2, 2020, with a magnification over the EUREC$^4$A region. From Stevens et al. (2021).

to five days starting from January 25, 2020, sampled on constant pressure levels from 1000 hPa to 50 hPa. The model results are compared to the Fifth-generation ECMWF Atmospheric Reanalysis (ERA5) dataset covering the same analysis period. The global reanalysis data can resolve the atmospheric energy transfers across many scales; however, it is insufficient to investigate the whole mesoscale range due to limited horizontal resolution. ERA5 data is sampled on a regular latitude–longitude, with a horizontal resolution of $0.25°$ by $0.25°$.

**Data availability.** The DYAMOND simulations can be accessed at the project website https://www.esiwace.eu/services/dyamond-initiative. ERA5 hourly data on pressure levels from 1979 to the present is openly available from the Climate Data Store (CDS) at https://cds.climate.copernicus.eu.

## 2.2 SPECTRAL ANALYSIS OF GLOBAL SIMULATIONS

### 2.2.1 Spherical harmonics

Spherical harmonics analysis lies at the core of this work since it provides an effective tool to investigate the variability of global atmospheric circulation as a function of horizontal scales. This section briefly introduces some concepts and the notation used throughout the study. The spherical harmonics expansion of any square-integrable function ($f$) can be expressed as

$$f(\lambda, \phi) = \sum_{l=0}^{\infty} \sum_{m=-l}^{l} f_{lm} Y_{lm}(\lambda, \phi) \tag{2.1}$$

where $l$ is the spherical harmonic degree or total wavenumber, $m$ is the zonal wavenumber, $\lambda$ is longitude and $\phi$ is latitude. The spherical harmonic coefficients $f_{lm}$ are obtained by inverting (2.1), i.e, projecting $f(\lambda, \phi)$ in a triangularly truncated series of spherical harmonics basis functions $Y^{lm} = P_{lm} e^{im\lambda}$, where $P_{lm}$ are the Legendre polynomials; for details see Baer (1972). The power spectrum of $f(\lambda, \phi)$ is defined in terms of the spectral coefficients as $F_{lm} = C_m \text{Re}\{f_{lm}^* f_{lm}\} = |f_{lm}|^2$, where the asterisk denotes the complex conjugates. The normalization factor $C_m = 2 - \delta_{m0}$ is used in real spherical harmonics, where $\delta_{m0} = 1$ for $m = 0$, and $\delta_{m0} = 2$ for $m > 0$. The power spectrum is normalized to satisfy Parseval's theorem in spherical coordinates, which relates the global integral of the squared function to the sum of the squared harmonic coefficients, i.e., $\int |f(\lambda, \phi)|^2 = \sum_{l,m \geq 0}^{l} |f_{lm}|^2$.

The global mean of the product of any two scalar functions $a$ and $b$ can be written following Augier and Lindborg (2013), as

$$\langle ab \rangle = \sum_{l \geq 0} \sum_{|m| \leq l} (a, b) \tag{2.2}$$

where the operator $(a, b)$ denotes the cross-spectrum defined as $(a, b)_{lm} = C_m \text{Re}\{a_{lm}^* b_{lm}\}$. For example, the horizontal spectrum of vertical kinetic energy per

unit mass is expressed in terms of the spherical harmonics coefficients of vertical velocity as $E_w(l) = (w, w)_{lm} = |w_{lm}|^2/2$. The spherical harmonic coefficients of all analysis fields in this study are calculated using the high-performance library for Spherical Harmonic Transform SHTns (Schaeffer, 2013). Since we are not interested in dissipative scales (motions under-resolved by the models) related to the model filters, we analyze spectra with a triangular truncation at the spherical wavenumber $l = 2048$ (horizontal wavelengths $\lambda_h \sim 20$ km). The transform is exact up to spherical wavenumber $l_{max} = N - 1 = 2047$, where $N$ is the number of latitude points of the Gaussian grid.

### 2.2.2 Helmholtz decomposition

The global mean of the scalar product of two horizontal vector fields $\langle \mathbf{a} \cdot \mathbf{b} \rangle$ can be written in a similar form to (2.2); considering that spherical harmonic basis functions $Y_{lm}$ are the eigenfunctions of the horizontal Laplace operator, i.e., $|\nabla_h|^2 Y_{lm} + l(l+1)Y_{lm}/r^2 = 0$; it follows that

$$(\mathbf{a}, \mathbf{b})_{lm} = \frac{r^2}{l(l+1)} C_m \operatorname{Re}\{\operatorname{rot}_h(\mathbf{a})^*_{lm} \operatorname{rot}_h(\mathbf{b})_{lm} + \operatorname{div}_h(\mathbf{a})^*_{lm} \operatorname{div}_h(\mathbf{b})_{lm}\} \qquad (2.3)$$

where the operators $\operatorname{rot}_h(\cdot) = \nabla_h \times (\cdot)$ and $\operatorname{div}_h(\cdot) = \nabla_h \cdot (\cdot)$ are the horizontal curl and divergence respectively, and $r$ is the earth's radius (Lambert, 1984).

The spectrum of horizontal kinetic energy (HKE) per unit mass can be defined using (2.3) from the horizontal wind $\mathbf{u}$ as

$$E_h^{lm} = \frac{1}{2}(\mathbf{u}, \mathbf{u})_{lm} = \frac{r^2}{2l(l+1)}(|\hat{\zeta}_{lm}|^2 + |\hat{\delta}_{lm}|^2) \qquad (2.4)$$

$\zeta_{lm}$ and $\delta_{lm}$ are the spherical harmonics coefficients of vertical vorticity and horizontal divergence, respectively. The definition presented in (2.3) and (2.4) give a natural decomposition of the horizontal kinetic energy into its fully rotational and divergent components known as Helmholtz decomposition. In physical space, this decomposition yields.

$$\mathbf{u} = \mathbf{u}_R + \mathbf{u}_D = \nabla_h \times (\psi \mathbf{e}_z) + \nabla_h \chi \qquad (2.5)$$

where $\mathbf{e}_z$ is the upward (radial) unit vector; the horizontal wind is linearly split into its non-divergent ($\mathbf{u}_R$) and non-rotational ($\mathbf{u}_D$) components expressed in terms of two scalar functions, the streamfunction $\psi$ and the velocity potential ($\chi$), which in turn relate to the vertical vorticity and horizontal divergence as $\zeta = \nabla_h^2 \psi$ and $\delta = \nabla_h^2 \chi$, respectively. Figure 2.2 illustrates the horizontal winds corresponding to rotational and divergent components of the atmospheric circulation in the lower stratosphere (24 km) simulated with the four models included in this thesis.

The spectrum of rotational kinetic energy (RKE) and divergent kinetic energy (RKE) per unit mass can be defined similarly to (2.4) as

$$E_R^{lm} = \frac{1}{2}(\mathbf{u}_R, \ \mathbf{u}_R)_{lm} = \frac{r^2}{2l(l+1)}|\zeta_{lm}|^2 \tag{2.6}$$

and

$$E_D^{lm} = \frac{1}{2}(\mathbf{u}_D, \ \mathbf{u}_D)_{lm} = \frac{r^2}{2l(l+1)}|\delta_{lm}|^2 \tag{2.7}$$

From (2.4), (2.6), and (2.7), it follows that $E_h = E_R + E_D$. This decomposition of the total kinetic energy is valuable for investigating the dynamics that underlie the kinetic energy spectrum since rotational modes are often used to approximate large-scale balanced dynamics. In contrast, the divergent modes and vertical motions are associated with fast unbalanced flows such as IGWs (Bierdel et al., 2016; Li and Lindborg, 2018).

In chapter 3, we analyze one-dimensional spectra of kinetic energy per unit mass obtained by summing over all zonal wavenumbers, i.e., the horizontal spectrum of kinetic energy per unit mass is defined as $E_h(l) = \sum_{|m|\leq l} E_h^{lm}$, and similarly for $E_R$, $E_D$, and $E_w$. In the literature, spectra are often shown as a function of horizontal wavenumber ($\kappa$) in Cartesian coordinates. From (2.4), one can define an equivalent horizontal wavenumber as $\kappa = \sqrt{[l(l+1)]}/r$, which roughly approximates $l/r$ at small scales. The horizontal wavelength is $\lambda_h = 2\pi/\kappa$.

## 2.3 NORMAL MODE DECOMPOSITION

Normal mode function (NMF) decomposition has been used extensively for representing a variety of geophysical phenomena on the globe. For studying the general circulation of the atmosphere, these modes are derived from the eigensolutions of the primitive equations linearized around a simple reference state of rest. This modal representation allows us to disentangle atmospheric motions into balanced low-frequency oscillations, such as large-scale Rossby waves, and high-frequency unbalanced motions, e.g., IGWs. Žagar et al. (2015) writes, *"...our view of the atmosphere is that of a vibrating system with many oscillation modes, like a musical instrument."* In contrast to spherical harmonic analysis, the main benefit of the NMF representation of the atmospheric circulation is that it can simultaneously represent both the wind and mass fields corresponding to the various modes, providing a more consistent representation of the underlying dynamics.

We perform a normal mode decomposition of global simulations using the MODES software, described in detail in Žagar et al. (2015). MODES performs a multivariate linear projection of the horizontal winds on balanced and unbalanced eigensolutions of the primitive equations, linearized around a resting background state (Kasahara and Puri, 1981). The orthogonal basis functions of the projection satisfy the dispersion relationships for Rossby waves (including the mixed Rossby–gravity wave mode) and inertia-gravity waves, including the Kelvin mode (Kasahara, 2020). In the following,
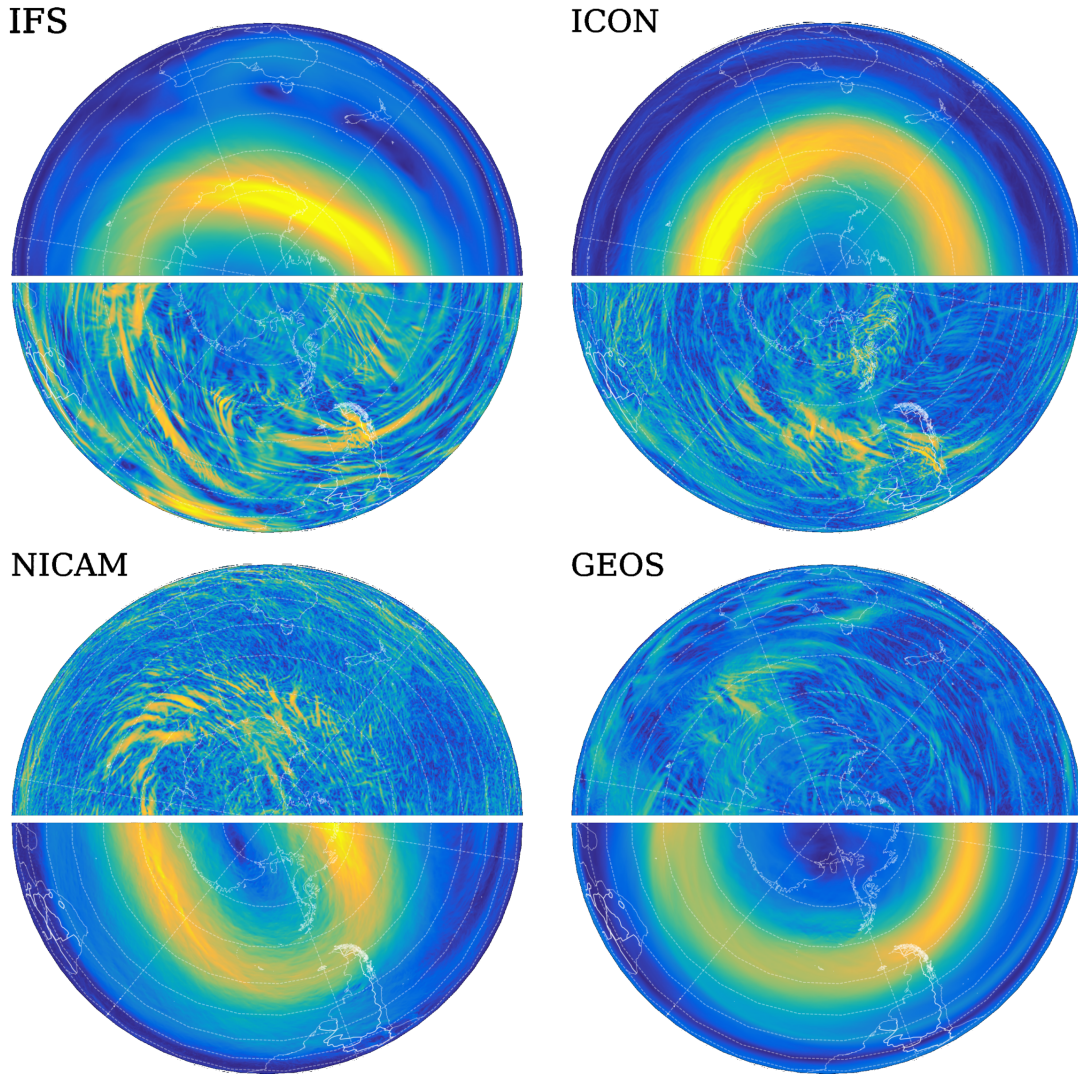
**Figure 2.2:** Snapshot of the Helmholtz decomposition of the atmospheric circulation performed on the horizontal wind for the IFS, ICON, NICAM, and GEOS models at 24 km corresponding to 0600 UTC February 3, 2020. The map is an orthographic projection centered on the south pole and 57°W. Blue represents slow horizontal wind speed, and yellow is fast horizontal wind speed. Wind speed associated with the rotational component is shown at the top and bottom parts of the figure, where large-scale structures such as the southern hemispheric polar vortex are visible. The divergent component, shown in the middle section, contains fine-scale structures mainly associated with gravity waves.

we will refer to the "balanced" component of the flow as that which projects onto the low-frequency linear Rossby modes, as opposed to the standard definition of a flow in which the three-dimensional velocity field is functionally related to the mass field (McIntyre, 2015). The "unbalanced" component of the flow is defined as that which projects onto the linear IGWs. Given the linearity of the decomposition, the IGW modes may contain some ageostrophic imbalance, not only freely propagating IGWs.

First, we interpolate the required input fields (three-dimensional horizontal winds, temperature, specific humidity, topography, and surface pressure) to a regular N256 Gaussian grid. The horizontal resolution at the Equator is $\sim$39 km. As the set of

NMFs implemented in MODES is defined on sigma levels (Kasahara and Puri, 1981), we next interpolate the three-dimensional fields vertically to 68 hybrid sigma/pressure levels extending from the surface to ~10 hPa (about 32 km). The NMF decomposition is carried out at individual timesteps and provides the spectrum of the horizontal kinetic plus available potential energy as a function of the zonal wavenumber and the meridional and vertical wave indices, which define the Hough harmonics. Since MODES is computationally expensive, we use a zonal wavenumber truncation of $l = 320$, which resolves horizontal wavelengths ($\lambda_h \sim 125$ km). Although MODES provides the energy spectra of kinetic and potential energies in the 3D-modal space as a function of longitudinal, meridional, and vertical scales, we isolate the wind field associated with the balanced and unbalanced circulation by projecting back to physical space, as demonstrated, for instance, in Žagar et al. (2017). The motivation behind this approach is to maintain consistency through the analysis and for a proper comparison to the full-resolution simulations in Chapter 3. Moreover, the spectral energy budget analysis in Chapter 4 requires velocity and mass fields in physical space.

Figure 2.3 illustrates the modal decomposition performed on ICON outputs in the lower stratosphere (24 km), corresponding to 0600 UTC on February 3, 2020. The inverse projection of horizontal wind associated with the Rossby and IGW modes is shown in Figs 1a and 1b. Large-scale features dominate the balanced circulation at this level, i.e., the stratospheric polar vortex, while the IGW circulation contains contributions from large scales at high latitudes and smaller scales in the tropics. The large-scale IGW energy seems to be associated with spontaneously generated waves around the polar vortex, at least in the stratosphere. In addition, the gradient wind balance may contribute to the IGW energy at planetary scales in the winter stratosphere (Žagar et al., 2015). In energetic terms, the large-scale portion of the horizontal kinetic energy spectrum ($E_h$) is mainly explained by the kinetic energy spectrum of the Rossby modes ($E_{RO_h}$), which is purely rotational ($E_{RO_h} \sim E_r$), at scales $L \gtrsim 600$ km (see Fig. 2.3c). At mesoscales ($L \lesssim 600$ km), the horizontal kinetic energy spectrum $E_{IG_h}$ of the IGW component and the purely vortical energy $E_r$ have comparable magnitudes. Section 3.3 examines the contributions of balanced and unbalanced components to the energy spectra in more detail. The following section describes the method for estimating the vertical velocity from horizontal IGW and Rossby modes shown in Fig. 2.3.

**Software availability.** Access to the MODES software can be requested at
https://modes.cen.uni-hamburg.de/software.

## 2.4 ESTIMATING VERTICAL VELOCITY

To diagnose the vertical velocity field from horizontal wind associated with IGW modes, we start with the mass continuity equation in hybrid-sigma vertical coordinates (Simmons and Burridge, 1981). The diagnostic equation for vertical pressure velocity $\omega$ is expressed as follows:

$$\omega(\eta) = -\int_0^\eta \nabla \cdot \left(\mathbf{u}\frac{\partial p}{\partial \eta}\right) d\eta \; + \; \mathbf{u} \cdot \nabla p, \tag{2.8}$$
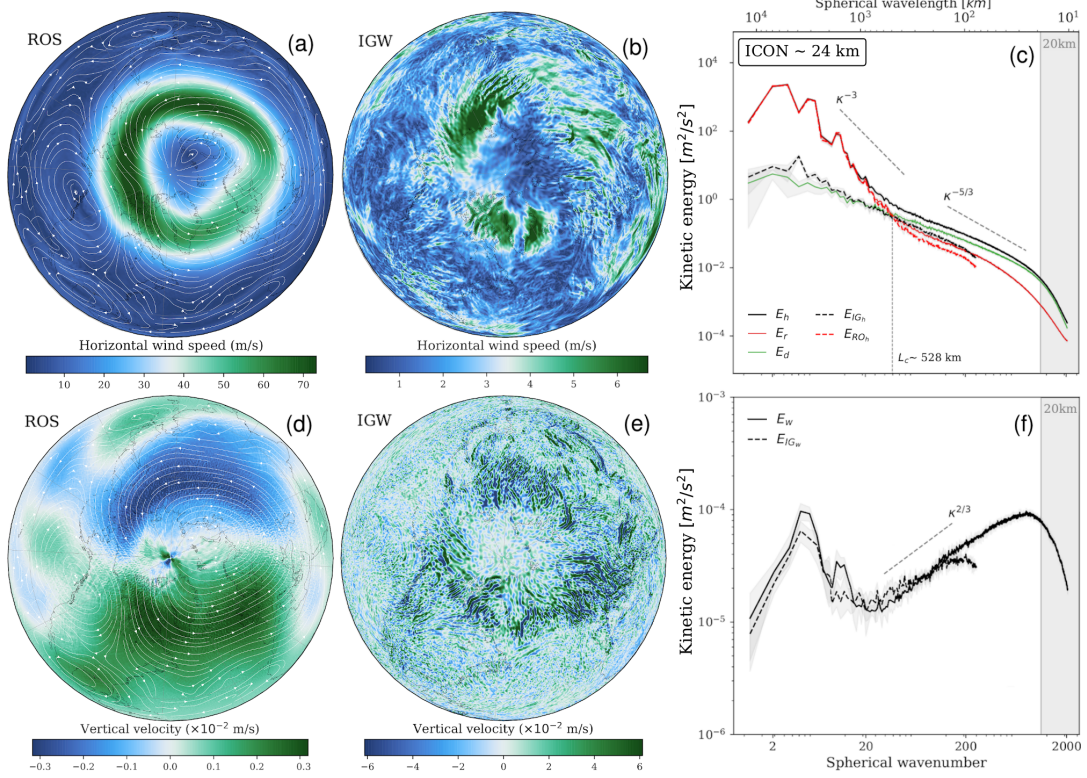
**Figure 2.3:** Modal decomposition of the atmospheric circulation performed on ICON at 24 km corresponding to 0600 UTC February 3, 2020. (a),(b),(d),(e) Maps in an orthographic projection centered at the North Pole and 57°W. The maps in (a) and (b) show the horizontal winds of Rossby and IGW modes from the inverse NMF decomposition. The vertical velocities of (d) Rossby and (e) IGW modes are calculated by solving mass continuity (2.8), discussed in detail in section 2.4. (c) The horizontal kinetic energy spectra associated with Rossby modes $E_{RO_h}$ (dashed red) and IGWs $E_{IG_h}$ (dashed black); the rotational $E_r$ and divergent $E_d$ kinetic energy spectra from the Helmholtz decomposition are shown in solid red and green, respectively. (f) The vertical kinetic energy spectra $E_w$ (solid black) and estimated IGW vertical kinetic energy spectra $E_{IG_w}$ (dashed black). The spectra shown in (c) and (f) are averaged over 24 hours on February 3, 2020, and the shaded area around each line indicates the standard deviation. Reference slopes for $\kappa^{-3}$, $\kappa^{-5/3}$, and $\kappa^{2/3}$ are shown in dashed lines. The gray shaded area indicates horizontal wavelengths $< 20$ km.

where $\mathbf{u} = (u, v)$ is the horizontal wind vector, and $p$ is pressure. The vertical coordinate $\eta(p, p_s)$ is a monotonic function of pressure and depends on the surface pressure $p_s$ such that $\eta(p_s, p_s) = 1$ and $\eta(0, p_s) = 0$. A detailed description of the vertical coordinate system is given in Untch and Hortal (2003). We solve (2.8) numerically using the IFS vertical discretization (ECMWF, 2021) since the vertical grid used for the modal decomposition is a sub-sample of the IFS vertical grid L137. The discrete analogue of Eq.2.8 defined at model half-levels reads

$$\omega_{k+\frac{1}{2}} = -b_{k+\frac{1}{2}} \frac{\partial p_s}{\partial t} - \sum_{j=1}^{k} \delta_j \Delta p_j + \Delta b_j (\mathbf{u}_j \cdot \nabla p_s), \tag{2.9}$$

where $\Delta b_k = b_{k+1/2} - b_{k-1/2}$, and $\Delta p = \Delta a_k + \Delta b_k p_s$. The terms $\delta_j$ and $\nabla_h p_s$ are the horizontal wind divergence and horizontal gradient of surface pressure. We set a

boundary condition $\omega_{N+1/2} = 0$ Pa/s at the surface and calculate the average between consecutive levels to obtain vertical velocity at full model levels. The rate of change of surface pressure is

$$\frac{\partial p_s}{\partial t} = -\sum_{j=1}^{N} \delta_j \Delta p_j + \Delta B_j (\mathbf{u}_j \cdot \nabla p_s), \tag{2.10}$$

where $N$ is the number of vertical levels. Finally, assuming hydrostatic balance, the vertical velocity $w$ is estimated using $w = -\omega/(\rho g)$, where $\rho$ is the air density and $g$ is the acceleration of gravity.

## 2.5 FORMULATION OF THE SPECTRAL ENERGY BUDGET

This section briefly describes the formulation of the spectral energy budget presented in Augier and Lindborg (2013). The budget is derived from the primitive system of equations for the conservation of momentum and energy in pressure ($p$) coordinates for a dry atmosphere

$$\partial_t \mathbf{u} = -\mathbf{u} \cdot \nabla_h \mathbf{u} - \omega \partial_p \mathbf{u} - \nabla_h \Phi - \mathbf{f}(\varphi) \times \mathbf{u} + \mathbf{D_u} \tag{2.11}$$

$$\partial_t \theta' = -\mathbf{v} \cdot \nabla \theta' - \omega \partial_p \langle \theta_r \rangle - \partial_t \langle \theta_r \rangle + Q_\theta + D_\theta \tag{2.12}$$

where $\mathbf{v} = (\mathbf{u}, \omega)$ is the three-dimensional velocity vector, with $\mathbf{u}$ being the horizontal wind, and $\omega = D_t p$ is the Lagrangian tendency of pressure also known as vertical pressure velocity. The first and second terms on the r.h.s are the horizontal and vertical components of the advection of the horizontal wind, respectively, where the horizontal part can be expressed in vector invariant form as $\mathbf{u} \cdot \nabla_h \mathbf{u} = \nabla_h K_h + \zeta \mathbf{e}_z \times \mathbf{u}$, where $K_h$ is the horizontal kinetic energy, and $\mathbf{e}_z$ the upward (radial) unit vector. The third term denotes the horizontal pressure gradient, where $\Phi$ is the geopotential, which can be diagnosed from the hydrostatic equation $\partial_p \Phi = -R_d T/p$, where $T$ is the air temperature and $R_d$ the gas constant of dry air. Next, the Coriolis acceleration is expressed in terms of $\mathbf{f}(\varphi) = f(\varphi)\mathbf{e}_z$ where the Coriolis parameter $f(\varphi) = 2\Omega sin(\varphi)$, is a function of latitude ($\varphi$) and the frequency of the Earth rotation $\Omega$. Equation (2.12) is expressed in terms of the perturbation of potential temperature, defined as $\theta' = \theta - \langle \theta_r \rangle$, where $\langle \theta_r \rangle$ is the "representative mean" i.e., the global average over a constant pressure level for values above the surface.

To formulate the spectral energy budget, we recall the definition of the HKE spectrum given in (2.4), and the horizontal spectrum of available potential energy (APE) is defined as

$$E_A^{lm} = \gamma(p)\frac{(\theta', \theta')_{lm}}{2} = \gamma(p)\frac{|\theta'_{lm}|^2}{2}, \tag{2.13}$$

where $\gamma(p) = -R_d \pi(p)/[p\partial_p \langle \theta_r \rangle]$ is the Lorenz's stability parameter, where $\pi(p) = (p/p_o)^{(R_d/C_p)}$ is the scaled pressure also known as the Exner function, with $p_o = 1$ bar.

The evolution equations for APE and HKE can be obtained by substituting (2.12) and (2.11) into the time derivative of (2.13) and (2.4) respectively–that is, $\partial_t E_A^{lm} = \gamma(p)(\theta', \partial_t \theta')_{lm}$ and $\partial_t E_h^{lm} = (\mathbf{u}, \partial_t \mathbf{u})_{lm}$. Reorganizing the resulting terms yields

$$\partial_t E_A^{lm} = G_A^{lm} - C_{A \to K}^{lm} + \partial_p F_{A\uparrow}^{lm} + T_A^{lm} + D_A^{lm} \tag{2.14}$$

and

$$\partial_t E_h^{lm} = C_{A \to K}^{lm} + \partial_p F_{K\uparrow}^{lm} + T_K^{lm} + L^{lm} + D_K^{lm}, \tag{2.15}$$

where the term $G_A = \gamma(p)(\theta', Q_\theta)_{lm}$ is the generation of APE due to diabatic heating, i.e., (parametrized) radiation and latent heat release or sources/sinks from the surface, $C_{A \to K} = -(\omega, \alpha)_{lm}$ is the conversion from APE to HKE, where $\alpha = R_d T/p$ is the specific volume. The terms $D_A^{lm} = \gamma(p)(\theta', D_\theta)_{lm}$ and $D_K^{lm} = (\mathbf{u}, D_{\mathbf{u}})_{lm}$ are the dissipation from parametrized processes and numerical diffusion for APE and HKE respectively. In 2.15, $L^{lm} = -(\mathbf{u}, f(\varphi)\mathbf{e}_z \times \mathbf{u})_{lm}$ is a linear spectral transfer term arising from the Coriolis effect. The vertical energy flux, denoted as $F_{K\uparrow}$, combines the pressure flux and the resolved turbulent vertical transfer. In contrast to the previous formulations, AL13's formulation exactly separates the pressure gradient term into conversion and vertical flux using the continuity and hydrostatic equations, i.e.,

$$-(\mathbf{u}, \nabla_h \Phi)_{lm} = C_{A \to K}^{lm} - \partial_p(\omega, \ \Phi)_{lm} \tag{2.16}$$

where the second term in r.h.s is the pressure flux associated with vertically propagating IGWs. Considering the exact three-dimensional advection, the total vertical flux reads

$$F_{K\uparrow} = -(\omega, \ \Phi)_{lm} - (\mathbf{u}, \ \omega \mathbf{u})_{lm} \tag{2.17}$$

where the second term is the resolved turbulent vertical transfer. The vertical APE flux is simply $F_{A\uparrow} = -\gamma(p)(\theta', \ \omega \theta')_{lm}/2$. The terms $T_{A,K}$ are the nonlinear spectral transfers computed as the complementary part of the nonlinear advection terms

$$T_A^{lm} = -\gamma(p)(\theta', \ \mathbf{v} \cdot \nabla \theta')_{lm} + \gamma(p)\partial_p(\theta', \ \omega \theta')_{lm}/2 \tag{2.18}$$

and

$$T_K^{lm} = -(\mathbf{u}, \mathbf{v} \cdot \nabla \mathbf{u})_{lm} + \partial_p(\mathbf{u}, \ \omega \mathbf{u})_{lm}/2 \tag{2.19}$$

where $\mathbf{v} = (\mathbf{u}, \ \omega)$ is the three-dimensional wind. These nonlinear transfers are conservative and only redistribute energy across horizontal scales at a pressure level.

### 2.5.1 Helmholtz decomposition of the spectral energy budget

The spectral budget of horizontal kinetic energy can be further decomposed into its divergent and rotational components as demonstrated by Li et al. (2023). The budget equations for each kinetic energy component read:

$$\partial_t E_D^{lm} = C_{A\to D}^{lm} - C_{D\to R}^{lm} + \partial_p F_{D\uparrow}^{lm} + T_D^{lm} + D_D^{lm} \tag{2.20}$$

$$\partial_t E_R^{lm} = C_{D\to R}^{lm} + T_R^{lm} + D_R^{lm} \tag{2.21}$$

where $C_{A\to D} = C_{A\to K}$, since energy conversion from available potential energy only affects the divergent component. Similarly, the vertical flux of kinetic energy is only allowed for the divergent component, i.e., $F_{D\uparrow}^{lm} = F_{K\uparrow}^{lm}$. For more details on the derivation of each term, see Li et al. (2023). The term $C_{D\to R}$ represents the spectral conversion term from DKE to RKE, which can be expressed as

$$C_{D\to R}^{lm} = [(\mathbf{u}_D, \boldsymbol{\eta} \times \mathbf{u})_{lm} - (\mathbf{u}_R, \boldsymbol{\eta} \times \mathbf{u})_{lm} - (\partial_p \mathbf{u}, \omega \mathbf{u}_R)_{lm} - (\mathbf{u}_R, \omega \partial_p \mathbf{u})_{lm}]/2 \tag{2.22}$$

where $\boldsymbol{\eta}$ is the absolute vorticity vector defined as $\boldsymbol{\eta} = (\zeta + f)\mathbf{e}_z$. The first two terms of the spectral conversion can be further divided into the contributions from relative vorticity and the Coriolis effect, while the last terms correspond to the contributions from vertical motion. From (2.21), neglecting dissipative processes, it is evident that RKE can increase only by conversion from DKE. The exact formulas for the RKE and DKE spectral energy transfers are

$$T_R^{lm} = [(\partial_p \mathbf{u}, \omega \mathbf{u}_R)_{lm} - (\mathbf{u}_R, \omega \partial_p \mathbf{u})_{lm} - (\mathbf{u}_R, \boldsymbol{\eta} \times \mathbf{u})_{lm} - (\mathbf{u}, \boldsymbol{\eta} \times \mathbf{u}_R)_{lm}]/2 \tag{2.23}$$

and

$$\begin{aligned} T_D^{lm} = &-[(\mathbf{u}_D, \nabla_h E_K)_{lm} + (\mathbf{u}, \delta\mathbf{u})_{lm}/2] \\ &- [(\mathbf{u}_D, \omega\partial_p \mathbf{u})_{lm} - (\partial_p \mathbf{u}, \omega\mathbf{u}_D)_{lm}]/2 \\ &- [(\mathbf{u}_D, \boldsymbol{\eta} \times \mathbf{u})_{lm} - (\mathbf{u}, \boldsymbol{\eta} \times \mathbf{u}_D)_{lm}]/2. \end{aligned} \tag{2.24}$$

Note that the total spectral transfer of HKE satisfies $T_R^{lm} + T_D^{lm} = T_K^{lm} + L^{lm}$, where the linear Coriolis term contributes to the spectral transfers of DKE and RKE; however, this term does not involve interactions between the rotational and divergent parts of the flow.

### 2.5.2 Flux form of the spectral energy budget

In order to investigate the energy transfer processes, it is convenient to construct the corresponding spectral energy fluxes. First, the total wavenumber spectrum for each term in the energy budget equations can be obtained by summing over all corresponding zonal wavenumbers. Additionally, the spectrum is vertically integrated within a layer between two pressure levels considering the vertical variation of density,

so the resulting spectral quantities have units of energy rather than energy per unit mass. For example, the total integrated wavenumber spectrum of HKE is defined as

$$E_K[l]_{p_t}^{p_b} = \int_{p_t}^{p_b} \frac{dp}{g} \sum_{|m| \leq l} E_K^{lm}(p) \tag{2.25}$$

where $p_b$ and $p_t$ are the atmospheric pressure at the bottom and top of the layer, respectively. The vertically integrated energy fluxes are defined as in (2.25) and then summed over all the spherical harmonics with total wavenumber greater than or equal to $l$ (i.e., the cumulative sum starting from the largest wavenumber).

The flux form of the spectral budget of available potential energy (APE), as well as rotational (RKE) and divergent (DKE) kinetic energies as a function of total wavenumber and integrated into a layer between the bottom ($p_b$) and the top ($p_t$) pressure levels as in (2.25), read:

$$\partial_t \mathcal{E}_A |_{p_t}^{p_b} = \mathcal{G}_A |_{p_t}^{p_b} - \mathcal{C}_{A \to D} |_{p_t}^{p_b} + \Delta_{p_t}^{p_b} \mathcal{F}_{A\uparrow} + \Pi_A |_{p_t}^{p_b} + \mathcal{D}_A |_{p_t}^{p_b}, \tag{2.26}$$

$$\partial_t \mathcal{E}_D |_{p_t}^{p_b} = \mathcal{C}_{A \to D} |_{p_t}^{p_b} - \mathcal{C}_{D \to R} |_{p_t}^{p_b} + \Delta_{p_t}^{p_b} \mathcal{F}_{D\uparrow} + \Pi_D |_{p_t}^{p_b} + \mathcal{D}_D |_{p_t}^{p_b}, \tag{2.27}$$

$$\partial_t \mathcal{E}_R |_{p_t}^{p_b} = \mathcal{C}_{D \to R} |_{p_t}^{p_b} + \Pi_R |_{p_t}^{p_b} + \mathcal{D}_R |_{p_t}^{p_b} \tag{2.28}$$

where the terms denoted by $\mathcal{F}_\uparrow$ are the cumulative (inward) vertical fluxes. The vertical DKE flux is defined as $\Delta_{p_t}^{p_b} \mathcal{F}_{D\uparrow} = g^{-1}[\mathcal{F}_{D\uparrow}(p_b) - \mathcal{F}_{D\uparrow}(p_t)]$, and similarly for the vertical flux of APE. These vertical fluxes are almost exclusively associated with vertically propagating gravity waves. The terms $\Pi_{A,D,R}$ are the cumulative nonlinear transfers redistributing energy across horizontal scales. For example, the nonlinear spectral flux of kinetic energy can be defined from (2.19) as

$$\Pi_N(l)_{p_t}^{p_b} = \sum_{n \geq l} \int_{p_t}^{p_b} \frac{dp}{g} \sum_{|m| \leq n} T_K^{nm}(p). \tag{2.29}$$

The total kinetic energy transfer is $\Pi_K(l) = \Pi_N(l) + \Pi_L(l)$, where $\Pi_L(l)$ is obtained from applying 2.29 to the linear Coriolis transfer $L^{lm}$. The total kinetic energy transfer can also serve as a budget check for simulations of GCMs since, by definition, $\Pi_K(l = 0) = 0$, which rests on the fact that the global mean of conservative energy fluxes at a pressure surface should vanish. After vertically integrating equations (2.14) and (2.15) for the entire mass of the atmosphere, using the summing convention as in (2.29) and putting $l = 0$, it is possible to recover the original energy budget equations formulated by Lorenz (1955). The terms $\mathcal{D}_{A,D,R}$ are cumulative dissipation from parametrizations and different numerical filters. Assuming the stationarity of the HKE and APE spectra and neglecting the divergence of the vertical fluxes at the boundaries (which should be exactly zero if vertically integrated for the full depth of the atmosphere), a quantitative estimation of the dissipation of HKE ($D_K$) and the effective net forcing $\Delta(\mathcal{G}_A - \mathcal{D})$ for a given wavenumber range $[l_1, l_2]$ is obtained

from the difference of the cumulative fluxes (2.26), (2.28) and (2.27) at these two wavenumbers. Following Augier and Lindborg (2013), the expressions for the HKE dissipation and the total effective forcing read

$$\Delta \mathcal{D}_K = \Delta \mathcal{C}_{A \to D} + \Delta \Pi_K \tag{2.30}$$

and

$$\Delta (\mathcal{G}_A - \mathcal{D}) = -\Delta \Pi, \tag{2.31}$$

where $\mathcal{D} = \mathcal{D}_K + \mathcal{D}_A$ is the total energy dissipation, $\Pi = \Pi_K + \Pi_A$ is the total energy spectral transfer, and $\Delta \Pi_K = \Pi_K(l_1) - \Pi_K(l_2)$, and similarly for the other fluxes [note the nonstandard definition of $\Delta$]. Note that expressions (2.30) and (2.31) are approximations based on the assumption of stationarity of the kinetic and available potential energy spectra. For applications to assess the degree of imbalance in GCMs, it is required to calculate the generation and dissipation terms explicitly from the corresponding dynamic tendencies, as well as tendencies from physics and parametrized processes.
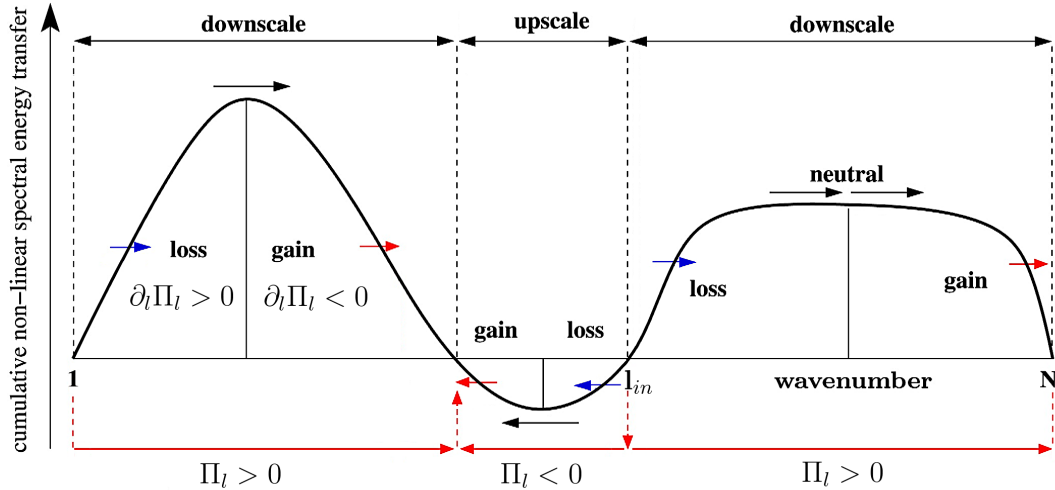


**Figure 2.4:** Schematic graph of cumulative nonlinear spectral energy flux $\Pi_K$. Downscale transfer is given for $\Pi_K > 0$ and upscale transfer for $\Pi_K < 0$. Modified from Malardel and Wedi (2016).

Finally, to facilitate the interpretation of the nonlinear spectral fluxes, we illustrate a hypothetical $\Pi_K$ curve in Fig. 2.4. The slope of a $\Pi(l)$ curve determines whether energy is gained or lost at a particular wavenumber. If the slope is negative at wavenumber $l$, energy is deposited at this wavenumber (but it does not say if the cascade is upscale or downscale); if the slope is positive, nonlinear interactions remove energy from wave number $l$. As both $\Pi(0) = 0$ and $\Pi(l > N) = 0$, if $\Pi(l) > 0$, the range of wavelengths from $l$ to $N$ receives energy from the range of wavelengths 0 to $l$ (but it does not say at which wavelength exactly it will be deposited). The energy cascade is then downscale (net energy transfer toward wave numbers larger than $l$) for $\Pi(l) > 0$ and upscale for $\Pi(l) < 0$. A plateau of the $\Pi(l)$ curve ($\partial_l \Pi(l) = 0$) corresponds to an energy transfer through the scales (downscale if the value of the plateau is $> 0$, upscale if it is negative) without deposition or loss of energy at $l$

due to nonlinear interaction (constant energy flux). Let us define a wavenumber $l_{in}$ where the conditions $\partial_l \Pi(l_{in}) > 0$ and $\Pi(l_{in}) = 0$ meet simultaneously. At this wavenumber, energy is deposited and subsequently diverges through an upscale cascade for wavenumbers $l < l_{in}$ and downscale for wavenumbers $l > l_{in}$. The scale corresponding to $l_{in}$ is known as the energy injection scale.

# 3 | THE DYNAMICS OF THE VERTICAL VELOCITY SPECTRUM

*Big waves have little waves,*
*that feed on deformation;*
*and little waves have lesser waves,*
*to turbulent dissipation.*

— Dewan, E. M. (1979)

## 3.1 INTRODUCTION

Understanding the dynamic coupling between horizontal and vertical atmospheric motions is essential to unraveling the mechanisms that shape mesoscale kinetic energy spectra. However, a critical piece of the puzzle is missing: what mechanisms control vertical kinetic energy at mesoscales? There is strong observational and numerical evidence of vertical kinetic energy spectra ($E_w$) relatively flat at mesoscales with a local maximum at small scales, leaving the explanation of this maximum open. Global storm-resolving simulations have shown that $E_w$ peaks at synoptic scales (Terasaki et al., 2009; Skamarock et al., 2014), which can be associated with long atmospheric waves; however, validating this feature with observations is unattainable. Global storm-resolving simulations with state-of-the-art general circulation models (GCMs) provide an opportunity to test proposed theories, as they compare well with observations (Hamilton et al., 2008; Terasaki et al., 2009; Skamarock et al., 2014; Selz et al., 2019). The newest generation of these models is now running at kilometer scales, explicitly resolves deep convection, and can therefore be expected to represent mesoscale dynamics realistically. The availability of three-dimensional data has proven valuable for the interpretation of one-dimensional aircraft observations across a wide range of scales (Bierdel et al., 2016). However, observational validation of simulated vertical velocities remains a challenge, as observations of vertical velocities across different horizontal scales, particularly on mesoscales, are scarce (Bacmeister et al., 1996; Bony and Stevens, 2019; Stephan and Mariaccia, 2021b). For this reason, vertical velocity spectra have been studied much less compared to horizontal energy spectra (Bacmeister et al., 1996; Callies et al., 2016; Schumann, 2019).

This chapter examines whether different kilometer-scale global GCMs agree on the relationship between vertical and horizontal kinetic energy spectra and how existing theoretical models explain the relationship. For this purpose, we employ storm-resolving global simulations from the DYAMOND (the DYnamics of the Atmospheric general circulation Modeled On Non-hydrostatic Domains) experiment (Stevens et al.,

2019), which explicitly model deep convection. There are several aspects related to model design and configuration that are known to affect the kinetic energy spectrum (Skamarock et al., 2014). These include the convective parameterizations, microphysics, vertical resolution, numerical filters, the representation of subgrid processes that account for unresolved turbulent motions, and subgrid-scale orography. Horizontal motion spectra and their dependence on model formulation are discussed in detail in Stephan et al. (2022), including the simulations analyzed here. The representation of explicit vs. parameterized convection and their effects on convectively generated IGWs and the vertical velocity spectrum for several configurations of the Integrated Forecasting System (IFS) model are discussed in Polichtchouk et al. (2022). Foremost, we focus on the relationship between the models' horizontal and vertical kinetic energy spectra rather than comparing the components in isolation. This relationship between spectra can shed light on the underlying physical processes, as revealed in the analysis. In particular, we are interested in whether or not the properties of resolved IGWs matter for how the vertical velocity spectrum relates to the horizontal motion spectrum.

This chapter is structured as follows: Section 3.2 compares the horizontal and vertical kinetic energy spectra between models and examines their vertical dependence. Furthermore, section 3.3 examines the contribution of balanced and unbalanced circulations to the total horizontal kinetic energy using two approaches: a Helmholtz decomposition, which yields the horizontal wind's purely divergent and rotational components, and a normal mode function decomposition, which yields the contribution of IGWs to the horizontal kinetic energy spectra. The vertical velocity spectrum of IGWs is estimated by numerically solving the mass continuity equation in physical space and then computing its spherical harmonic expansion. Furthermore, section 3.4 explores the possibility that the shape of the vertical kinetic energy spectrum can be inferred from knowledge of the horizontal kinetic energy spectrum at the same level but without invoking information about other levels. Finally, section 3.5 summarizes the results and conclusions.

## 3.2 THE ENERGY SPECTRUM IN GLOBAL STORM-RESOLVING MODELS

We begin this section with comparisons of the horizontal kinetic energy spectra ($E_h$) and the vertical kinetic energy spectra ($E_w$) between the different simulations before investigating how they relate to each other in subsection 3.4. The spectra differ substantially between the troposphere and the stratosphere, so we mainly show 6 km as representative of the free troposphere and 24 km as representative of the stratosphere.

Figure 3.1 shows $E_h$ as a function of the spherical wavenumber for ICON, IFS, GEOS and NICAM. The models reproduce the observed shape of the Nastrom-Gage spectrum to first order. The models agree well in spectral power across all scales at 6 km and scales of 1000–2000 km at 24 km. Overall, the greatest differences exist in the mesoscale region in the stratosphere. ICON shows similar mesoscale energy per unit mass in the troposphere and the stratosphere; these results are in agreement

with the results of Skamarock et al. (2014) (hereafter S14), based on global MPAS simulations with a horizontal resolution of 3 km. The GEOS and IFS models have slightly less energy in the stratosphere, whereas NICAM has greater mesoscale energy than in the troposphere. The scale at which dissipative effects become visible varies considerably between the models ($\sim$20–50 km wavelength). As noted by Skamarock (2004), the effective resolution can be affected by numerical damping and various filters. Spectral power decays already at scales < 100 km in the IFS. The related absence of the observed spectral slope -5/3 at mesoscales in the IFS model has been pointed out in previous studies and linked to the effects of parameterized energy transfer of subgrid-scale processes (Shutts, 2005; Malardel and Wedi, 2016).
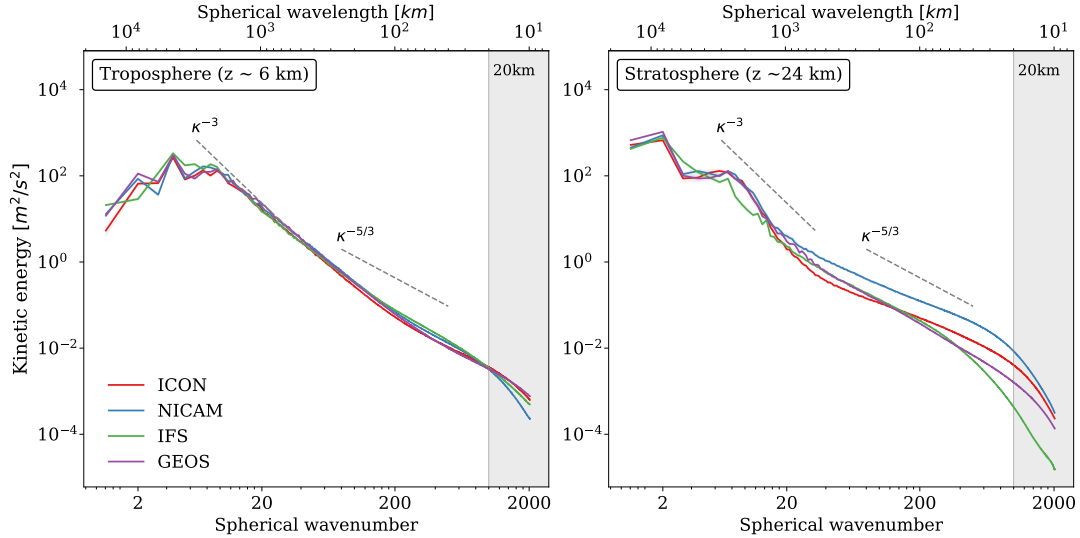


**Figure 3.1:** Horizontal kinetic energy spectra as a function of spherical wavenumber for ICON, NICAM, IFS and GEOS (left) in the free troposphere at 6 km and (right) in the stratosphere at 24 km. Reference slopes of $\kappa^{-3}$ and $\kappa^{-5/3}$ are shown in dashed lines. The gray shaded area indicates horizontal wavelengths < 20 km.

Table 3.1 lists the spectral slopes obtained by performing a piecewise linear regression of each spectrum in logarithmic space for the intervals 20 km $\leqslant \lambda_h < L$ and $L \leqslant \lambda_h \leqslant 2000$ km, where $\lambda_h$ is the horizontal wavelength. The synoptic-to-mesoscale transition scale ($L$) is the intermediate point in 20–2000 km that minimizes the sum of the squared errors of both intervals. Tropospheric spectral slopes vary slightly from model to model and are consistently shallower than -3 in the wavelength range 200–2000 km, ranging from $-2.49$ to $-2.58$. Stratospheric slopes are steeper than -3 for ICON (-4.12), slightly steeper for GEOS (-3.52), and NICAM (-3.59), while the IFS slopes remain close to -3. The mesoscale slopes are consistently steeper than $-5/3$ in the troposphere ranging from $-2.16$ to $-1.9$. In the stratosphere, the slopes of IFS and GEOS remain close to $-1.7$ and shallower in ICON (-1.24) and NICAM (-1.31).

Figure 3.2 illustrates how $E_h$ varies with height. The transition scale varies between 112–194 km in the troposphere and between 663–948 km in the stratosphere, agreeing with S14 results. The increase with altitude of the transition scale is not gradual but occurs abruptly at the tropopause somewhere between 12–16 km. The vertical variation of $E_h$ in the IFS compares favorably to the results of Burgess et al. (2013) based on T799 ECMWF operational analysis.

**Table 3.1:** Regression of spectral slopes for ICON, IFS, GEOS, and NICAM at 6 and 24 km. The vertical grid spacing $\Delta z$ is given for each model. The transition scale from synoptic to mesoscale is denoted as $L$. Estimated slopes and standard errors (std. err.) are shown for wavelength intervals of $20\ \text{km} \leqslant \lambda_h < L$ and $L \leqslant \lambda_h \leqslant 2000$ km.

| z ∼ 6 km | $\Delta z(m)$ | $L$ (km) | $2000\ \text{km} \geq \lambda_h \geq L$ slope | std. err. | $L > \lambda_h \geq 20\ \text{km}$ slope | std. err. |
|---|---|---|---|---|---|---|
| ICON | 400.0 | 122 | -2.58 | 0.012 | -1.92 | 0.003 |
| IFS | 291.0 | 194 | -2.53 | 0.004 | -1.91 | 0.008 |
| GEOS | 251.5 | 132 | -2.57 | 0.005 | -2.16 | 0.004 |
| NICAM | 400.0 | 112 | -2.49 | 0.003 | -1.94 | 0.003 |
| z ∼ 24 km | | | | | | |
| ICON | 1008.0 | 663 | -4.12 | 0.011 | -1.24 | 0.036 |
| IFS | 521.5 | 948 | -3.09 | 0.021 | -1.74 | 0.097 |
| GEOS | 360.5 | 740 | -3.52 | 0.012 | -1.79 | 0.042 |
| NICAM | 986.0 | 794 | -3.59 | 0.012 | -1.31 | 0.046 |

The vertical velocity spectra show evidence of two different power-law behaviors and have approximately five orders of magnitude less energy integrated across resolved scales than their horizontal counterpart (note that Fig. 3.3 contains fewer orders of magnitude on the ordinate than Fig. 3.1). The results shown in Fig. 3.3 are in good agreement with previous findings regarding the spectral slopes of $E_w$ at mesoscales ($\lesssim 100$ km) from observations (Bacmeister et al., 1996; Gao and Meriwether, 1998) and from high-resolution numerical simulations (Terasaki et al., 2009; Skamarock et al., 2014; Craig and Selz, 2018b; Müller et al., 2018). All models predict a similar spectral power for the maximum found at large scales in the troposphere. As in the case of $E_h$, most of the differences between the models occur in the mesoscale range.

Figure 3.4 shows $E_w$ at various altitudes. The tropospheric and stratospheric spectra differ on several points. First, we observe a transition from slopes near $-1$ at large scales ($10 < l < 40$) toward slopes of about $1/3$ at the mesoscale in the troposphere. In contrast, the large-scale slopes are steeper than $-1$ for all models in the stratosphere. Regarding the mesoscale region in the stratosphere, ICON presents slopes steeper than $1/3$ of around $2/3$, while GEOS's slopes flatten after spherical wavenumber $l \sim 200$ and NICAM closely follows a $1/3$ scaling at all vertical levels. Finally, the $E_w$ slopes in IFS show signs of energy dissipation similar to those of $E_h$, namely flattening of the slopes and a rapid energy decay with wavenumber in the stratosphere at scales $l > 200$.

The evident diversity between models regarding the $E_h$ and $E_w$ scaling raises the question of whether the models' disagreement comes from differences in the underlying dynamics or model formulation. While beyond the scope of this paper, we recognize that aspects of a model's formulation that can influence the shape of the mesoscale kinetic energy spectrum include vertical resolution and vertical turbulent diffusion (Waite, 2016; Skamarock et al., 2019), which vary substantially in our simulations. Additionally, convective parameterizations also affect the kinetic energy spectrum
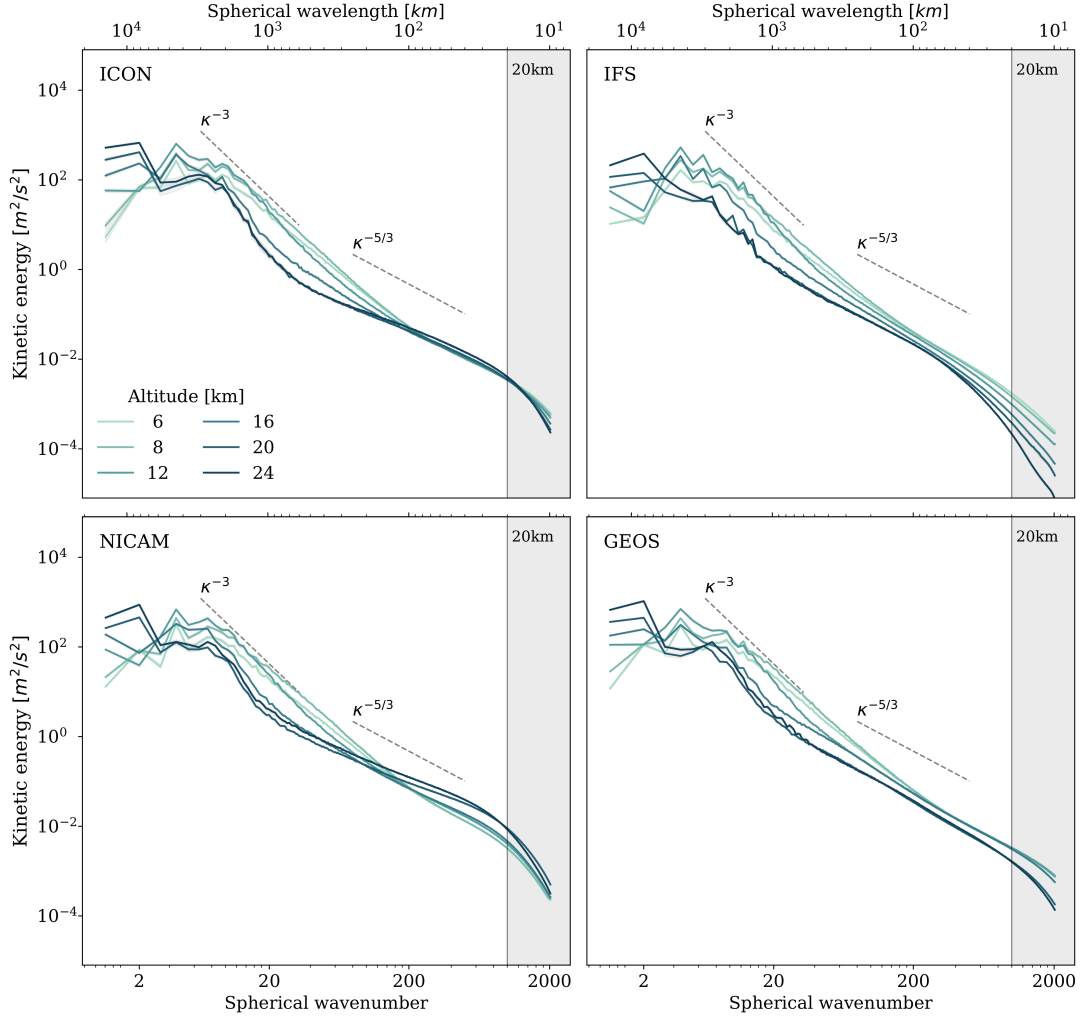
**Figure 3.2:** Horizontal kinetic energy spectra as a function of spherical wavenumber for ICON, IFS, NICAM and GEOS at heights of 6, 8, 12, 16, 20 and 24 km. Reference slopes of $\kappa^{-3}$ and $\kappa^{-5/3}$ are shown in gray dashed lines. The gray shaded area indicates horizontal wavelengths $< 20$ km.

at small scales since convection is a crucial IGW source (Polichtchouk et al., 2022; Stephan et al., 2022).

The vertical grid spacings $\Delta z$ for each model at levels 6 and 24 km are listed in Table 3.1. In the lower stratosphere, $\Delta z$ is coarser for ICON ($\sim 1$ km) and NICAM ($\sim 980$ m) compared to IFS ($\sim 520$ m) and GEOS ($\sim 360$ m). Insufficient vertical resolution might explain some differences between models, even at well-resolved horizontal scales. For example, ICON and NICAM exhibit shallower mesoscale spectral slopes compared to IFS and GEOS in the stratosphere (see Fig. 1), which might indicate that the spectra are not fully converged at this level, consistent with the results of Skamarock et al. (2019), where convergence is approached for $\Delta z \leq 200$ m in MPAS simulations. Waite (2016) indicated that the sensitivity of model spectra to vertical resolution depends on the vertical mixing scheme; with no vertical mixing or weak, stability-dependent mixing, the mesoscale spectra are artificially amplified by low resolution. Our simulations may show signs of amplification at the coarser vertical resolutions since ICON and NICAM, which have similar prognostic turbulent kinetic energy
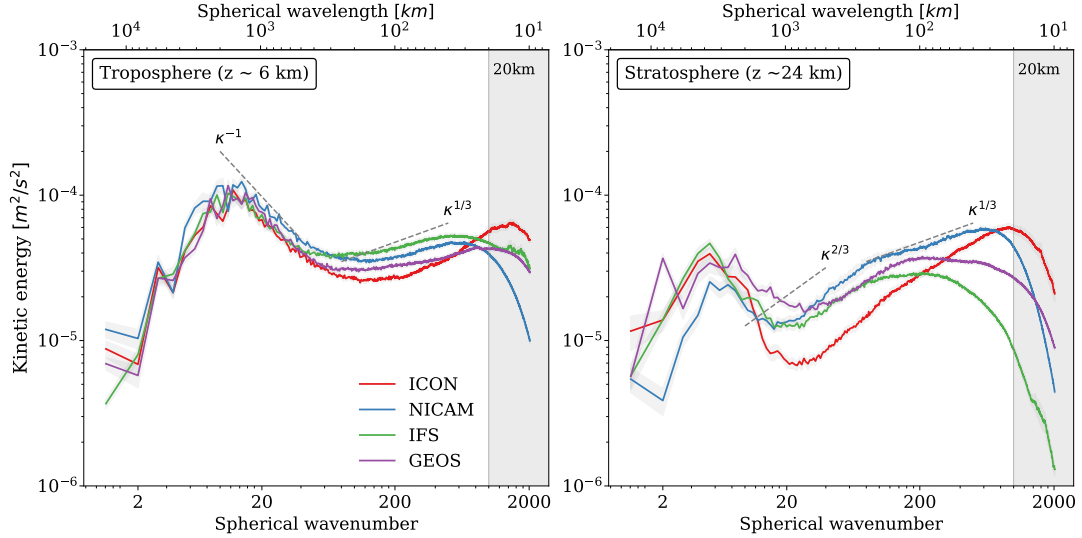
**Figure 3.3:** Vertical kinetic energy spectra as a function of spherical wavenumber for ICON, NICAM, IFS and GEOS (left) in the free troposphere at 6 km and (right) in the stratosphere at 24 km. Reference slope of $\kappa^{-1}$, $\kappa^{1/3}$ and $\kappa^{2/3}$ are shown in dashed lines. The gray shaded area indicates horizontal wavelengths $< 20$ km.

(TKE) schemes, show higher mesoscale energy magnitudes in the stratosphere than IFS and GEOS with a diagnostic eddy diffusivity scheme.

The shape of the mesoscale energy spectrum is often interpreted in terms of the different dynamics of balanced circulations and IGWs. Therefore, we next explore balanced and unbalanced dynamics contributions to $E_h$ and $E_w$.

## 3.3 GRAVITY WAVE CONTRIBUTIONS TO THE KINETIC ENERGY SPECTRUM

This section examines the contributions to $E_h$ from rotational ($E_r$) and divergent ($E_d$) energy spectra obtained by Helmholtz decomposition, as well as the spectra of IGW wind fluctuations ($E_{IG_h}$). In addition, $E_{IG_h}$ is further decomposed into its divergent ($E_{IG_d}$) and rotational ($E_{IG_r}$) components. Finally, we present the energy spectra of vertical velocity ($E_{IG_w}$) estimated from IGW horizontal winds.

In the following, we analyze the modal decomposition of DYAMOND simulations using MODES presented in Stephan et al. (2022). Since IGW fields are unavailable for NICAM, we only show energy spectra of IGW modes corresponding to the ICON, GEOS, and IFS models. Figure 3.5 shows all horizontal energy components for ICON, IFS and GEOS at 6 km and 24 km. Model results are consistent with the established understanding that $E_r$ dominates the planetary and synoptic ranges of $E_h$. $E_d$ dominates the mesoscale energy in the stratosphere, while $E_d$ and $E_r$ approach the same order of magnitude towards smaller scales in the troposphere, in agreement with Skamarock and Klemp (2008). The models do not show large deviations from a $\kappa^{-5/3}$ scaling of $E_d$ for spherical wavenumbers $l > 10$ with slopes $-1.6 \pm 0.02$, except for ICON in the stratosphere ($1.28 \pm 0.01$). $E_r$ follows $\kappa^{-3}$ over a wide range but flattens
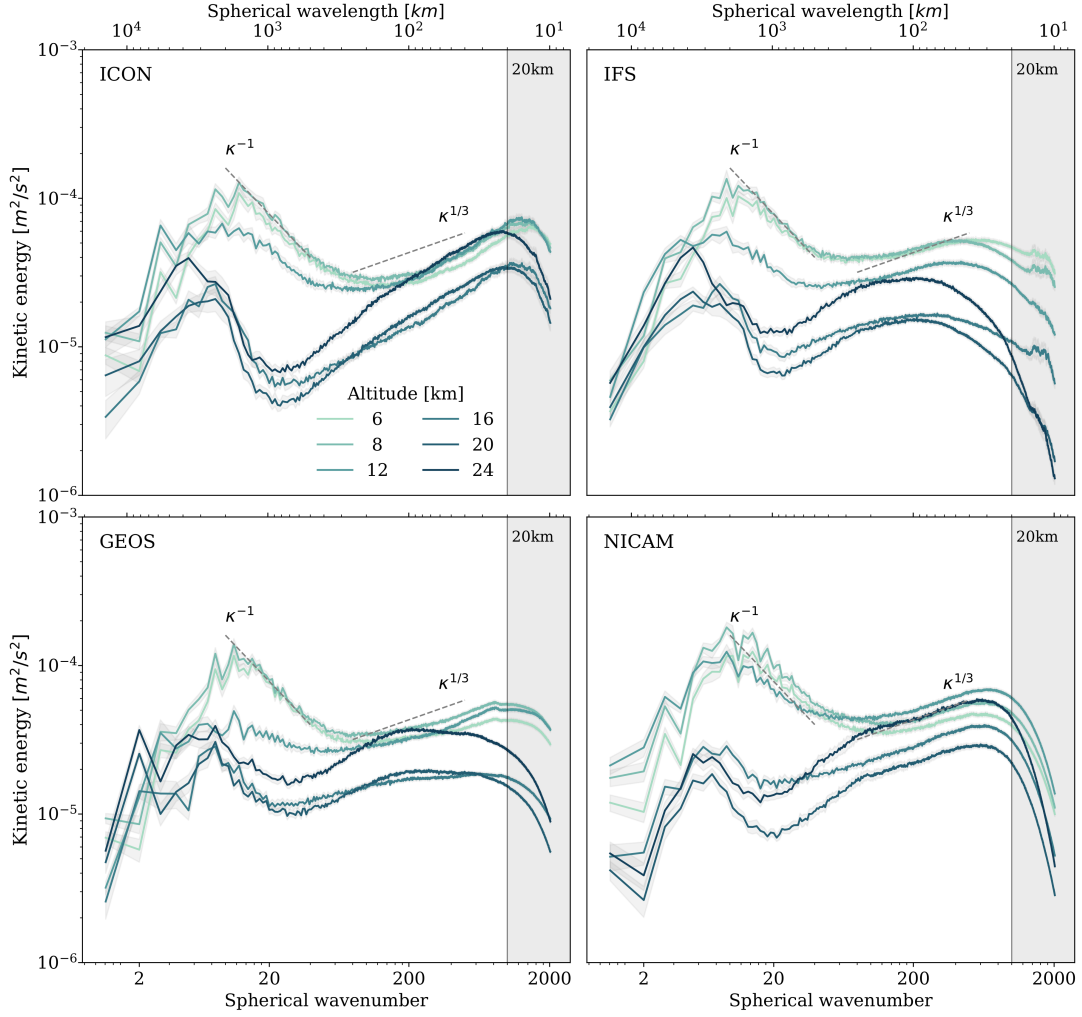
**Figure 3.4:** Vertical kinetic energy spectra as a function of spherical wavenumber for ICON, IFS, NICAM and GEOS at heights of 6, 8, 12, 16, 20 and 24 km. Reference slopes of $\kappa^{-1}$ and $\kappa^{1/3}$ are shown in gray dashed lines. The gray shaded area indicates horizontal wavelengths < 20 km.

towards the smaller scales. The flattening of $E_r$ slopes is present in all models in the troposphere at scales $\lesssim 100$ km, confirming the results of Waite and Snyder (2013) based on idealized baroclinic wave simulations with 12.5 km resolution. Meanwhile, in the stratosphere, the flattening of $E_r$ occurs at scales of about 400–500 km in ICON, agreeing with Hamilton et al. (2008). However, it is not evident in IFS and GEOS.

Oftentimes $E_{IG_h}$ is approximated by $E_d$. However, IGWs can have nonzero rotational energy. As shown in Fig. 3.5, $E_{IG_d} \leq E_{IG_h}$, where the equality holds at mesoscales. The IFS's stratospheric $E_{IG_h}$ at large scales shows different behavior compared to ICON and GEOS in that a greater fraction of $E_r$ projects into IGW modes (see Fig. 3.5). Žagar et al. (2017) showed for the ERA-Interim and ECMWF operational analyses that the excess rotational energy in the IGW modes stems from the gradient wind balance within the stratospheric polar vortex (Žagar et al., 2015). Figure 3.5 suggests that ICON's shallow mesoscale slope found in the lower stratosphere, where $E_h \propto \kappa^{-1.24}$, is not explained by linear IGW modes since $E_{IG_h}$ has a significantly smaller magnitude than $E_h$, and follows slopes close to $\kappa^{-5/3}$.

The modal decomposition filters some divergent energy at small scales due to the insufficient vertical truncation, i.e., the number of vertical modes is smaller than the number of model levels (Žagar et al., 2017). Note that the stratospheric mesoscale magnitudes and slopes of $E_{IG_h}$ and $E_r$ are of the same order in ICON, whereas $E_{IG_h}$ dominates the mesoscale energy in the other models.
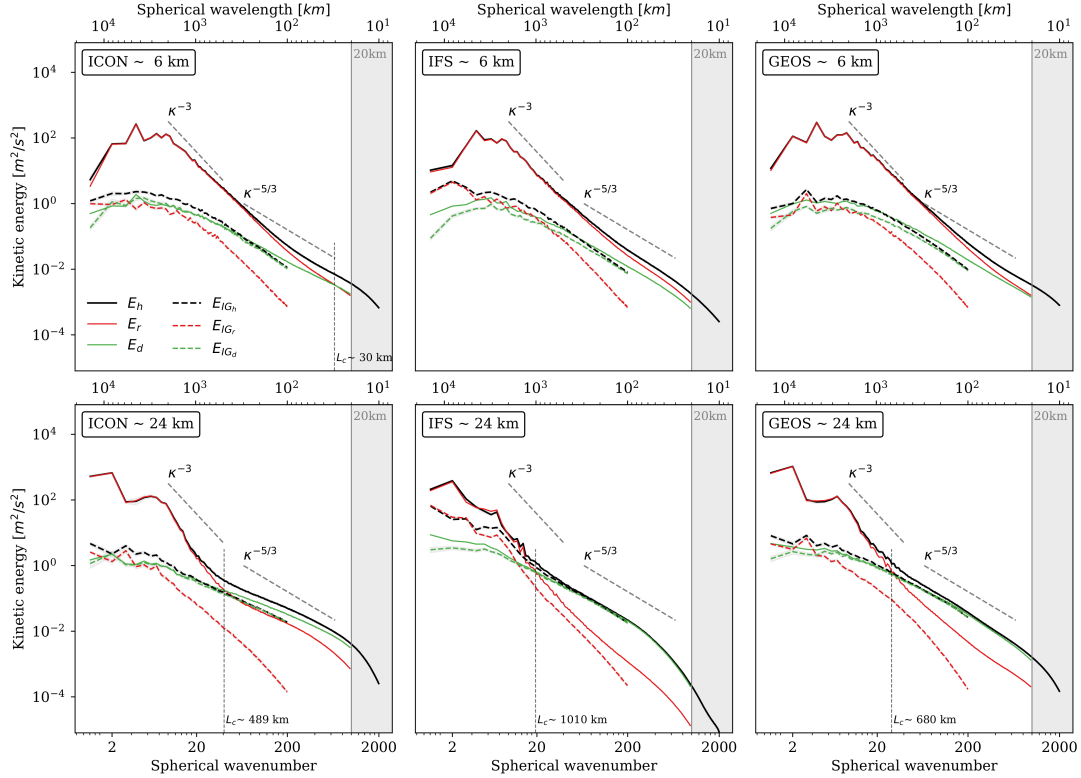


**Figure 3.5:** Kinetic energy spectra of the total horizontal wind field (solid black); rotational (red) and divergent (green) kinetic energies for ICON, IFS and GEOS at (top) 6 km and (bottom) 24 km. The total IGW energy spectra ($E_{IG_h}$) are shown in dashed black lines, along with divergent (dashed green) and rotational (dashed red) IGW kinetic energy components. Vertical dotted lines denote the crossing scale ($L_c$) where $E_r$ and $E_d$ intersect. The gray shaded area indicates horizontal wavelengths $< 20$ km.

Figure 3.6 shows $E_w$ and $E_{IG_w}$ in the troposphere (6 km) and the stratosphere (24 km). $E_w$ is almost fully explained by the horizontal IGW circulation, as expected, because the spectral shapes of $E_{IG_h}$ and $E_d$ are similar for most scales (Fig. 3.5). Deviations exist where the spectra of $E_{IG_h}$ and $E_d$ differ, as is the case, for example, at planetary scales in ICON and GEOS and at the mesoscales in ICON. At planetary scales, $E_{IG_h} > E_d$ in all models due to contributions from $E_{IG_r}$ to $E_{IG_h}$, which is required to explain the large-scale peak of $E_w$ at spherical wavenumbers 4–10, as will be discussed in section 3.4.

Our results agree with previous high-resolution numerical simulations that explicitly diagnose IGWs (Kitamura and Matsuda, 2010; Terasaki et al., 2011; Žagar et al., 2015) or use divergent energy to approximate IGWs in the mesoscale (Callies et al., 2014). These results suggest that IGWs dominate the mesoscale range on average in the stratosphere, while the mesoscale IGW and balanced components have comparable magnitudes in the troposphere. However, in the stratosphere, ICON shows fractions of
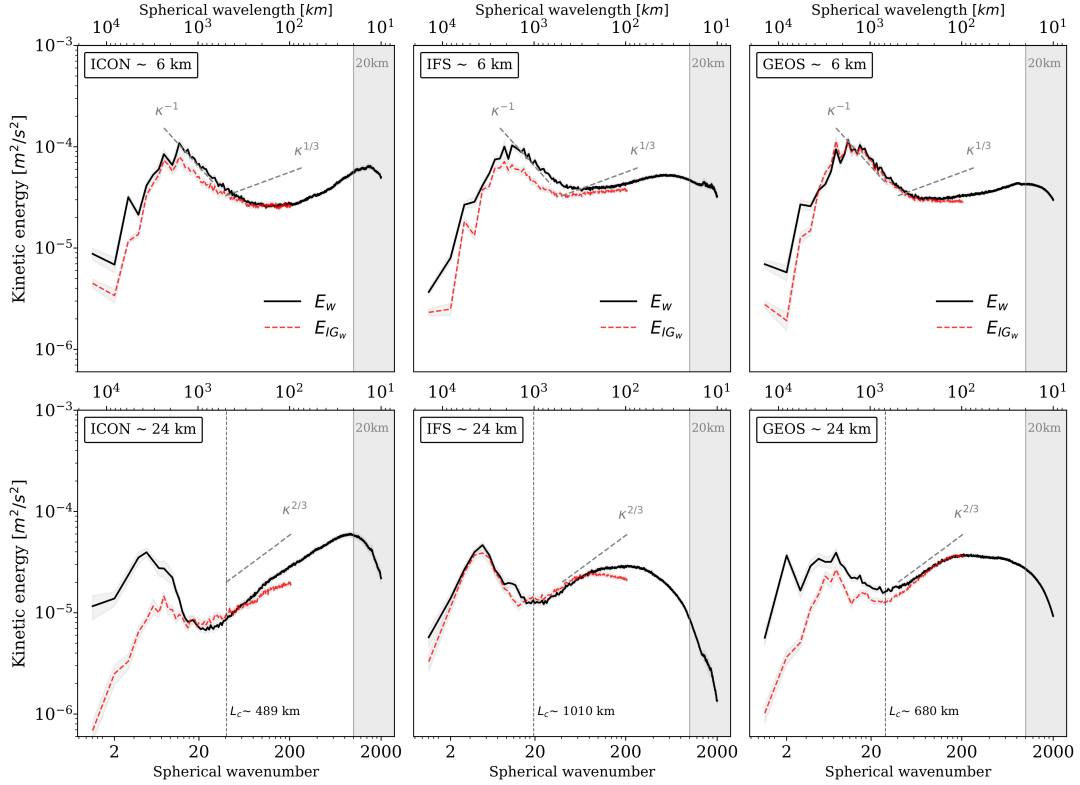
**Figure 3.6:** Vertical kinetic energy spectra $E_w$ (solid black), and estimated IGW vertical kinetic energy spectra $E_{IG_w}$ (red) for ICON, IFS and GEOS at 6 km (upper panel) and 24 km (lower panel). Reference crossing scales ($L_c$) are shown as vertical dotted lines. The gray shaded area indicates horizontal wavelengths $< 20$ km.

$E_d$ and $E_r$ to $E_h$ of around 2/3 and 1/3 at mesoscales, in contrast to IFS and GEOS where $E_d$ dominates.

Differences in the divergent to rotational and horizontal kinetic energy fractions may hint at differences in the underlying dynamics between the models. However, we do not exclude the possibility that the underlying dynamics are not represented correctly due to inadequate vertical resolution or insufficient/excessive vertical mixing, which may lead to spurious gravity waves or noise at small horizontal scales (Waite, 2016). In addition, the overlap between NMF and Helmholtz decomposition and missing information on nonlinear energy transfer makes it difficult to interpret the results in terms of physical processes directly. The following section turns to concepts that allow us to infer the relationship between $E_h$ and $E_w$ without requiring knowledge of the three-dimensional circulations.

## 3.4 MODELS LINKING VERTICAL AND HORIZONTAL MOTION SPECTRA

This section begins with exploring the relationship between $E_w$ and $E_{IG_h}$ at large scales based on the hydrostatic IGW polarization relation. Next, we discuss the

prospect of extending the IGW interpretation of $E_w$ to the mesoscale. Finally, we examine the kinematic link between $E_w$ and $E_d$ through mass continuity at mesoscales, providing a 1D description of the $E_w$ spectrum from divergent horizontal winds at the same vertical level.

### 3.4.1 Large scales

As shown in Fig. 3.6, $E_{IG_w}$ matches $E_w$ reasonably well at most horizontal scales. Dewan (1997), hereafter D97, introduced the Saturated-Cascade Theory (SCT), which provides predictions for the observed $\kappa^{-5/3}$ form of the mesoscale kinetic energy spectra. Additionally, the saturated-cascade theory predicts a scaling for $E_{IG_w}$ directly from the wave polarization relation. For linear inertia–gravity waves, the hydrostatic polarization relation yields

$$E_{IG_w}(\kappa,\hat{\omega}) = \frac{\hat{\omega}^2}{N^2 - \hat{\omega}^2}\left(\frac{\hat{\omega}^2 - f^2}{\hat{\omega}^2 + f^2}\right)E_{IG_h}(\kappa,\hat{\omega}), \tag{3.1}$$

where $\hat{\omega}$ is the intrinsic frequency, and $f$ and $N$ are the inertial and the Brunt–Väisälä frequencies, respectively. D97 further assumes $f^2 \ll \hat{\omega}^2 \ll N^2$ and $\lambda_z < H$, where $\lambda_z$ is the vertical wavelength, and $H \sim 8$ km is the density scale height. The polarization relation under the medium-frequency approximation then takes the simple form

$$E_{IG_w}(\kappa,\hat{\omega}) = \frac{\hat{\omega}^2}{N^2}E_{IG_h}(\kappa,\hat{\omega}). \tag{3.2}$$

The saturated-cascade condition given by (55) in D97 relates the intrinsic frequency with the horizontal wavenumber as $\hat{\omega}^2 = c\epsilon^{2/3}\,\kappa^{4/3}$, where $c$ is a constant and $\epsilon$ is the wave dissipation rate, which implies that only waves with specific frequencies contribute to the spectrum. The spectral relationships in SC theory are strictly one-dimensional so that $E_{IG_w}(\ ) = (\hat{\omega}^2/N^2)E_{IG_h}(\ )$, where ( ) could be $\kappa$, $\hat{\omega}$ or the vertical wavenumber $m$. Eliminating $\hat{\omega}$ in (3.2) gives:

$$E_{IG_w}(\kappa) = c\frac{\epsilon^{2/3}}{N^2}\kappa^{4/3}E_{IG_h}(\kappa) \propto \kappa^{-1/3}. \tag{3.3}$$

The prediction of $E_w$ slopes based on (3.3) is inconsistent with the simulated slopes in all models. In ICON, which exhibits a significantly shallower mesoscale slope $E_{IG_h} \propto -1.24$, (3.3) predicts a flat $E_w$ instead of the observed $E_w \propto \kappa^{2/3}$. This disagreement, however, does not invalidate the interpretation of gravity waves controlling $E_w$. Instead, the saturation and cascade conditions may not co-occur, and the relationship between the wave intrinsic frequency and the horizontal wavenumber may differ from $\hat{\omega} \propto \kappa^{2/3}$. Dewan and Good (1986) introduced the Linear Instability Theory (LIT), which assumes that the saturation amplitude of each wave packet is $N/m$ regardless of the frequency or horizontal wavenumber, which leads to the prediction of $E_h(m) \sim m^{-3}$. Several observational studies have corroborated this prediction (Smith et al., 1987; Allen and Vincent, 1995; Zhang et al., 2017), but not necessarily confirm either the LIT or the SCT. Figure 3.7 shows vertical wavenumber spectra of horizontal $E_{IG_h}(m)$ and vertical $E_{IG_w}(m)$ kinetic energies calculated from

the IGW fields of ICON, IFS, and GEOS. All models show $E_h(m)$ consistent with the theoretical $m^{-3}$ at vertical wavelengths $\lambda_z \sim$ 2–8 km, followed by a transition to a shallower $m^{-5/3}$ regime at $\lambda_z \sim 2$ km, identified as the buoyancy wavenumber. This behavior is consistent with a saturated wave spectrum $\lambda_z > 2$ km. For vertical scales smaller than the buoyancy wavenumber, the spectrum is governed by turbulence and follows a spectral slope of $m^{-5/3}$. In contrast, $E_w(m)$ follows approximately $m^{-3}$ at wavelengths $< 6$ km.

The assumption of LIT and SCT seems to hold for vertical scales (3 km $< \lambda_z <$ 8 km), which implies that the shape of the vertical wavenumber spectrum does not depend on wave frequency; therefore, the joint $(m, \hat{\omega})$ spectrum of horizontal and vertical winds are separable for this vertical wavenumber range. We follow this assumption of separability using a one-dimensional frequency spectrum of the form $B(\hat{\omega}) \propto \hat{\omega}^{-p}$, where $p \sim 5/3$ (Gardner, 1996). Using the standard Jacobian transformation, one can obtain the one-dimensional spectrum $E_{IG_h}(\kappa) = E_{IG_h}(m)|dm/d\kappa|$, and similarly for $E_{IG_w}(\kappa)$. These assumptions are rather crude, and in fact, some studies have indicated the non-separability of the joint $(m, \hat{\omega})$ spectrum (Gardner, 1996; Gardner et al., 1998). However, they allow us to relate $E_{IG_w}(\kappa, z)$ and $E_{IG_h}(\kappa, z)$ at fixed heights using (3.1), and compare them to the model's spectra.
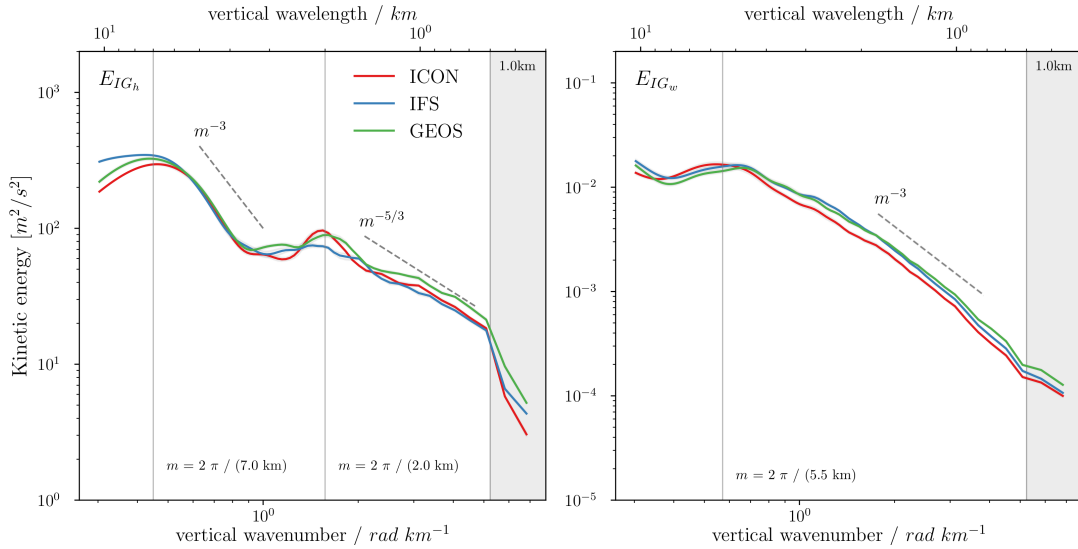


**Figure 3.7:** Vertical wavenumber spectra of the IGW modes for (left) the horizontal kinetic energy, and (right) the vertical kinetic energy for ICON, IFS and GEOS. Reference slopes for $m^{-3}$ and $m^{-5/3}$ are shown in gray dashed lines. The gray shaded area indicates vertical wavelengths $< 1$ km.

In the following, we suggest an alternative derivation of $\hat{\omega}(\kappa)$. From the linear vorticity equation, we have for inertia–gravity waves (Li and Lindborg, 2018):

$$R = \frac{E_{IG_d}}{E_{IG_r}} = \frac{\hat{\omega}^2}{f^2}, \qquad (3.4)$$

which is true for each Fourier mode of a wave field regardless of its vertical structure. Equation (3.4) implies that the relationship $\hat{\omega}(\kappa)$ is determined by $R(\kappa)$, provided that $E_{IG_d} \geq E_{IG_r}$ or $R \geq 1$, so that $\hat{\omega} \geq f$. The equality $R = 1$ holds at large scales

for pure inertial waves. The scale at which $E_{IG_d}$ becomes larger than $E_{IG_r}$ is defined as $L_{IG_c}$.

Figure 3.8 shows $R(\kappa)$ at different altitudes in the troposphere and stratosphere. We focus on the $R \geq 1$ region in what follows. The IFS shows a scaling of $R(\kappa)$ that follows $\kappa^{4/3}$ closely at scales $l \gtrsim 10$ in the stratosphere, which implies $\hat{\omega} \propto \kappa^{2/3}$, consistent with the saturated-cascade hypothesis. In the troposphere, the slope is only slightly flatter than $\kappa^{4/3}$. Meanwhile, ICON and GEOS deviate sooner from $\kappa^{4/3}$, following a scaling closer to $\kappa^2$ at scales $\gtrsim 800$ km. Models show more similar slopes in the troposphere than the stratosphere, with $R$ being approximately an order of magnitude smaller in the troposphere compared to the stratosphere. Furthermore, it is possible to verify that the vertical wavelengths are within the applicability limits of (3.2), namely $\lambda_z < H$, by using estimates of the intrinsic frequency from $R(\kappa)$ in the gravity-wave hydrostatic dispersion relation:

$$m^2 = \frac{\kappa^2(N^2 - \hat{\omega}^2)}{\hat{\omega}^2 - f^2}, \tag{3.5}$$

where $m = 2\pi/\lambda_z$ is the vertical wavenumber. In the troposphere, the models present $\lambda_z \sim 4$ km at mesoscales, while $\lambda_z$ ranges from 4 km to around 6 km in the stratosphere.
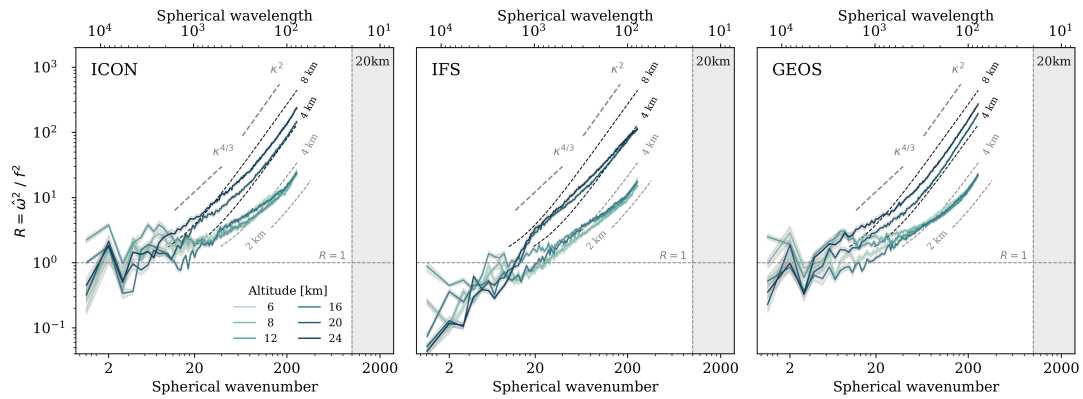


**Figure 3.8:** Ratio $R$ of divergent $E_{IG_d}$ to rotational $E_{IG_r}$ kinetic energies as a function of spherical wavenumber for ICON, IFS and GEOS at 6, 8, 12, 16, 20 and 24 km. Vertical wavelengths are shown in dashed lines for the troposphere (gray) and the stratosphere (black). Reference slopes for $\kappa^{4/3}$ and $\kappa^2$ are shown in gray dashed lines. The horizontal dashed line corresponds to $R = 1$. The gray shaded area indicates horizontal wavelengths $< 20$ km.

As a consequence of (3.4), it follows that the intrinsic frequency can be approximated using $\hat{\omega}/f = \sqrt{R}$. Figure 3.9 shows $\hat{\omega}/f$ estimated from the zonally averaged ratio of divergent and rotational kinetic energies in physical space at 6 and 24 km for ICON, IFS, GEOS, and the ERA5 reanalysis. These results show near-inertial frequencies in the lower stratosphere ($2.0f$ to $2.5f$) and higher ($2.0f$–$3.5f$) in the troposphere. These estimates of $\hat{\omega}$ are consistent with the medium-frequency approximation of the polarization relation. The models show considerable differences regarding the meridional distribution of $\hat{\omega}/|f|$; however, they consistently exhibit higher intrinsic frequencies in the troposphere compared to the stratosphere at mid-latitudes in the northern hemisphere and the opposite behavior in the southern hemisphere. Further, ICON and GEOS show values of $\hat{\omega}/|f|$ approximately constant

at mid-latitudes in the troposphere. In contrast, in the lower stratosphere, $\hat{\omega}/|f|$ systematically decreases with latitude in the southern hemisphere and from the Equator to around 60°N. In the IFS and ERA5, $\hat{\omega}/|f|$ are almost identical and consistent with linear IGW theory ($\hat{\omega}/|f| > 1$) at the latitude band 40°S–40°N. To verify these estimates, we compare the meridional distribution of $\hat{\omega}/|f|$ shown in Fig. 3.9 to the results of Geller and Gong (2010) (their Fig. 1a), which were calculated using kinetic to potential energy ratios based on radiosonde data (1998–2006). This comparison indicates that ICON and GEOS provide a better match to radiosonde observations, at least in the northern hemisphere.

Geller and Gong (2010) showed that the intrinsic frequency computed from averaged energy ratios using polarization relations is consistently smaller than the average intrinsic frequencies calculated with the Hodograph method for each radiosonde sounding by approximately a constant factor. We assume here that $\hat{\omega}$ in (3.1) is proportional to that obtained from (3.4) resulting in $\hat{\omega}^2 = \alpha R f^2$, where $\alpha > 0$. For convenience we define $R' = \alpha R$. The proportionality factor $\alpha$ accounts for the effect of wave superposition modulating the wave frequencies, and amplitudes since (3.1) is only exact for monochromatic waves (Fritts, 1984).

Eliminating the intrinsic frequency in (3.2) using $\hat{\omega}^2 = R' f^2$, we obtain the following approximation for the IGW vertical kinetic energy:

$$E_{LS_w}(\kappa, z) = \frac{f^2}{N^2} R'(\kappa, z) E_{IG_h}(\kappa, z). \tag{3.6}$$

Note that (3.6) is highly sensitive to the values of Prandtl's ratio $f/N$. We use the value of the Coriolis frequency $f$ at mid-latitudes (i.e., $f$ at 45°), and $N(z)$ is approximated by a stepwise function of altitude, which takes values $N = 0.012$ rad/s in the troposphere and $N = 0.026$ rad/s in the stratosphere.

Figure 3.10 shows the prediction of (3.6) and $E_w$. In a statistical sense, the analytical model derived in this section explains to first order the vertical velocity spectra for a wide range of horizontal scales and predicts the average vertical kinetic energy at large scales (500–2000 km), save for the proportionality factor $\alpha$. We estimate $\alpha$ using a non-linear least-squares regression of (3.6) to the models' spectra. The parameter $\alpha$ consistently decreases with height; however, it varies significantly between models. In ICON, $\alpha$ ranges from approximately 0.26 in the stratosphere to 0.65 in the troposphere, in GEOS from 0.2 (stratosphere) to 1.0 (troposphere), and from 0.36 (stratosphere) to 2.0 (troposphere) in IFS.

The tropospheric slopes of $E_{LS_w}$ range from $-1$ to $-1/3$ at scales 400 km $\lesssim \lambda_h < L_{IG_c}$, which matches the slopes of $E_w$ in all models. In the stratosphere, the predicted slopes are consistent with the $E_w$ slopes in GEOS, while for ICON and IFS, the prediction fails to capture the large-scale slopes. In addition, (3.6) captures the observed slope transition of $E_w$ in the stratosphere, mainly through changes in the slope of $R(\kappa)$ since $E_h$ does not deviate significantly from $-5/3$ for spherical wavenumbers $l > 10$. In the stratosphere, ICON and GEOS exhibit a slope transition to the mesoscale with slopes close to $2/3$ and $1/3$, respectively. In contrast, IFS shows a scaling of $\kappa^{-1/3}$ consistent with the wave saturation hypothesis.

We note that (3.6) largely underestimates the magnitude of $E_w$ at mesoscales. In Polichtchouk et al. (2022), it is demonstrated that most of the mesoscale vertical velocity variance is owing to the tropical region. At the same time, the large-scale peak in the global $E_w$ is associated with extratropical systems, such as baroclinic instability at scales $\sim 4000$ km. Consistent with the estimates of $\hat{\omega}$ shown in Fig. 3.9, the models agree on the occurrence of higher averaged intrinsic frequencies in the Tropics and near-inertial frequencies towards the poles. It is therefore not surprising that (3.6), which includes waves $f^2 \ll \hat{\omega}^2 \ll N^2$ and is less sensitive to high-frequency IGWs than (3.1), is not representative of the mesoscale $E_w$.
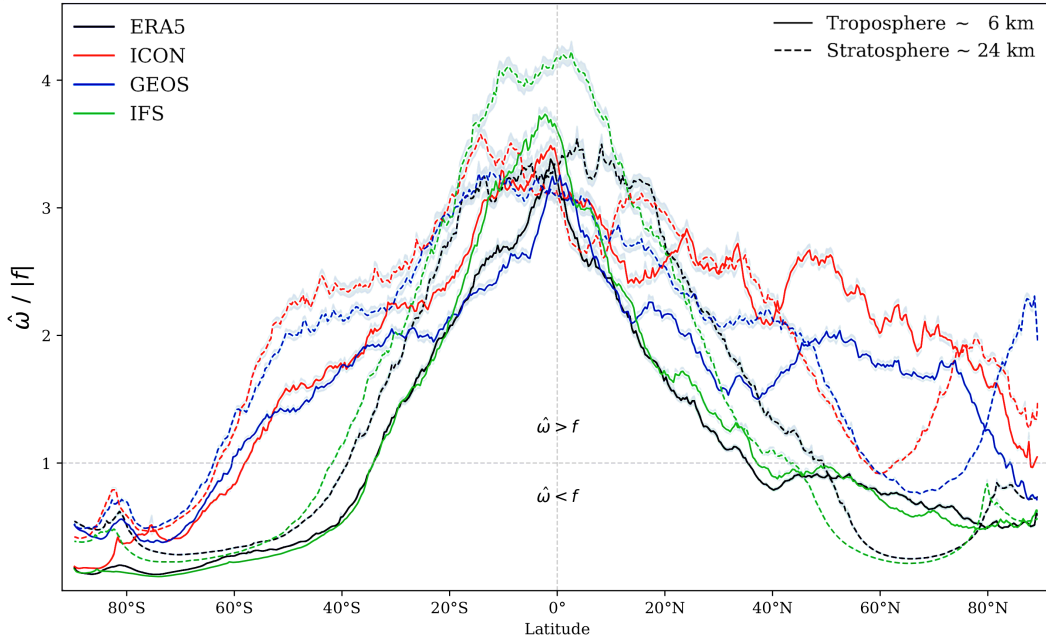


**Figure 3.9:** Meridional distribution of the zonally averaged ratio of intrinsic to inertial frequency $\hat{\omega}/|f| = \sqrt{R}$ at 6 km (solid) and 24 km (dashed) for models ICON, GEOS and IFS. ERA5 reanalysis is shown for reference in black. Dashed gray lines delimit $\hat{\omega} = |f|$. The standard deviation is shown as a shaded area for each line.

Skamarock et al. (2014) suggested that the synoptic-scale peak in the vertical kinetic energy spectra is related to vertical motions associated with large-scale waves. Most of the large-scale vertical kinetic energy in the stratosphere seems to be associated with spontaneously generated IGWs from imbalances around the polar vortex (see Fig. 2.3e), which are persistent throughout the analysis period. In the free troposphere, orographically generated waves might be significant in explaining some of the large-scale vertical kinetic energy. However, the fact that gravity-wave polarization relations well describe the large-scale $E_w$ through (3.6) does not imply that freely propagating IGWs dominate the synoptic scales.

An alternative explanation is that the synoptic-scale peak in the free troposphere comes from balanced vertical velocity associated with mid-latitude baroclinic waves, which project onto the linear IGW modes. In fact, Fig. 3.11 suggests that most large-scale structures in the tropospheric vertical velocity field for ICON are related to baroclinic jet fronts and topographic effects. From a scaling analysis of the linearized
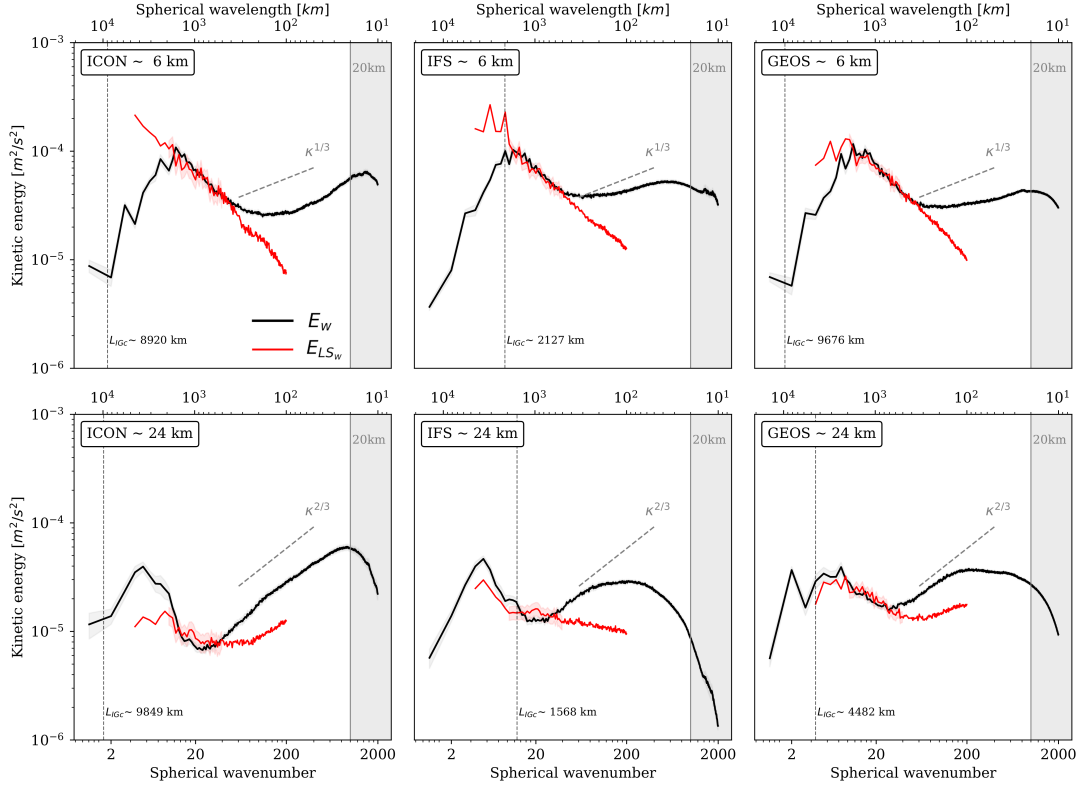
**Figure 3.10:** Vertical kinetic energy spectra $E_w$ as a function of spherical wavenumber for ICON, IFS and GEOS in the troposphere (6 km) and stratosphere (24 km). The vertical velocity spectra $E_{LS_w}$ calculated with (3.6) are shown in red. The shaded area around each line indicates the 95% confidence bands from the uncertainties in the model parameters. Vertical dotted lines denote the crossing scale $L_{IG_c}$ where $E_{IG_d}$ and $E_{IG_r}$ intersect. The gray shaded area indicates horizontal wavelengths $< 20$ km.

QG equations, considering only the leading-order terms, we have for the balanced vertical kinetic energy (Dritschel and McKiver, 2015):

$$E_w \sim Ro^2 \frac{f^2}{N^2} \left( \frac{fL}{NH} \right)^2 E_h, \tag{3.7}$$

where $L$ and $H$ are the horizontal and vertical characteristic length scales. The Rossby number, $Ro$, can be approximated as the ratio of ageostrophic velocity, $u_a$, to geostrophic velocity, $u_g$, i.e., $Ro \sim |u_a|/|u_g|$. At large scales, the horizontal kinetic energy, $E_h$, is dominated by geostrophic flow ($E_h \sim u_g^2$), while $E_{IG_h}$ is mostly ageostrophic ($E_{IG_h} \sim u_a^2$). Therefore, it follows that $E_{IG_h} \sim Ro^2 E_h$. This relationship allows us to express (3.6) in terms of $E_h$ as $E_w \sim Ro^2 (f/N)^2 R' E_h$. This expression is consistent with (3.7) when $R' \sim (fL/NH)^2$. The validity of the QG approximation requires $(fL/NH) \sim 1$, implying that $\alpha R \sim O(1)$. As shown in Fig. 3.8, $R$ ranges from 0.5 to 4 at scales $L \sim 2000$–3000 km, which is consistent with the values of $\alpha^{-1}$ independently estimated for each model at different levels. This scaling analysis suggests that the observed large-scale peak in $E_w$ may result from QG balanced vertical motions that still satisfy (3.6).
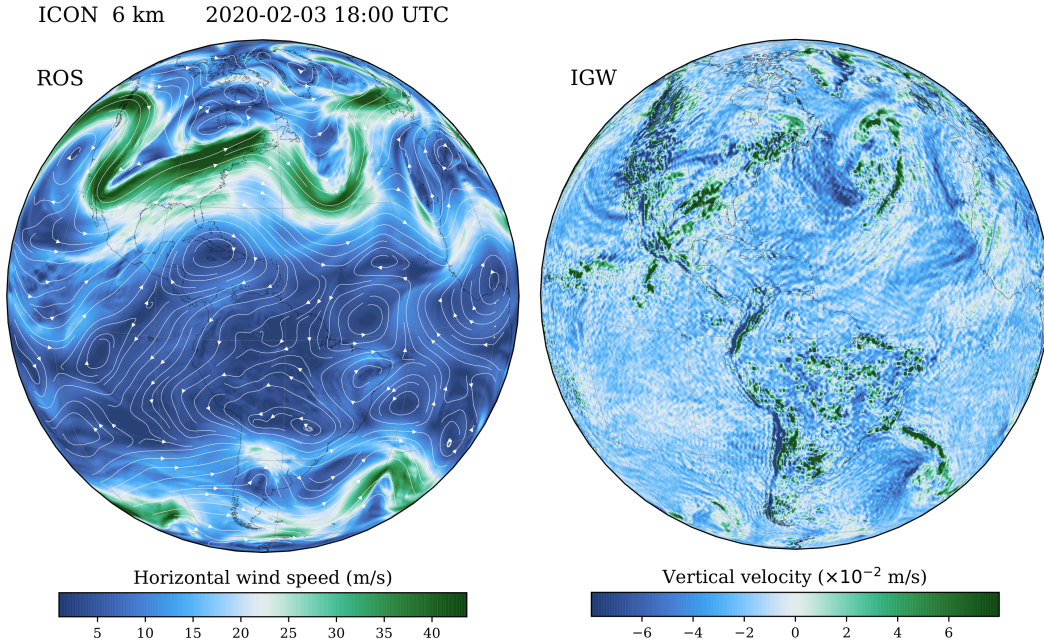
**Figure 3.11:** Snapshot of the modal decomposition of the atmospheric circulation performed on ICON in the free troposphere (6 km), corresponding to 1800 UTC on 3 February 202 for (left) the horizontal wind speed associated with the Rossby modes, and (right) the vertical velocity of IGWs modes. Maps are in orthographic projection centered at the Equator and 65° W.

Wang and Bühler (2020), hereafter WB20, developed a method to incorporate weakly nonlinear ageostrophic corrections into the linear wave-vortex decomposition from one-dimensional aircraft measurements using a statistical QG omega equation. This approach was motivated by the fact that nonlinearities can cause a non-zero vertical velocity field associated with the balanced flow that projects onto linear IGW modes. Their results suggest that IGW modes are robust to nonlinear effects in the lower stratosphere, even at large scales. However, it still needs to be determined whether linear IGW modes are also robust in the upper troposphere. Because we cannot directly quantify the nonlinear projection of vortical energy onto the IGW modes, our analysis does not allow for a definitive conclusion on the cause of the large-scale peak in the vertical kinetic energy spectrum. Applying WB20's approach to analyze 3D global DYAMOND-like simulations might be valuable to shed light on whether the large-scale $E_w$ in the upper troposphere is due to linear IGWs rather than vertical motions associated with the balanced ageostrophic flow.

The following section discusses a general interpretation of the relationship $E_w/E_d$ based on mass continuity in the incompressible limit. Additionally, we show that the $E_w$ positive slopes in the mesoscale end of the spectrum also emerge from the hydrostatic IGW polarization relation if one allows for higher frequency IGWs.

### 3.4.2 Mesoscales

Vertical velocity $w$ is related to the horizontal wind components $u$ and $v$ by mass continuity. A scale analysis of the continuity equation shows that for large-scale motions the mass flux is non-divergent, $\nabla \cdot (\rho \boldsymbol{v}) = 0$, also known as the anelastic approximation, where $\boldsymbol{v} = (u, v, w)$ and $\rho$ is the air density. Neglecting horizontal variations in density at surfaces of constant height, [i.e. $\rho = \rho_0(z)$] gives $\nabla \cdot \boldsymbol{v} - w/H_\rho = 0$, where $H_\rho = -\rho_0 (\partial \rho_0 / \partial z)^{-1}$ is the density vertical length scale ($\sim 8$ km). If we make the additional assumption that the vertical length scale of the circulation is much smaller than $H_\rho$, then $\nabla \cdot \boldsymbol{v} = 0$ (i.e., incompressible flow). This kinematic link between horizontal and vertical motions provides a framework for deriving a quantitative model of vertical velocity spectra for a wide range of spatial scales from the surface layer to the lower stratosphere. Such models have been discussed in previous studies (e.g. Peltier et al., 1996; Tong and Nguyen, 2015; Schumann, 2019).

Following Schumann (2019), hereafter S19, integrating the continuity equation from the ground ($z = 0$) to a height $z = h$ with boundary conditions $w(0) = 0$ yields

$$w(h) = -\int_0^h \left( \frac{\partial u}{\partial x} + \frac{\partial v}{\partial y} \right) dz = -h \left( \frac{\partial \bar{u}}{\partial x} + \frac{\partial \bar{v}}{\partial y} \right), \tag{3.8}$$

where $\bar{u}$ and $\bar{v}$ denote the vertically averaged wind components.

The Fourier modes of the wind components ($\hat{u}$, $\hat{v}$, $\hat{w}$), also satisfy (3.8), from which follows that

$$\hat{w}\hat{w}^* = h^2 \left[ \kappa_x^2 \hat{\bar{u}}\hat{\bar{u}}^* + \kappa_x \kappa_y (\hat{\bar{u}}\hat{\bar{v}}^* + \hat{\bar{v}}\hat{\bar{u}}^*) + \kappa_y^2 \hat{\bar{v}}\hat{\bar{v}}^* \right]. \tag{3.9}$$

The second term on the r.h.s of (3.9) accounts for the mean correlations between $u$ and $v$, which are small in the mesoscales. We can eliminate the cross-correlation term using the vertical component of vorticity ($\zeta$) in Fourier space. The Fourier coefficients of $\zeta$ relate to the horizontal wind through $\hat{\zeta} = i\kappa_x \hat{v} - i\kappa_y \hat{u}$. After vertically integrating $\hat{\zeta}$ using the same limits as in (3.8) and multiplying by its complex conjugate, one obtains the horizontal wavenumber spectrum of the vertical vorticity as follows

$$\hat{\bar{\zeta}}\hat{\bar{\zeta}}^* = \kappa_x^2 \hat{\bar{v}}\hat{\bar{v}}^* - \kappa_x \kappa_y (\hat{\bar{u}}\hat{\bar{v}}^* + \hat{\bar{v}}\hat{\bar{u}}^*) + \kappa_y^2 \hat{\bar{u}}\hat{\bar{u}}^*, \tag{3.10}$$

where $\hat{\zeta}$ relates to the rotational kinetic energy as $E_r = \hat{\zeta}\hat{\zeta}^*/(2k^2)$ and the divergent kinetic energy is simply $E_d = E_h - E_r$. Inserting (3.10) into (3.9) gives:

$$E_w(\kappa, h) = (h\kappa)^2 \bar{E}_d(\kappa), \tag{3.11}$$

where $E_w = \hat{w}\hat{w}^*/2$ is the horizontal wavenumber spectrum of vertical velocity at height $h$, $\bar{E}_d = (\hat{\bar{u}}_d \hat{\bar{u}}_d^* + \hat{\bar{v}}_d \hat{\bar{v}}_d^*)/2$ denotes the kinetic energy spectra computed from vertically averaged spectral coefficients of the divergent winds. Note that (3.11) is only exact in a horizontally isotropic atmosphere with constant density at height $h$.

To allow comparisons of (3.11) with modeled $E_w(k, h)$ and $E_d(k, h)$ at a given $h$, S19 proposed that $\bar{E}_d(k, h)$ and the horizontal spectra of divergent kinetic energy

$E_d(k,h)$ are proportional, at sufficiently large scales ($h\kappa \ll 1$). Considering $\bar{E}_d(k,h) = \beta^2 E_d(k,h)$, and inserting in (3.11) gives

$$E_{MC_w}(\kappa,h) = (h_e\kappa)^2 E_d(\kappa,h), \qquad \text{for} \quad h\kappa \ll 1 \tag{3.12}$$

where $h_e = \beta h$ denotes the "effective height" controlled by the parameter $\beta$ and measures the depth of layers with effectively uniform divergent flow (Schumann, 2019). The physical interpretation of $\beta$ depends on the application. In S19's interpretation, $\beta$ encodes the vertical coherence of the profiles of divergent horizontal velocities. For example, in a barotropic flow in a layer of depth $h$, $\beta \to 1$ and $\bar{E}_d(k,h) \approx E_d(k,h)$. In Peltier et al. (1996), a similar parameter was associated with surface layer stability. These two interpretations are equivalent in the free convective regime where the mean vertical wind shear decreases (Businger, 1973), and $\beta \to 1$. In the following, we investigate to what extent $E_{MC_w}$ is a good approximation of mesoscale $E_w$ for the different models.

Figure 3.12 shows the ratio $E_w/E_d$ scaled by $(h\kappa)^2$ at different model levels for ICON, IFS and GEOS. This ratio shows a scaling close to $\kappa^2$ at mesoscales as predicted by (3.12). However, this scaling breaks at scales $\sim 100$ km in the troposphere and larger scales in the lower stratosphere. These breaks presumably occur at scales where the spatial variability of density is not negligible, and therefore, the assumption of incompressibility does not hold. From a nonlinear least-squares regression of (3.12) to model spectra, we estimate $\beta$ at each vertical level. The value of $\beta$ varies from approximately 0.49–0.66 in the troposphere to around 0.11–0.13 in the stratosphere. The parameter $\beta$ decreases with height due to small vertical correlations of horizontal motions between the stratosphere and the troposphere. S19 reported values of $\beta = 0.5$ at $h = 9.5$ and 0.05 at 17 km, resulting in $h_e = 5$ and 1 km, respectively, based on MPAS 3km simulations. In the DYAMOND simulations, we observe less pronounced variations of $h_e$, which slowly decrease with height ranging between 2.6–4 km in all models.
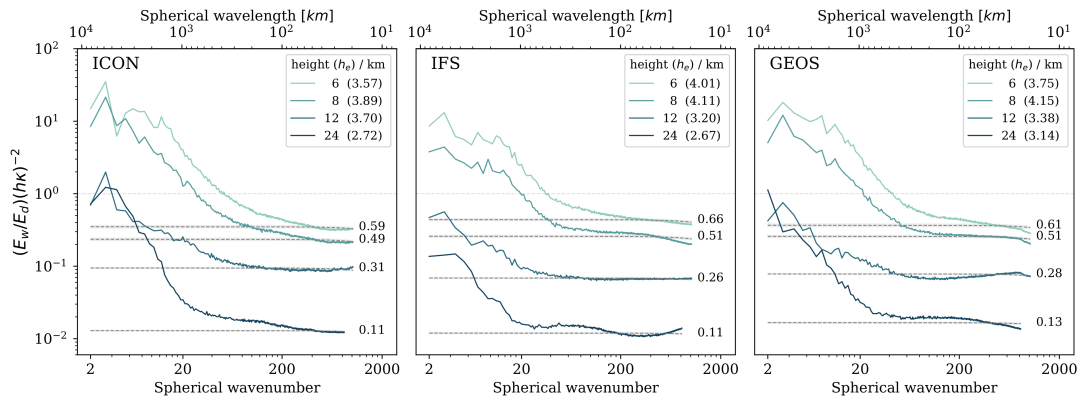


**Figure 3.12:** The ratio of vertical to horizontal divergent kinetic energy scaled by $(h\kappa)^2$, computed for ICON, IFS, and GEOS at levels 6, 8, 12, and 24 km. Horizontal dashed lines correspond to the predictions of $E_{MC_w}$ from the S19 analytical model, and the corresponding $\beta$ coefficient is depicted to the right of each line. Effective height is shown in the inlet, along with the corresponding altitude.

According to (3.12) and assuming that $E_d$ scales as $\kappa^{-5/3}$ at mesoscales, the prediction for the scaling of $E_w$ is $\kappa^{1/3}$. In the troposphere, we observe positive slopes

closer to 1/3, except for ICON, with a steeper slope at scales $< 100$ km (see Fig. 3.6). In the stratosphere, IFS and GEOS show a slope close to 2/3 for scales ($\sim$200–1000 km) and significantly shallower slopes at scales $< 200$ km, while ICON shows the 2/3 slope throughout the stratosphere's mesoscale. ICON's $E_w$ steeper slopes are explained by the shallow $E_d$ slopes of about $-4/3$ (see Table 3.1).

In the following, we explore the relationship between $E_w$ and $E_{IG_h}$ in the mesoscale region. Analytical models of the form (3.12) must also apply to the ratio $E_{IG_w}/E_{IG_h}$ at mesoscales since linear IGW modes satisfy the incompressible continuity equation by definition. A simple approximation for $E_{IG_w}$ can be derived from (3.1) and the dispersion relation (3.5):

$$E_{MS_w}(\kappa) = \tilde{\kappa}^2 h_e^2(\kappa) \ E_{IG_h}(\kappa), \tag{3.13}$$

where $\tilde{\kappa} = \kappa/2\pi$ is the scaled wavenumber in units $(m^{-1})$, and the "effective height" parameter is redefined in terms of gravity-wave vertical wavelengths and intrinsic frequencies as

$$h_e = \lambda_z \left( \frac{\hat{\omega}^2}{\hat{\omega}^2 + f^2} \right)^{1/2} = \lambda_z \left( \frac{R'}{R' + 1} \right)^{1/2}. \tag{3.14}$$

For near-inertial waves $\hat{\omega}/|f| \sim 1$, (3.14) predicts $h_e \sim 0.7\lambda_z$, while in the high-frequency range $\hat{\omega} \sim N$, it gives $h_e \sim \lambda_z$. At mid-latitudes in the stratosphere, where $\hat{\omega}/|f| \sim 2$ (see Fig. 3.9), we have $h_e \sim 0.9\lambda_z$. The estimates of $h_e \sim 0.8\lambda_z$ are consistent with those shown in Fig. 3.12, where $h_e$ is calculated from fitting (3.12) to model spectra, and $\lambda_z$ is calculated from the hydrostatic dispersion relation (see Fig. 3.8).

Note that (3.13) is similar to (3.12), except that $E_w$ is related to $E_{IG_h}$ and the parameter $h_e$ is a function of horizontal wavenumber as it depends on $E_{IG_d}$ and $E_{IG_r}$. Considering $\alpha = 1$, (3.13) simplifies to $E_{IG_w} = (\lambda_z/\lambda_h)^2 \ E_{IG_d}$, which is consistent with the incompressible mass-continuity scaling of IGW wind components. In the high-frequency limit $\hat{\omega} \to N$, (3.13) is less sensitive to $\alpha$, since $E_{IG_h} \to E_d$ and $h_e \to \lambda_z$. For practical applications of (3.13), we use an averaged effective height in the mesoscale region (20–500 km) and values for $\alpha$ of 0.5 and 1.2 in the stratosphere and troposphere, respectively.

Figure 3.13 shows $E_{MS_w}$ and $E_w$ at 6 and 24 km. Notably, $E_{MS_w}$ approximates $E_w$ with high accuracy regarding mesoscale spectral slopes in all models. In particular, the stratospheric large-scale slopes of $E_w$ are captured by $E_{MS_w}$ in IFS. These results suggest that $E_{IG_h}$ is a better predictor of $E_w$ than $E_d$ in the large-scale portion of the mesoscale (200–1000 km). Equation (3.12) accurately predicts the slopes of $E_w$, provided that $E_d$ remains close to $E_{IG_h}$ (see Fig. 3.5). The vertical kinetic energy $E_{MC_w}$ calculated with (3.12) predicts steeper slopes than $E_w$, and therefore a faster energy increase towards small scales. In the troposphere, $E_{MC_w}$ converges towards $E_w$ at scales $\lambda_h < 100$ km. In the stratosphere, especially for IFS and GEOS, one could obtain a better match between $E_{MC_w}$ and $E_w$ at scales $\sim$200–1000 km by increasing $h_e$ to approximately $h_e \sim \lambda_z$, however this results in an overestimation of $E_w$ at shorter scales ($\lambda_h < 100$ km).

Simplified analytical models based on linear IGW polarization relations of the form (3.6) and (3.13) together provide a quantitative description of $E_w$ for a wide range of horizontal scales in the troposphere and the stratosphere. These results are consistent with those obtained by integrating the continuity equation (2.8) from horizontal IGW modes. These results suggest that IGW properties, namely the dominant vertical wavelength and intrinsic frequency, control the effective height and, therefore, the magnitude of $E_w$. The main benefit of the IGW interpretation of $h_e$ is that it links vertical and horizontal kinetic energy spectra, invoking only local wind field information, which can be validated with observations. In principle, we can constrain the $h_e$ parameter at horizontal scales $\sim 200$ km using vertical wavelengths estimated from vertical profiles of horizontal winds and vertical velocities estimated from dropsonde data as demonstrated, e.g., by Bony and Stevens (2019).
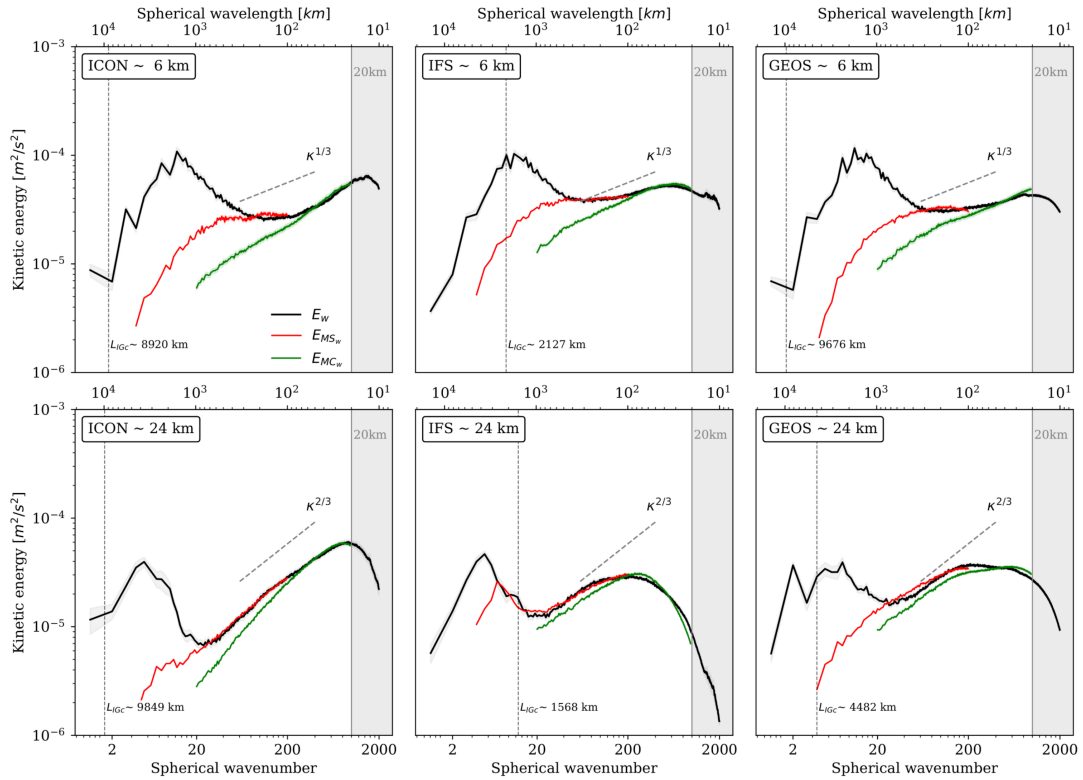


**Figure 3.13:** Vertical kinetic energy spectra $E_w$ as a function of spherical wavenumber for ICON, IFS, and GEOS at (top) 6 km and (bottom) 24 km. The vertical kinetic energy spectra $E_{MC_w}$ calculated with (3.12) and $E_{MS_w}$ are shown in green and red, respectively. The shaded area around each line indicates the 95% confidence bands from the uncertainties in the model parameters. Vertical dotted lines denote the crossing scale ($L_{IG_c}$) where $E_{IG_d}$ and $E_{IG_r}$ intersect. The grey shaded area indicates horizontal wavelengths < 20 km.

## 3.5 SUMMARY AND CONCLUSIONS

This chapter investigates the relationship between horizontal and vertical kinetic energy spectra calculated from global storm-resolving simulations of four numerical models of the DYAMOND experiment. The data analyzed consists of numerical outputs from the

ICON, IFS, GEOS, and NICAM models with horizontal grid spacings $< 5$ km, covering 12 days of the winter experiment. We focus primarily on the relationships between $E_h$ and $E_w$ across all resolved horizontal scales ($\lambda_h > 20$ km). We investigate the role of balanced and unbalanced circulations obtained utilizing normal mode function decomposition, which yields the contribution of IGWs to the horizontal kinetic energy spectra. To estimate the contribution of IGWs to the vertical velocity spectra, we numerically solve the mass continuity equation in physical space from horizontal IGW modes. Additionally, we analyze $E_{IG_r}$ and $E_{IG_d}$ associated with the unbalanced IGWs component. Furthermore, we consider the linearized vorticity equation and hydrostatic IGW polarization relations to link $E_w$ and $E_h$ at large scales and discuss extending the IGW interpretation to the mesoscale region. In addition, we explore the kinematic link between $E_w$ and $E_h$ at mesoscales and shorter scales using an incompressible, isotropic scaling of the continuity equation.

All models exhibit a high degree of agreement on spectral power in the large-scale regime for wavelengths greater than 600–800 km in the free troposphere. The stratospheric spectral slope, however, is slightly steeper than $\kappa^{-3}$—with a similar transition in spectral slopes from large scales to a shallower mesoscale regime in the stratosphere. The mesoscale transition region varies slightly from model to model and occurs consistently at longer wavelengths in the stratosphere compared to the troposphere. In the mesoscale region, the models differ in their magnitudes of kinetic energy per unit mass in the stratosphere, while these differences are less significant in the troposphere. Model results are consistent with the observation that the rotational flow dominates the synoptic range. In contrast, the rotational and divergent components are of the same order in the mesoscale range in the troposphere, and the divergent IGW energy dominates $E_h$ in the stratosphere.

The vertical kinetic energy spectra are relatively flat across all resolved horizontal scales, with evidence of two peaks, one at synoptic scales ($\sim 2000$ km) and one at the smallest resolved scale ($\sim 20$ km). All models predict a similar spectral power related to the maxima found at large scales, while most differences occur in the mesoscale. For example, $E_w$ mesoscale slopes are close to $1/3$ in the troposphere for all models and slightly steeper ($2/3$) in the lower stratosphere in ICON, while in IFS and GEOS, the slopes flatten for $\lambda_h < 100$ km. We show that vertical kinetic energy spectra are explained, to a good approximation, exclusively by horizontal winds over a wide range of horizontal scales.

At the mesoscale, the vertical and horizontal kinetic energy spectra are linked kinematically, as shown by Schumann, 2019. This kinematic link between the horizontal and vertical motions provides a framework for deriving a quantitative analytical model of $E_w$ from knowledge of $E_d$ at a given vertical level. The relationship of $E_w$ to $E_d$ on the mesoscale is best explained by mass continuity in the incompressible limit at scales $< 100$ km, and the ratio $E_w/E_d$ scales to a good approximation as $(h_e\kappa)^2$. The "effective height" is approximately within 2–4 km in all models but depends weakly on the height for each model independently. This variation of $h_e$ is approximately 1 km between the troposphere and stratosphere, consistent with variations of the vertical wavelengths estimated from the gravity-wave dispersion relation. These results suggest that the properties of IGWs, namely the dominant vertical wavelength and the intrinsic frequency, control the "effective height" and, hence, the magnitude of vertical

velocity variance. The main benefit of this interpretation of $h_e$ is that it links $E_w$ and $E_h$, invoking only the wind field information at the same level. IGW characteristics can, in principle, be estimated directly from observations.

At large scales, the proportionality $E_w/E_d \propto \kappa^2$ breaks since the transition in the $E_w$ slopes from negative to positive between global and synoptic scales passing through an energy minimum (at $l \sim 20$ in the stratosphere), has no counterpart in $E_d$. The large-scale maxima found in $E_w$ can be explained to a good approximation by the hydrostatic IGW polarization relation in the mid-frequency limit, where the intrinsic frequencies are inferred from the energy ratio $E_{IG_d}/E_{IG_r}$. A simple analytical model is presented, relating $E_w$ and $E_{IG_h}$ save for a proportionality factor $\alpha$. The value $\alpha$ decreases with altitude from approximately 1.2 in the troposphere to around 0.5 in the stratosphere. The estimates of $\hat{\omega}/f$ from the divergent to rotational IGW energy ratio are consistent with the results presented in Geller and Gong, 2010 based on radiosonde observations. These results show $\hat{\omega}/f$ of around 1.5–2.5 in the stratosphere and a higher ratio of 2–3 in the troposphere, which would be consistent with the hypothesis that IGWs control $E_w$ at large scales. However, the analysis reveals that the large-scale $E_w$ peak appears consistent with QG scaling to first-order; therefore, additional analysis is needed to determine its cause. Nevertheless, the simplified analytical models derived here describe vertical kinetic energy for various spatial scales.

The results of partitioning the circulation into IGW and balanced modes in the lower stratosphere suggest that IGWs dominate mesoscale spatial variability in IFS and GEOS, while these components are of similar order in ICON. In the troposphere, the contributions from IGWs and vortical modes to $E_h$ are similar in all models. The IGW modes explain differences in $E_h$ and, to some degree, differences in $E_w$ because $E_{IG_h}$ governs most of $E_w$ kinematically and through the hydrostatic polarization relation at most resolved scales. Alternatively, $E_w$ could explain the magnitudes of $E_d$ and $E_r$ since energy converts from available potential energy to the kinetic energy of the divergent flow through vertical motions and then to rotational kinetic energy (Lorenz, 1960; Chen and Wiin-nielsen, 1975). However, a quantitative analysis of these energy conversion processes and the interactions involving rotational and divergent modes in global storm-resolving simulations is missing. Regardless of the model discrepancies in the underlying dynamics of horizontal winds, the vertical velocity seems consistent with quasi-linear dynamics. In light of these results, the following chapter investigates the resolved spectral fluxes and energy transfer between horizontal and vertical motions using high-resolution simulations.

# 4 | ENERGY BUDGET IN STORM-RESOLVING SIMULATIONS

*Big whirls have little whirls,*
*that feed on their velocity;*
*and little whirls have lesser whirls,*
*and so on to viscosity.*

— Lewis F. Richardson (1922)

## 4.1 INTRODUCTION

The realization of the observed $\kappa^{-5/3}$ mesoscale spectrum is often used to assess the correctness and dynamical consistency of simulations of Earth's atmosphere. Global circulation models (GCMs) can reliably simulate the large-scale $\kappa^{-3}$ since this spectrum range is related to well-resolved synoptic-scale balanced dynamics. The latest advancements in kilometer-scale modeling may allow us to simulate mesoscale dynamics realistically (Stevens et al., 2019). Recent high-resolution GCMs simulations can readily reproduce the mesoscale spectral characteristics (Hamilton et al., 2008; Terasaki et al., 2009; Skamarock et al., 2014; Stephan et al., 2022; Morfa and Stephan, 2023). However, the success of models at simulating mesoscale phenomena does not necessarily imply consistent underlying dynamics because models can reach the same statistical quasi-equilibrium through different routes. For this reason, more information on spectral energy transfers is needed to interpret model differences regarding physical processes. Several model design and configuration aspects might also impact the horizontal kinetic energy (HKE) spectrum (Skamarock et al., 2014), including convective parameterizations, microphysics, vertical diffusion, and subgrid-scale orography. Parameterized processes introduce energy fluxes that can impact the dynamics by replacing the resolved energy transfers across scales (Malardel and Wedi, 2016).

As demonstrated in Chapter 3, high-resolution GCMs exhibit considerable differences in their simulated kinetic energy spectra. Nevertheless, vertical motions seem consistent with quasi-linear dynamics (Morfa and Stephan, 2023), and the relationship between horizontal and vertical motion spectra is consistent in all the models– whether this result applies to the real atmosphere still needs to be verified with observations. In Chapter 3, we derived semi-empirical spectral models linking horizontal and vertical kinetic energy (VKE) spectra based on mass continuity and IGW polarization relations, which provide a quantitative prediction of the VKE spectral slopes at large scales

and mesoscales. Moreover, the magnitude of the VKE spectrum is controlled by IGW properties, namely the dominant vertical wavelength. These results suggest that IGW modes dominate the VKE spectra at most horizontal scales, whereas an incompressible, isotropic scaling of the continuity equation captures the relationship between VKE and HKE spectra at scales $\lesssim 100$ km (Schumann, 2019). The match between the approximations and modeled VKE spectra suggests that the latter is explained to a good approximation, exclusively by HKE at most horizontal scales. Given these results, we might ask: Do high-resolution simulations of different models also agree on the mechanisms shaping the HKE spectrum at mesoscales?

This chapter explores whether different kilometer-scale global GCMs agree on the mechanism shaping the HKE spectrum at mesoscales. We employ the formulation of the spectral energy budget of the atmosphere developed by Augier and Lindborg (2013), which provides an effective tool for systematically investigating model dynamics. In addition to the AL13 methodology, we use the Helmholtz decomposition of the spectral budget of kinetic energy introduced by Li et al. (2023), which provides insights regarding the interaction between atmospheric rotational and divergent motions. For this purpose, we employ storm-resolving global simulations from the DYAMOND experiment (Stevens et al., 2019), which explicitly models most of the dynamically relevant mesoscale phenomena. We analyze 3-hourly outputs of instantaneous fields for five days starting from January 25, 2020, on constant pressure levels from 1000 hPa to 50 hPa, focusing on the free troposphere ($\sim$ 450–250 hPa) and the lower stratosphere ($\sim$ 250–50 hPa). To interpret the differences between models' kinetic energy spectra regarding physical processes, we investigate the resolved mesoscale energy fluxes from storm-resolving simulations of two state-of-the-art GCMs and the ERA5 as a comparison baseline. The global reanalysis data can resolve the atmospheric energy transfers across many scales; however, it is insufficient to investigate the whole mesoscale range due to limited horizontal resolution. ERA5 comes on a regular latitude-longitude grid, with a horizontal resolution of 0.25° by 0.25°. Our analysis includes ERA5 spectra truncated at wavenumber 512 (horizontal wavelength $\sim$ 78 km). Finally, we explore the contribution of balanced and unbalanced dynamics to the resolved energy fluxes of ERA5, ICON, and the IFS using normal mode function (NMF) decomposition described in section 2.3.

This chapter is structured as follows: Section 4.2 analyzes and compares the resolved compensated kinetic energy spectra and the spectral energy budget among the simulations. Section 4.2.2 examines the vertical distribution of the energy fluxes and the contributions from vertical fluxes to the global budget of kinetic energy. Section 4.3 highlights the different contributions to the energy budget of rotational and divergent kinetic energies, using the Helmholtz decomposition developed by Li et al. (2023) and investigates the contributions from balanced and unbalanced dynamics using the NMF decomposition into linear Rossby waves and IGWs. Finally, section 4.4 discusses the implications of our findings.

## 4.2 ENERGY FLUXES IN STORM-RESOLVING SIMULATIONS

This section investigates the spectral energy budget of two high-resolution global simulations performed with ICON and the IFS. As a baseline for comparisons of globally integrated fluxes, we have included ERA5. The characteristics of the energy fluxes of ERA5 have been extensively discussed in Li et al. (2023); however, the horizontal resolution of the reanalysis data is insufficient to resolve the entire mesoscale range. The simulations investigated here with a major increase in resolution provide an opportunity to better understand the dynamics underlying the HKE spectral transition to the mesoscale $l^{-5/3}$ regime. The following section compares the energy budget and the associated energy spectra, vertically integrated between 1000–50 hPa for the simulations.

### 4.2.1 The global spectral energy budget

Figure 4.1 shows the total kinetic energy transfer ($\Pi_K$) that redistributes energy across scales, split into the linear Coriolis transfer ($\Pi_L$) and the nonlinear spectral kinetic energy transfer ($\Pi_N$), as well as the cumulative energy conversion from available potential energy (APE) to divergent kinetic energy (DKE), denoted as $\mathcal{C}_{A\to D}$, and from DKE to rotational kinetic energy (RKE) denoted as $\mathcal{C}_{D\to R}$. The fluxes are vertically integrated between 1000–50 hPa for the IFS (a) and ICON (b). Panels (c) and (d) of Fig. 4.1 show compensated nondimensional spectra of kinetic energy ($\tilde{E}_K$), available potential energy ($\tilde{E}_A$), and VKE ($\tilde{E}_w$) for the IFS and ICON, respectively. Following Augier and Lindborg (2013), we can obtain the compensated energy spectra by assuming that the mesoscale spectrum results from an inertial subrange due to isotropic turbulence, i.e., $E_K(l) \propto \tilde{\Pi}_K^{2/3} l^{-5/3}$ (Kolmogorov, 1941), where $\tilde{\Pi}_K$ represents the maximum nonlinear kinetic energy transfer at mesoscales. Furthermore, let us consider the total mass of a given pressure layer, approximately equal to $r^2 \Delta p/g$, with $r$ being Earth's radius. From dimensional analysis, the resulting compensated nondimensional spectrum is

$$\tilde{E}_K(l) = C(\Delta p/g)^{-1/3}(r\tilde{\Pi}_K)^{-2/3}l^{5/3}E_K(l), \tag{4.1}$$

where $C$ is a constant of order unity (Augier and Lindborg, 2013).

At first glance, the models agree on the magnitude of most cumulative energy fluxes at large scales except for the globally integrated conversion $\mathcal{C}_{A\to D}(l=0)$, which is roughly 0.8 $W\ m^{-2}$ larger in the IFS. This difference in energy conversion at large scales explains the larger magnitude of $E_D$ in the IFS (Fig. 4.1c) compared to ICON (Fig. 4.1d) at wavenumbers $\sim$ 2–20. The models present a notable downscale cascade of APE in this range of wavenumbers. The large cumulative conversion at synoptic scales and the steep negative slope of $\Pi_A$ giving a spectral transfer from planetary toward synoptic scales can be associated mainly with baroclinic instability (Augier and Lindborg, 2013). In ICON, the downscale cascade of APE, which originates at the planetary scale, approaches zero at $l \sim 40$. In contrast, the IFS shows residual nonlinear APE transfer with a subsequent cascade, consistent with the results of Malardel and Wedi (2016), who attributed this mesoscale APE transfer to the weakness of the
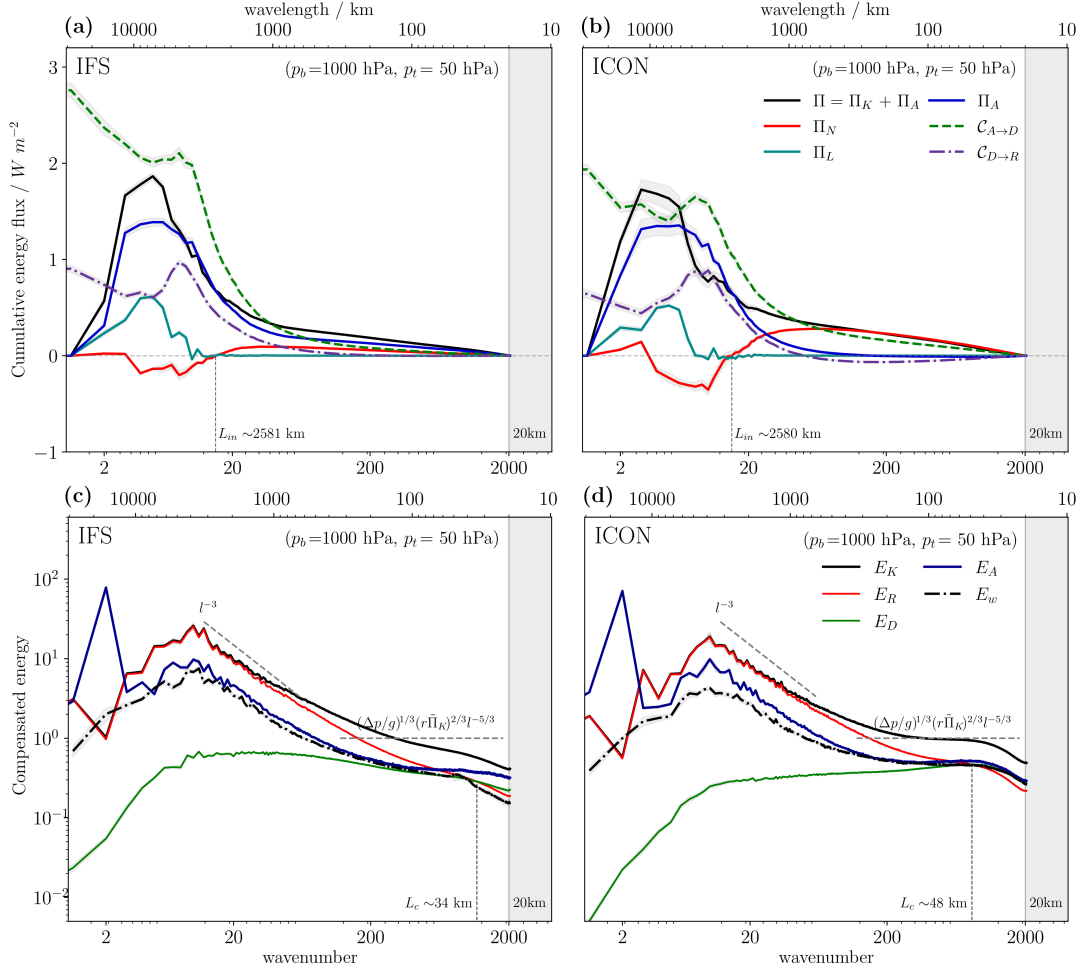
**Figure 4.1:** Cumulative energy fluxes as a function of spherical wavenumber for (a) IFS and (b) ICON. Panels (c) and (d) show compensated nondimensional spectra of APE and kinetic energy components for each model, respectively. Spectral fluxes and energy spectra are vertically integrated within a layer corresponding to $p_b = 1000$ hPa and $p_t = 50$ hPa. Reference slopes of $l^{-3}$ and $l^{-5/3}$ are shown in dashed lines. The maximum HKE nonlinear spectral transfer used for nondimensionalization is $\tilde{\Pi}_K = 0.32\ W\ m^{-2}$, and was calculated from $\Pi_K$ in panel (b). The gray shaded area corresponds to scales smaller than the triangular truncation ($\lambda_h < 20$ km).

conversion of APE into DKE. Notably, the ratio $E_K/E_A$ is approximately 2 in both models, indicating that the total energy is partitioned equally between the two components of HKE and the APE, also consistent with predictions of QG turbulence (Charney, 1971).

The linear HKE spectral transfer $\Pi_L$ shows an evident downscale cascade at planetary scales, which peaks around $l \sim 5$ and has similar magnitudes in both models. This large-scale HKE transfer toward the synoptic scales is mainly associated with the variation of the Coriolis parameter with latitude, which results in a non-negligible background vorticity gradient (i.e., the $\beta$ effect) (Lambert, 1984; Li et al., 2023). The linear Coriolis contribution to the HKE spectral transfer is negligible at wavenumbers $l > 10$, meaning that the spectral energy transfer at mesoscales is primarily due to nonlinear interactions. At synoptic scales (wavelengths 2000–5000 km), the HKE nonlinear transfer $\Pi_K$ is upscale and feeds the large-scale circulation as predicted

| $l$ | ERA5 | | IFS | | ICON | |
|---|---|---|---|---|---|---|
| | 0–20 | 20–511 | 0–20 | 20–2047 | 0–20 | 20–2047 |
| $\Delta\mathcal{C}_{A\to D}$ | 1.70 | 0.73 | 1.97 | 0.78 | 1.17 | 0.77 |
| $\Delta\mathcal{C}_{D\to R}$ | 0.97 | 0.60 | 0.59 | 0.31 | 0.33 | 0.31 |
| $\Delta\Pi_A$ | -0.37 | 0.37 | -0.48 | 0.48 | -0.39 | 0.39 |
| $\Delta\Pi_K$ | -0.01 | 0.01 | -0.06 | 0.06 | -0.11 | 0.11 |
| $\Delta\mathcal{D}_K \simeq \Delta(\mathcal{C}_{A\to D} + \Pi_K)$ | 1.68 | 0.74 | 1.91 | 0.85 | 1.06 | 0.88 |
| $\Delta(\mathcal{G}_A - D) \simeq -\Delta\Pi$ | 0.38 | -0.38 | 0.54 | -0.54 | 0.50 | -0.50 |

**Table 4.1:** Estimation of the spectral energy budget ($W\ m^{-2}$) for ERA5, IFS, and ICON at large scales ($0 \leqslant l \leqslant 20$) and mesoscales ($20 \leqslant l \leqslant N$), where $N$ is the spectral truncation: $N = 2047$ for ICON and the IFS, and $N = 511$ for ERA5. The quantities $\Delta\mathcal{C}_{A\to D}$, $\Delta\mathcal{C}_{D\to R}$, and $\Delta\Pi_{A,K}$ are directly obtained from Fig. 4.1. For example, the net cumulative energy transfer for a given wavenumber range $[l_1, l_2]$ is defined as $\Delta\Pi = \Pi(l_1) - \Pi(l_2)$, and similarly for the energy fluxes.

by Charney (1971). This upscale transfer has been corroborated by spectral analysis with different global reanalysis data (Boer and Shepherd, 1983; Burgess et al., 2013), or more recently using the latest ERA5 dataset (Li et al., 2023). Interestingly, the energy injection scale ($L_{in}$), where $\Pi_K = 0$, is almost identical in the two models with $L_{in} \simeq 2580$ km. This value agrees with the maximum instability scale predicted by QG linear stability theory, indicating that baroclinic instability is the primary source of upscale kinetic energy (Wang et al., 2015).

Table 4.1 summarizes the vertically integrated energy budget assuming stationary energy spectra of APE and HKE. The cumulative fluxes are computed separately for the large planetary and synoptic scales below wavenumber 20 and for the wavenumber range ($20 \leqslant l \leqslant N$) as representative of the mesoscale, where $N = 2047$ is the spectral truncation used for ICON and the IFS. The ERA5 global dataset truncated at $N = 511$ is included as a baseline for comparison of the energy fluxes at large and intermediate scales. The net cumulative conversion $\Delta\mathcal{C}_{A\to D}$ is positive across all scales in the models; with the IFS exhibiting a stronger conversion of $\Delta\mathcal{C}_{A\to D} = 1.97\ W\ m^{-2}$ than ICON ($1.17\ W\ m^{-2}$) and ERA5 ($1.7\ W\ m^{-2}$). At mesoscales, $\Delta\mathcal{C}_{A\to D} \sim 0.73$–$0.77\ W\ m^{-2}$, which is similar for both models and the reanalysis. However, because more energy cascades from the large scales in ICON ($\Delta\Pi_K \simeq 0.11\ W\ m^{-2}$) compared to the IFS ($\Delta\Pi_K \simeq 0.06\ W\ m^{-2}$), the compensating dissipation of HKE is also stronger in ICON. The global energy imbalance, approximated by the cumulative effective generation of $\Delta(\mathcal{G}_A - D_A)$, is similar for ICON and the IFS ($\Delta(\mathcal{G}_A - D_A) \simeq 0.5\ W\ m^{-2}$) and about $0.4\ W\ m^{-2}$ for ERA5 at large scales. Because the effective generation in a stationary state is conservative, an equivalent dissipation must occur at mesoscales to compensate for the large-scale energy generated.

The general characteristics of the energy fluxes at large scales closely agree with previous studies (Augier and Lindborg, 2013; Li et al., 2023). However, previous analyses of resolved mesoscale fluxes had coarser resolutions than the ones investigated here, which is a drawback for simulating the mesoscale dynamics, especially for resolving gravity waves and strongly stratified turbulence (Augier and Lindborg, 2013), which motivated this study. As mentioned earlier, most differences among models are

found at mesoscales, particularly in the spectral transfer of HKE. This spectral energy transfer is consistently weaker in IFS compared to ICON. The reasons for the weak upscale and downscale cascades in the IFS are discussed in detail in Malardel and Wedi (2016), showing that a forward cascade could be simulated with the IFS if essential parts of the boundary layer parameterization are turned off, e.g., the momentum exchanges near the surface and in the boundary layer. For example, ICON simulates a peak downscale spectral transfer of $\tilde{\Pi}_K \approx 0.36\ W\ m^{-2}$ in contrast to the IFS, where $\tilde{\Pi}_K \approx 0.16\ W\ m^{-2}$, and the HKE spectrum is steeper than $l^{-5/3}$ (see Fig. 4.1c). In the case of ICON, the HKE spectrum closely follows the $l^{-5/3}$ power law; however, it is only partially explained by the downscale cascade since the cumulative conversion $\mathcal{C}_{A \to D}$ is not negligible at these scales and affects the magnitude of the DKE spectrum considerably. Note that $\mathcal{C}_{A \to D} > 0$ and decreases at the mesoscales, which means a local positive conversion, indicating that a fraction of the $l^{-5/3}$ spectrum must be produced by direct forcing of the HKE. Adding to the direct local forcing of DKE at mesoscales is the conversion between RKE and DKE, which is $\mathcal{C}_{D \to R} < 0$ at these scales and increases with wavenumber, indicating that RKE decreases in favor of DKE generation; however this conversion does not affect the total HKE spectrum. As expected, the RKE spectrum dominates the planetary and synoptic scales, following a slope close to $-3$. At mesoscales, the spectrum of rotational kinetic energy $E_R$ flattens, confirming the results of (Koshyk et al., 1999; Waite and Snyder, 2013). The vertically integrated $E_R$ and $E_D$ become comparable at mesoscales, contributing equally to the total HKE spectrum consistent with the prediction of strongly stratified turbulence (Lindborg, 2006). However, the magnitude of $E_A$ seems inconsistent with the strongly stratified turbulence scaling, which predicts $E_A \sim E_K$.

The differences in the cumulative conversion of APE to DKE can be understood from its definition: $\mathcal{C}_{A \to D}(l) = \sum_{n \geq l} \sum_{|m| \leq n} -(\omega, \alpha)_{nm}$, where $\alpha = R_d T/p$ is the specific volume. From Fig. 4.1, we note that ICON simulates a larger magnitude of APE, implying a larger temperature variance and VKE than IFS at mesoscales. These differences in VKE between the models are relevant in explaining the differences in strength of the coupling between horizontal and vertical motions, as measured by the local energy conversion from APE to HKE shown in Fig. 4.1. The compensated VKE spectrum ($\tilde{E}_w$) is obtained from the relationship based on mass continuity (3.12), introduced in section 3.4.2, which relates VKE and HKE spectra as $E_w(\kappa) = (h_e \kappa)^2 E_D(\kappa)$, where $h_e$ denotes the effective height. Combining (3.12) and (4.1), we define the compensated nondimensional spectrum of VKE as

$$\tilde{E}_w(l) = C(\Delta p/g)^{-1/3}(r\tilde{\Pi}_K)^{-2/3}(r/h_e)^2 l^{-1/3} E_w(l). \tag{4.2}$$

where $C = 1$, $r$ is Earth's radius, and $h_e \sim 1$ km measures the depth of layers with effectively uniform divergent flow (Schumann, 2019). The vertically integrated $E_D$ in ICON is slightly shallower than $l^{-5/3}$ (Fig. 4.1d) peaking around the model's effective resolution ($\lambda_h \sim 4$–$6\Delta x$), where $\Delta x$ is the horizontal grid resolution (Skamarock, 2004). An interesting outcome of the scaling presented in (4.2) is that the compensated VKE spectrum (4.2) closely follows that of APE at most scales rather than DKE. At scales ($\lambda_h \sim 100$ km), $\tilde{E}_w$ approaches the isotropic, incompressible scaling proposed by Schumann (2019), as discussed in section 3.4.2. In the IFS, $\tilde{E}_w$ shows an abrupt decrease close to the effective resolution, indicating that vertical motions are considerably

damped at small unresolved scales. In contrast, $\tilde{E}_w$ follows the divergent energy down to dissipation scales in ICON.

### 4.2.2 The vertical distribution of the energy fluxes

As discussed in section 4.2, the spectral energy fluxes vertically integrated up to the lower stratosphere indicate that the mesoscales are dominated by a downscale cascade of HKE and local energy conversion of APE into HKE. The contributions from energy transfers and conversion are model-dependent–the IFS spectrum is consistent with more prominent contributions from local energy sources/sinks, whereas scale interactions are the dominant process in ICON. This section investigates the vertical structure of the energy fluxes and discusses the energy transfers of the two models, including ERA5 as a comparison baseline. We focus on two pressure layers corresponding to approximately the free troposphere ($\sim$ 450–250 hPa) and the lower stratosphere ($\sim$ 250–50 hPa). Figure 4.2 shows the spectral fluxes and the cumulative conversion integrated for the ERA5 dataset. From Fig. 4.2a, it is evident that most of the features of the energy fluxes integrated within 1000–50 hPa discussed in section 4.2 (Fig. 4.1a, b) are mainly associated to the upper troposphere. The tropospheric $\mathcal{C}_{A\rightarrow D}$ and $\Pi_A$ in ERA5 resemble those of the IFS simulation, which is not surprising since the IFS is used as the dynamic core for the reanalysis and largely dictates the large-scale dynamics. Interestingly, ERA5 produces a robust HKE transfer across all scales in the troposphere, more similar to the ICON simulation, arguably due to the assimilation of horizontal winds from observations with higher variance than simulated by the IFS at mesoscales.

In the lower stratosphere (Fig. 4.2b), APE transfers upscale $\Pi_A < 0$ and $\Pi_A$ and increases with increasing wavenumber at scales ($3 \leqslant l \leqslant 20$). At the same time, there is a relatively large net conversion of DKE to APE ($\Delta\mathcal{C}_{A\rightarrow D} < 0$); however, it is too small to balance the loss of APE through upscale transfer resulting in $\Delta(\mathcal{G}_A - D) \simeq -0.25\ W\ m^{-2}$. The net vertical flux predominantly enhances DKE at these scales, suggesting that a substantial dissipation of APE must be responsible for the imbalance. At mesoscales ($l > 20$), the transfer of APE remains upscale, and the loss of APE is further amplified by a positive conversion of APE to DKE ($\mathcal{C}_{A\rightarrow D} > 0$), resulting in a net effective generation of $\Delta(\mathcal{G}_A - D_A) \simeq 0.06\ W\ m^{-2}$. This net imbalance at mesoscales could potentially be linked to the APE generation due to latent heat release from deep convection, as other diabatic sources are not expected to contribute to the lower stratosphere.

Figure 4.2 also shows the total cumulative (inward) vertical fluxes, defined as $\Delta_{p_t}^{p_b}\mathcal{F}_{\uparrow} = \mathcal{F}_{\uparrow}(p_b) - \mathcal{F}_{\uparrow}(p_t)$, where $\mathcal{F}_{\uparrow} = \mathcal{F}_{A\uparrow} + \mathcal{F}_{D\uparrow}$ is the sum of APE and DKE cumulative vertical fluxes evaluated at the bottom ($p_b$) and top ($p_t$) of the layer respectively. The overall characteristics of the vertical fluxes are in close agreement with the results of Li et al. (2023) (their Fig. 5), who analyzed one month of 6-hourly ERA5 data corresponding to January 2018. In the upper troposphere (Fig. 4.2a), the cumulative vertical flux increases from $-0.6\ W\ m^{-2}$ at planetary scales to around zero at $l = 200$, indicating the removal of DKE and APE at these scales. Nevertheless, the budget of HKE at these scales is still dominated mainly by conversion from APE.
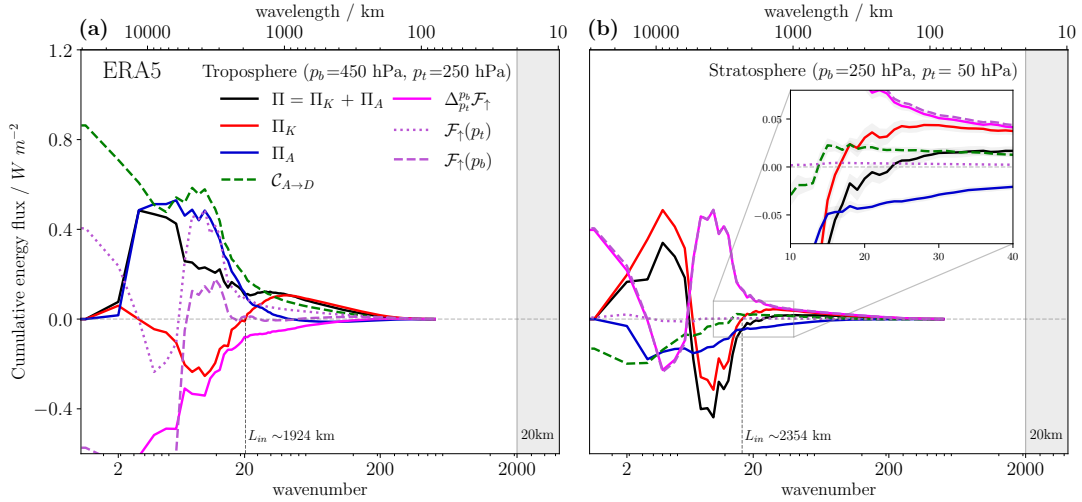
**Figure 4.2:** Cumulative nonlinear transfers of HKE and APE, energy conversion from APE to HKE, and total vertical fluxes as a function of spherical wavenumber for ERA5, vertically integrated over layers corresponding to (a) the upper troposphere and (b) the lower stratosphere. The inset in (b) is an expanded view of wavenumbers approximately corresponding to synoptic-to-mesoscale transition $(10 \leqslant l \leqslant 40)$. The gray shaded area corresponds to scales $\lambda_h < 20$ km.

At mesoscales, the vertical fluxes are relatively small within the layer, indicating that the spectral transfer dominates. To better understand how the net cumulative fluxes influence the energy budget in each layer, we carefully examine the vertical fluxes through the bottom and top surfaces in Fig. 4.2. In the upper troposphere, $\mathcal{F}_\uparrow$ is upward at $p_b = 450$ hPa (Fig. 4.2a) decreasing at wavenumbers $1 \leqslant l \leqslant 3$, and then increasing at wavenumbers $3 \leqslant l \leqslant 10$; since $\mathcal{F}_\uparrow(p_t) > \mathcal{F}_\uparrow(p_b)$ at these scales, the net effect is an energy loss to the lower stratosphere. This large-scale energy exchange between the troposphere and lower stratosphere is likely associated with the conversion due to the Hadley and Ferrel cells, as discussed by Augier and Lindborg (2013). At mesoscales $(l > 40)$, the exchange of energy between the two layers is minor compared to planetary and synoptic scales; nevertheless, the vertical flux at 250 hPa is upward while it is nearly zero at 450 hPa, indicating a net energy loss due to gravity waves generated in the troposphere that propagate into the lower stratosphere. These waves generated in the troposphere greatly impact the lower stratospheric mesoscale spectrum of HKE because the net vertical flux (as shown in Fig. 4.2b) is comparable to the nonlinear HKE transfer towards small scales, and it contributes more than the local conversion from APE. However, the limited horizontal resolution of ERA5 restricts a comprehensive assessment of mesoscale fluxes. Considering this limitation, our focus now shifts toward the resolved fluxes of the high-resolution simulations and their implications.

Figure 4.3 shows the energy budget from the high-resolution simulations performed with ICON and the IFS. In the upper troposphere (Fig. 4.3a,c), the characteristics of the IFS's cumulative conversion and spectral transfer of APE are similar to those discussed before for ERA5 except for the HKE spectral transfer. In contrast, ICON simulates a weaker cumulative conversion of APE to DKE and the APE spectral transfer across scales in this layer but with a spectral transfer of HKE with a magnitude similar to ERA5. The cumulative vertical fluxes from the simulations present a peculiar
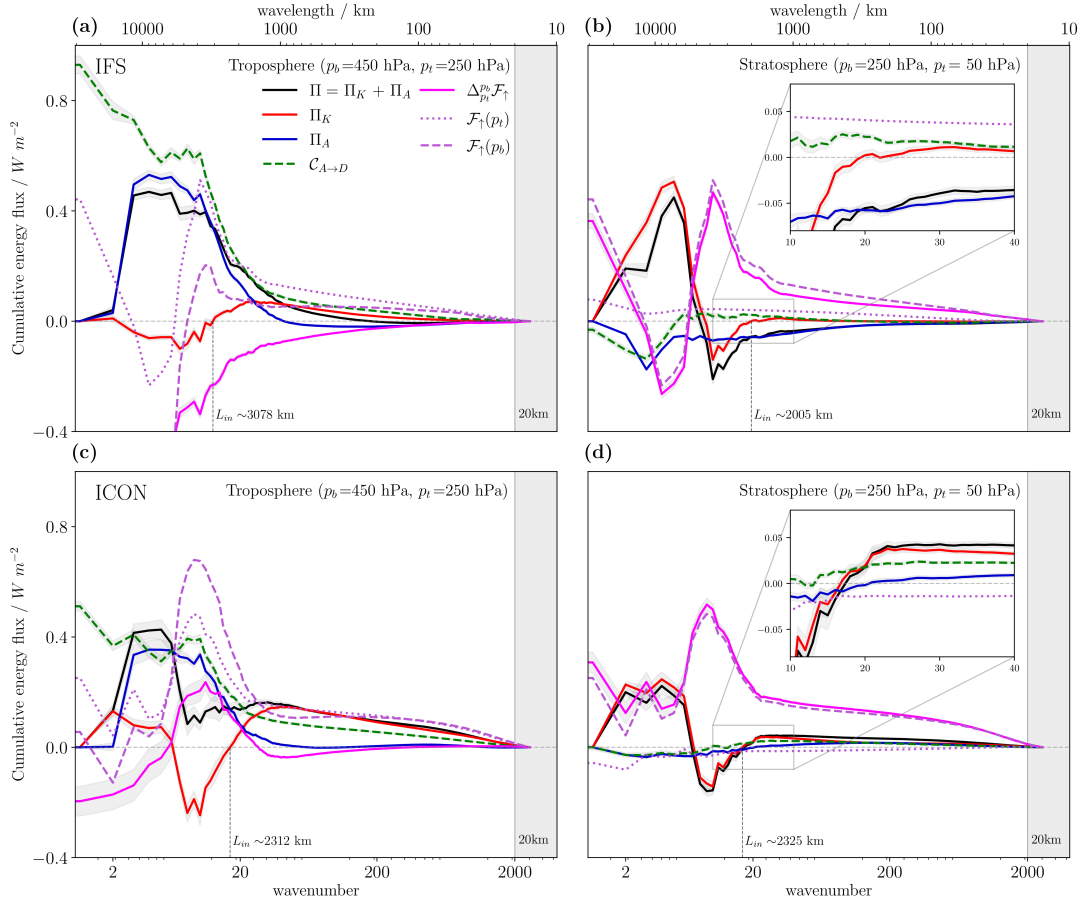
**Figure 4.3:** Cumulative nonlinear transfers of HKE and APE, energy conversion from APE to HKE, and total vertical fluxes as a function of spherical wavenumber for (a),(b) the IFS, and (c),(d) ICON vertically integrated over layers corresponding to (a),(c) the free troposphere and (b),(d) the lower stratosphere. The insets in (b) and (d) are an expanded view of wavenumbers approximately corresponding to synoptic-to-mesoscale transition ($10 \leqslant l \leqslant 40$). The gray shaded area corresponds to scales smaller than the triangular truncation ($\lambda_h < 20$ km).

shape at large and synoptic scales peaking around $l \sim 10$ for ICON and $l \sim 6$ for the IFS. These intense net vertical fluxes at large scales are not present in ERA5 (Fig. 4.2a) but closely agree with fluxes reported by Augier and Lindborg (2013) simulated with the AFES model. These maxima in $\Delta\mathcal{F}_\uparrow$ nearly coincide with the peak upscale HKE transfer for each model. The vertical fluxes at the top and bottom layers decrease with wavenumber, and $\Delta\mathcal{F}_\uparrow(p_b)$ dominates so that the layer gains energy from upward-propagating large-scale waves. Most energy fluxes of the IFS in the lower stratosphere (Fig. 4.3b,d) compare favorably with ERA5 at large scales, especially the APE transfer and the compensating conversion from DKE to APE ($\mathcal{C}_{A\to D} < 0$) that sustains the upscale APE transfer ($\Pi_A < 0$). In contrast, ICON presents a weaker downscale HKE transfer and consequently a smaller magnitude of the conversion ($\mathcal{C}_{A\to D}$) and upscale APE transfer. These results are consistent with those reported by Augier and Lindborg (2013) from simulations of the AFES and IFS models, concluding that the lower stratosphere is not directly forced by baroclinic instability at large scales but by vertical fluxes from the troposphere, owing to upward-propagating planetary waves.

The simulations investigated here provide a notable advantage over the ERA5 dataset in resolving a wider range of scales. For this reason, we focus on the mesoscale energy fluxes in the following. In the troposphere $\Delta\mathcal{F}_\uparrow$ slightly increases in the wavenumber range $40 \leqslant l \leqslant 200$ for both models, with $\mathcal{F}_\uparrow(p_b)$ and $\mathcal{F}_\uparrow(p_t)$ decreasing with wavenumber, since $\mathcal{F}_\uparrow(p_t) > \mathcal{F}_\uparrow(p_b)$ the upper troposphere loses energy through an upward flux at $p_t = 250$ hPa at these scales, indicating gravity wave generation within the layer. In ICON, $\mathcal{F}_\uparrow(p_t)$ and $\mathcal{F}_\uparrow(p_b)$ have similar magnitudes for wavenumbers $> 200$, so that the upper tropospheric HKE remains unaffected at these scales. In the IFS, the vertical fluxes through the top and bottom layers are upward with similar magnitudes at shorter scales ($l \geq 512$). This result suggests that upward propagating gravity waves with wavelengths $200 \lesssim \lambda_h \lesssim 1000$ km are mainly generated in the upper troposphere. In contrast, gravity waves with $\lambda_h \lesssim 200$ km are generated in the lower troposphere and propagate freely through the upper troposphere, directly forcing the lower stratospheric HKE spectrum at mesoscales. The cumulative vertical fluxes in the lower stratosphere (Fig. 4.3b,d) reveal that vertically propagating IGWs are more dominant at mesoscales than spectral transfers– the models exhibit a negligible HKE cascade and only a small direct forcing due to conversion from APE to HKE. In both models, there is an upward vertical flux through the tropopause at mesoscales since $\mathcal{F}_\uparrow(p_b) > 0$ and decreases with wavenumber, while $\mathcal{F}_\uparrow(p_t) \sim 0$, indicating that upward-propagating IGWs generated in the troposphere are the primary mechanism forcing the lower stratospheric HKE spectrum.

The previous analysis presented the main differences between the models regarding energy fluxes and spectral transfers. The question is, how are these differences reflected in the resulting mesoscale energy spectrum? Figure 4.4, shows compensated nondimensional spectra of horizontal ($\tilde{E}_K$), rotational ($\tilde{E}_R$), divergent ($\tilde{E}_D$), and vertical ($\tilde{E}_w$) kinetic energies, as well as available potential energy ($\tilde{E}_A$) for the simulations. In addition, we include the HKE spectra calculated from horizontal winds obtained from IGWs modes, as explained in section 2.3. Let us focus on the upper troposphere in Fig. 4.4, panels (a) and (b). At large scales, the models have similar magnitudes of HKE (solid black line), decreasing with wavenumber as $l^{-3}$. At about 200 km, the HKE spectrum transitions to a shallower spectrum closely following a $l^{-5/3}$ (horizontal reference line) in ICON and slightly steeper in the IFS. The Helmholtz decomposition of the HKE spectrum reveals that the DKE and RKE contribute equally to the mesoscale kinetic energy at 40 km for the IFS and 65 km in ICON. A notable difference is that both $E_R$ and $E_D$ approximately follow a $l^{-5/3}$ in ICON toward small scales, while $E_R$ follows the $l^{-3}$ at all scales for the IFS, and $E_D$ is steeper than $l^{-5/3}$.

The VKE spectrum (black dashed-dotted line in Fig. 4.4) has a similar shape at large scales for both models; however, it approaches the incompressible scaling at scales $\sim 400$ km in the IFS, while this scaling is obtained at shorter scales of about 100 km in ICON with a larger VKE magnitude than the IFS at mesoscales. These results suggest that horizontal and vertical motions are dynamically coupled in ICON, where the VKE magnitude, larger than predicted by incompressible mass continuity, favors a direct conversion of APE to DKE, resulting in enhanced DKE at small scales. In contrast, the IFS is consistent with a kinematic relation between VKE and DKE at mesoscales suggested by Schumann (2019), and the corresponding direct forcing of DKE due to net cumulative conversion ($\Delta\mathcal{C}_{A\to D} \simeq 0.02\ W\ m^{-2}$) is smaller than
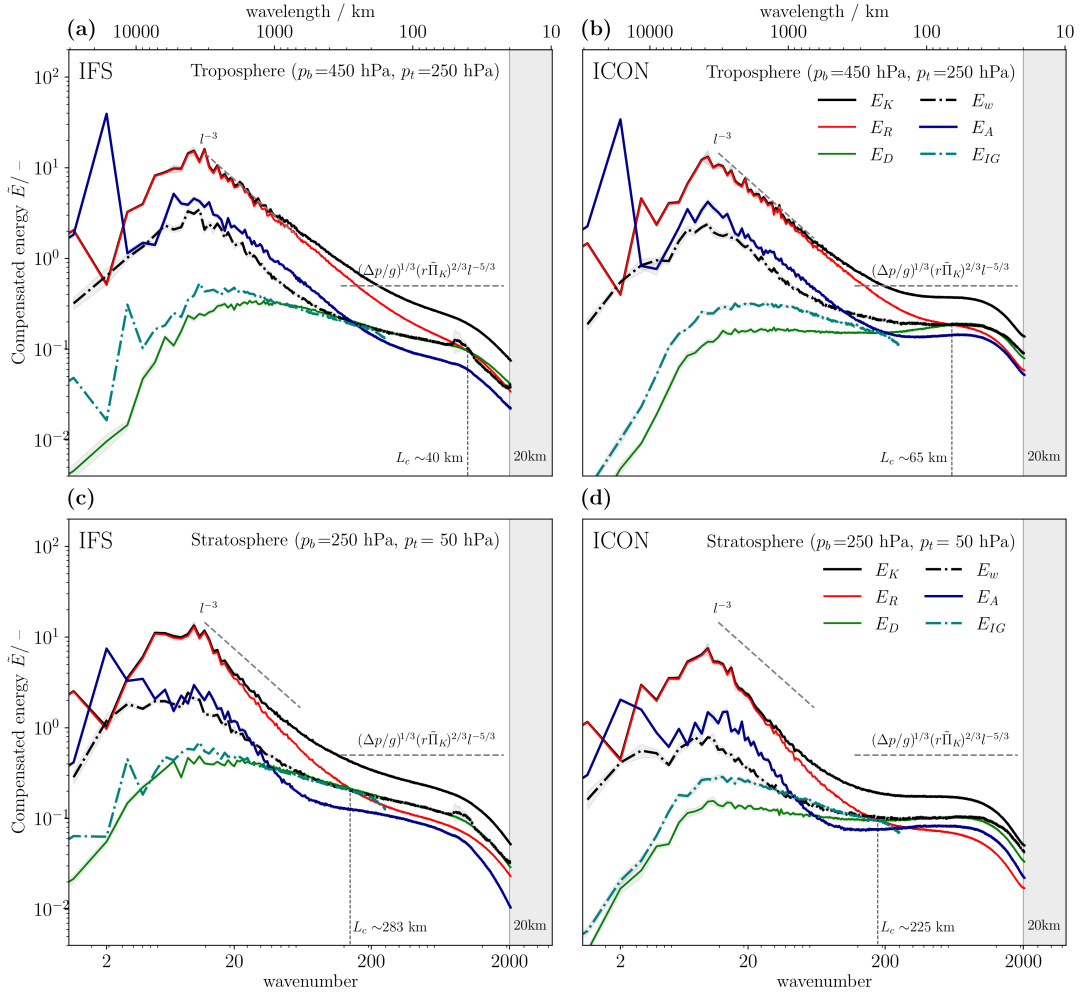
**Figure 4.4:** Compensated nondimensional spectra of HKE (solid black), APE (solid blue), RKE (solid red), DKE (solid green), VKE (dashed-dotted black) and HKE calculated from IGWs modes (dashed green) as a function of spherical wavenumber and vertically integrated over layers corresponding to (a),(b) the free troposphere and (c),(d) the lower stratosphere for (a),(c) the IFS, and (b),(d) ICON. The legend is given in panels (b) and (d). The grey shaded area corresponds to scales smaller than the triangular truncation ($\lambda_h < 20$ km).

in ICON ($\Delta\mathcal{C}_{A \to D} \simeq 0.06 \ W \ m^{-2}$), as shown in Fig. 4.3. Moreover, the slope of the compensated VKE spectrum is closer to the $\tilde{E}_{IG}$ (dashed green line) than to $\tilde{E}_D$, which supports our conclusion that vertical motions are controlled by horizontal IGWs modes at mesoscales (see section 3.4.2). In the lower stratosphere (Fig. 4.4c,d), the HKE spectrum approaches the $l^{-5/3}$ power law at larger horizontal scales compared to the troposphere– the crossing scale $L_c$, defined as the scale where $\tilde{E}_D$ and $\tilde{E}_R$ intersect, is 283 km for the IFS and 225 km for ICON. The divergent component, mostly associated with IGWs since $\tilde{E}_D \sim \tilde{E}_{IG}$, dominates the mesoscale kinetic energy in both models. As discussed earlier, the downscale HKE cascade is small compared to vertical fluxes due to IGWs, meaning that direct local forcing of DKE is more relevant than spectral transfers in determining the $l^{-5/3}$ mesoscale spectrum at these altitudes.

From linear gravity wave theory, $E_A \sim E_{IG}/2$ would be about consistent with a spectrum dominated by IGWs of intrinsic frequencies $\hat{\omega} \sim 2|f|$, which stems from the

fact that $E_A$ and $E_{IG}$ are related through the hydrostatic polarization and dispersion relation as $E_{IG}/E_A = [1 + (f/\hat{\omega})^2]/[1 - (f/\hat{\omega})^2]$ in the frequency range $f \leqslant \hat{\omega} \ll N$, where $E_{IG}$ is approximated by $E_D$ at scales $l > 512$ because of the truncation used in the modal decomposition. Hydrostatic IGWs require $E_w < E_A < E_{IG}$ because otherwise, the intrinsic frequency is outside the range $f \leq \hat{\omega} \leq N$. Similarly, the APE and VKE spectra are linked as $E_w/E_A = (\hat{\omega}/N)^2$ (Geller and Gong, 2010). Calculating this ratio from the spectra shown in Figs. 4.4c,d gives $\hat{\omega} \sim 3|f|$ for the IFS, and $\hat{\omega} \sim 2|f|$ for ICON at mesoscales. The values $\hat{\omega} \sim 2\text{–}3|f|$ are in close agreement with the intrinsic frequencies estimated in section 3.4.1 based on ratios of divergent to rotational kinetic energies of the wave field using (3.4). At large scales, the ratio $E_w/E_A$ can not be explained by IGWs since the shape of $E_A$ associated with the wave field should approximately follow a $l^{-5/3}$ power law at all scales, whereas the balanced flow dictates the $l^{-3}$ APE spectrum (Tanaka, 1985; Žagar et al., 2015). The fact that $\tilde{E}_w$ follows $\tilde{E}_A$ at synoptic scales seems to indicate that large-scale vertical motions are related to the balanced circulation and not freely propagating IGWs as hypothesized in section 3.4.1, from QG scaling arguments.

## 4.3 CONTRIBUTIONS OF BALANCED AND UNBALANCED DYNAMICS

As discussed in section 4.2.2, the direct forcing of IGWs on the mesoscale energy spectra in the upper troposphere is limited, and the dominant impact comes from the HKE spectral transfer according to both models. These findings align with Augier and Lindborg (2013), who suggested that the tropospheric mesoscale $l^{-5/3}$ spectra conform to predictions based on the presence of a cascade mediated by nonlinear interactions. Section 4.3.1 addresses this issue by performing a Helmholtz decomposition of the HKE budget as demonstrated by Li et al. (2023).

### 4.3.1 Spectral rotational and divergent kinetic energy transfers

As shown in Fig. 4.4, the divergent and rotational kinetic energies approach the same spectral magnitude and slope in the tropospheric mesoscales, meaning these components contribute equally to the HKE spectrum. However, it is not only the relative magnitude of the rotational and divergent components that are important for the dynamics behind the energy spectrum but also the multiscale nonlinear interactions between these two components (Li et al., 2023). Moving forward, we discuss these interactions based on the spectral transfers of the IFS and ICON simulations.

Figure 4.5 shows the cumulative nonlinear spectral transfer of horizontal ($\Pi_K$), rotational ($\Pi_R$), and divergent ($\Pi_D$) kinetic energies integrated over the upper troposphere (250–450 hPa). The interactions between $E_R$ and $E_D$ are shown by the cumulative conversion ($\mathcal{C}_{D\rightarrow R}$) for (a) the IFS and (b) ICON. The cumulative conversion is further split into the contributions from the Coriolis effect ($\mathcal{C}_{D\rightarrow R}^f$), vertical vorticity ($\mathcal{C}_{D\rightarrow R}^\zeta$), and vertical velocity ($\mathcal{C}_{D\rightarrow R}^\omega$). The total conversion between DKE and RKE equals the sum of each component mentioned above. For details on the exact formulas for each energy conversion term, see section 2.5.1. Despite the

apparent differences in the magnitudes of the spectral energy transfer between the IFS and ICON, their spectral shapes and relative contributions from rotational and divergent transfer are similar. The models show that interactions between rotational modes ($\Pi_R$) mediate the upscale cascade at synoptic and planetary scales starting at approximately 2000 km. The upscale cascade is accompanied by a large net cumulative conversion in both models since $\mathcal{C}_{D \to R}^f$ has a steep decrease with wavenumber. From the budget of rotational kinetic energy (2.28), the only sources of RKE at a given range of scales are the conversion from DKE and spectral transfer $\Pi_R$, balanced by dissipation $\mathcal{D}_R$. Since both models show similar amounts of net conversion $\mathcal{C}_{D \to R}$, and the RKE transfer is smaller in IFS, the dissipation of RKE must be stronger compared to ICON.
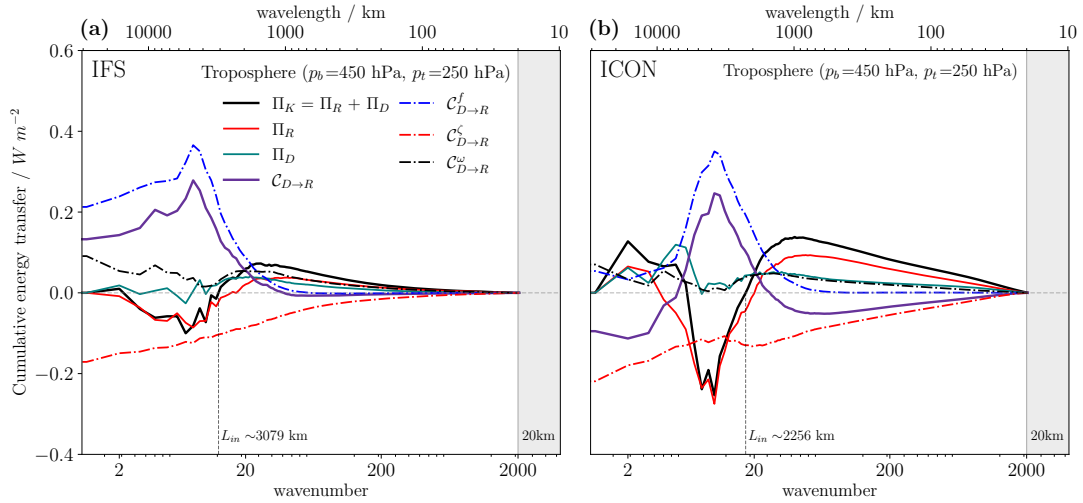


**Figure 4.5:** Cumulative nonlinear transfers of horizontal ($\Pi_K$), rotational ($\Pi_R$), and divergent ($\Pi_D$) kinetic energies. The cumulative conversion from DKE to RKE is decomposed into the contributions from the Coriolis effect ($\mathcal{C}_{D \to R}^f$), vertical vorticity ($\mathcal{C}_{D \to R}^\zeta$), and vertical velocity ($\mathcal{C}_{D \to R}^\omega$) for (a) the IFS and (b) ICON vertically integrated over the upper troposphere (250–450 hPa). The grey shaded area corresponds to scales smaller than the triangular truncation ($\lambda_h < 20$ km).

At mesoscales (Fig. 4.5), $\Pi_R$ and $\Pi_D$ are downscale, however $\Pi_R$ dominates the HKE spectral transfer in both models. The DKE spectral transfer (green line) is similar in both models, indicating that stronger nonlinear interactions between rotational modes explain ICON's larger mesoscale energy cascade than the IFS. At scales of $\lesssim 650$ km, the linear cumulative conversion approaches zero. The net conversion between RKE and DKE is determined by the balance between $\mathcal{C}_{D \to R}^\zeta$ and $\mathcal{C}_{D \to R}^\omega$. In both simulations, $\mathcal{C}_{D \to R}^\omega$ have similar magnitudes and decrease with wavenumber, which means it converts DKE to RKE. The dominant contribution to the net conversion comes from $\mathcal{C}_{D \to R}^\zeta$, which increases with wavenumber, i.e., it converts RKE to DKE. These two terms nearly balance out in the IFS, meaning that rotational and divergent energies are effectively decoupled. In contrast, ICON shows a strong conversion from RKE to DKE. This mechanism seems to explain why the DKE spectrum is flatter than $l^{-5/3}$ and has a larger magnitude than RKE at mesoscales (Fig. 4.4b)– that is, RKE cascades downscale in large quantities towards dissipation scales. At the same time, a considerable fraction of it is converted to DKE through nonlinear interactions.

### 4.3.2 Spectral kinetic energy transfer of Rossby and inertia-gravity waves

The decomposition of the spectral energy budget into rotational and divergent components provides insights into the underlying dynamics of the energy spectrum; however, it is important to consider its limitations in discerning between different physical processes, such as waves or stratified turbulence (Lindborg, 2006). Although the downscale cascade is a strongly nonlinear process, linear IGWs can interact with the mean flow and contribute to the spectral transfer across scales (Lelong and Riley, 1991; Waite and Bartello, 2006; Kitamura and Matsuda, 2010; Kafiabad et al., 2019). However, the role of IGWs in the downscale energy cascade is not fully understood. In the following, we estimate the contributions of linear Rossby and IGW modes to the spectral HKE transfer. First, the spectral energy budget described in section 2.5 is computed for the inverse fields resulting from the normal mode decomposition described in section 2.3. The inverse fields of the decomposition consist of the horizontal wind components, temperature, and the geopotential associated with the balanced Rossby and unbalanced IGW modes. The vertical velocity of each component is calculated as described in 2.4. The spectral budget is also calculated on the total fields, i.e., the numerical outputs from the models used as input for the normal mode decomposition.

The approach described above provides a dynamically consistent estimation of the spectral energy budget for each component: Rossby waves, IGWs, and the total atmospheric circulation separately. However, in contrast to the Helmholtz decomposition of the budget, which exactly separates the fluxes into rotational and divergent components, the spectral energy fluxes of each mode do not add up to the total fluxes. This mismatch happens for two reasons: First, the thermodynamic state of each component must be consistent with the wind field, which differs among the components. Secondly, the spectral transfer and fluxes involving interactions between the Rossby and IGW modes are not considered in each separate calculation of the budget. For example, we can estimate these interactions by defining a complementary cumulative spectral transfer ($\Pi_{CF}$) that satisfies

$$\Pi_K = \Pi_{RO} + \Pi_{IG} + \Pi_{CF} \tag{4.3}$$

where each $\Pi$ term is calculated using (2.29), $\Pi_K$ is the total nonlinear HKE spectra transfer, $\Pi_{RO}$ and $\Pi_{IG}$ are the nonlinear spectral HKE transfer of Rossby and IGW modes, respectively. The other fluxes entering the budget equations are calculated similarly. When the velocity field is decomposed into vortical/geostrophic (V) and gravity-wave (W) modes, the energy transfer function $\Pi_K$ can be interpreted as triad interactions (Kitamura and Matsuda, 2010). These interactions can be categorized into four types: VVV (composed of three vortical modes), VVW (two vortical modes and one wave mode), VWW (one vortical and two wave modes), and WWW (three wave modes). The kinetic energy transfer function can be expressed as $\Pi_K = \Pi_{VVV} + \Pi_{VWW} + \Pi_{VVW} + \Pi_{WWW}$. From (4.3), it follows that $\Pi_{RO} = \Pi_{VVV}$, $\Pi_{IG} = \Pi_{WWW}$, and $\Pi_{CF} = \Pi_{VWW} + \Pi_{VVW}$. Note that the exact spectral transfer due to nonlinear interactions between Rossby and IGW modes could, in principle, be derived from the primitive system of equations (2.11) and (2.12), as demonstrated in previous studies,

e.g. Marques and Castanheira (2012); however, this is outside the scope of the current analysis.

Figure 4.6 shows the cumulative energy transfers of HKE, decomposed into the RKE and DKE components as in Fig. 4.5 for ERA5, vertically integrated over (a) the upper troposphere and (b) the lower stratosphere. The cumulative (inward) vertical flux ($\Delta\mathcal{F}_{IG\uparrow}$) due to vertically propagating IGWs is shown in magenta. Additionally, we include the spectral energy transfers associated with Rossby waves ($\Pi_{RO}$), IGWs ($\Pi_{IG}$), and their interactions ($\Pi_{CF}$). In the following, we only show results from the ERA5. The NMF decomposition truncates the numerical outputs at wavenumber $l = 320$, which resolves horizontal wavelengths ($\lambda_h \sim 125$ km) for ERA5, the IFS, and ICON, meaning that no additional value is gained from the high-resolution simulations, and they compare favorably with ERA5 (not shown).
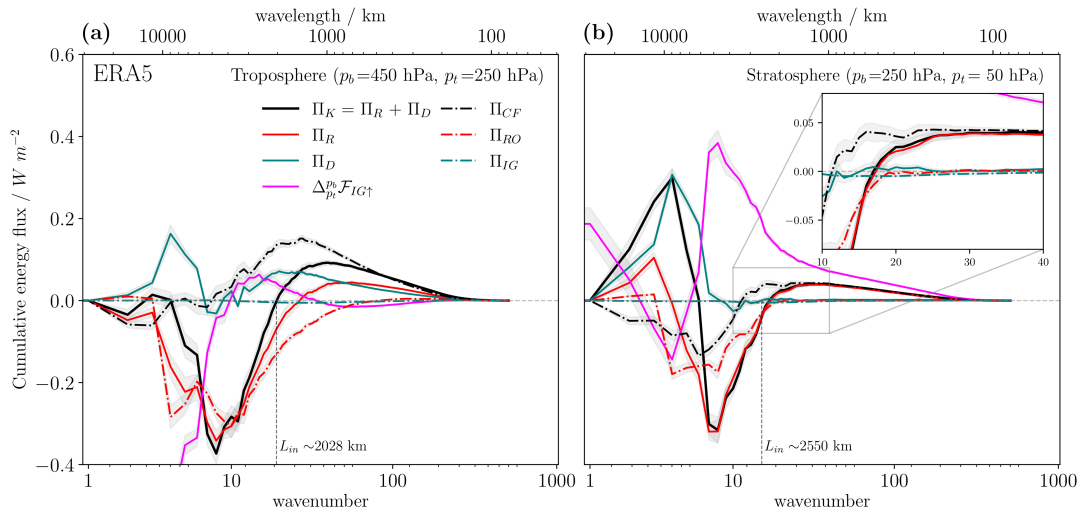


**Figure 4.6:** Cumulative energy transfers of HKE (solid black) decomposed into the RKE (solid red) and DKE (solid green) components for ERA5, vertically integrated over (a) the upper troposphere and (b) the lower stratosphere. The cumulative (inward) vertical flux ($\Delta_{p_t}^{p_b}\mathcal{F}_{IG\uparrow}$) due to vertically propagating IGWs is shown in magenta. The energy transfers $\Pi_{RO}$ and $\Pi_{IG}$ correspond to Rossby waves (dashed red) and IGWs (dashed green), respectively. The complementary energy transfer ($\Pi_{CF}$) calculated using (4.3), and quantifying Rossby waves and IGW interactions is shown in dashed black. Vertical dotted lines denote the energy injection scale ($L_{in}$). The legend is given in panel (a). The grey shading around each line indicates the temporal standard deviation.

Let us focus on the cumulative vertical flux of IGW energy (magenta line in Fig. 4.6). In contrast to the vertical fluxes shown in previous sections, $\Delta\mathcal{F}_{IG\uparrow}$ is the sum of the vertical pressure and momentum fluxes corresponding to the IGW inverse fields. At planetary scales, $\Delta\mathcal{F}_{IG\uparrow} < 0$ and increases with wavenumber towards synoptic scales, indicating a loss of DKE due to vertically propagating planetary waves. At scales $10 \leqslant l \leqslant 20$, the upper troposphere gains energy from large-scale IGWs propagating from the lower troposphere. The cumulative vertical flux is relatively small at mesoscales ($l \gtrsim 40$) and increases with wavenumber, suggesting that the layer loses energy due to IGWs propagating to the lower stratosphere. The signature of these waves can be seen in Fig. 4.6b, where all scales $l \gtrsim 10$ gain energy from upward

propagating IGWs and contribute more to the HKE spectrum than the spectral transfers $\Pi_K$; however this spectral transfer is not negligible.

The cumulative spectral transfers of RKE, DKE, and HKE in the upper troposphere (Fig. 4.6a) exhibit similar behavior as the high-resolution simulations (Fig. 4.5); however, $\Pi_R$ and $\Pi_D$ contribute equally to the total transfer at mesoscales. Perhaps not surprisingly, the nonlinear transfer due to Rossby waves closely approximates the upscale transfer due to interactions between rotational modes $\Pi_{RO} \sim \Pi_R$ at scales $l < 10$, which is expected because Rossby waves are governed by QG dynamics represented by the triad VVV. At scales $\lesssim 300$ km, $\Pi_{RO}$ deviates from $\Pi_R$ and approaches zero towards the truncation scale. This difference between $\Pi_{RO}$ and $\Pi_R$ at mesoscales suggests that the more energetic rotational modes that cause the downscale cascade are not contained in the linear Rossby modes. Another type of balance might be important at these scales, e.g., stratified turbulence (Lindborg, 2006). Notably, the nonlinear transfer of wave energy $\Pi_{IG}$ is negligible at all scales even when $\Pi_D$ explains about half the total HKE transfer, which seems to reject the hypothesis that the downscale cascade is due to weakly nonlinear interacting IGWs (Dewan, 1979; Smith et al., 1987).

The complementary energy transfer $\Pi_{CF}$ is small at large scales in the upper troposphere (Fig. 4.6a) and increases, reaching a maximum at around the energy injection scale $L_{in} \sim 2000$ km, meaning that the synoptic scales lose energy due to a downscale cascade mediated by interactions between the balanced flow and IGWs. This interpretation is further supported by the fact that $\Pi_R$ (interactions of purely rotational modes) is small, and both $\Pi_D$ and upward vertical IGW flux peak at these scales. However, the exact formulation of the interactions of IGWs and the balanced circulation is needed to say for sure. At mesoscales, $\Pi_{CF}$ approaches the total HKE downscale transfer $\Pi_K$ since both $\Pi_{RO}$ and $\Pi_{IG}$ are negligible, which suggests that interactions between IGWs and the balanced part of the flow could explain the nonlinear downscale energy cascade at mesoscales, where rotational and divergent modes have similar importance. This result is consistent with the finding of Kitamura and Matsuda (2010), who conducted idealized numerical experiments of rotating stratified turbulence. They identified that nonlinear interactions between vortical/geostrophic and gravity modes dominate downscale energy transfer.

In the lower stratosphere (Fig. 4.6b), the downscale energy transfer is smaller than in the upper troposphere, and $\Delta\mathcal{F}_{IG\uparrow}$ dominates, particularly at mesoscales. At large scales, $\Pi_R$ is not explained by $\Pi_{RO}$ as in the troposphere; rather, $\Pi_{RO}$ and $\Pi_{CF}$ contribute similarly to the upscale energy transfer. At mesoscales, the nonlinear interactions between rotational modes contribute the largest total transfer since $\Pi_R \sim \Pi_K$ and $\Pi_D \sim 0$ at scales $\lambda_h \lesssim 2500$ km. Moreover, $\Pi_{CF}$ is almost identical to the total downscale spectral transfer of HKE (see inset in Fig. 4.6b). A possible interpretation is that this spectral transfer results from resonant interactions between vortical and gravity-wave modes involving their rotational components. Waite and Bartello (2006) showed that in the case of strong stratification, vortical energy could dramatically affect the wave energy spectrum, which dominates at these scales.

## 4.4 SUMMARY AND CONCLUSIONS

This chapter investigates atmospheric energy spectra and the spectral energy budget of global storm-resolving simulations of various state-of-the-art GCMs of the DYAMOND experiment. The simulations analyzed here have considerably higher resolution than previous analyses of the atmospheric energy budget, providing an opportunity to investigate the dominant mechanism shaping the mesoscale spectrum. The analysis shows that the large-scale dynamics are consistent among the simulations and compare favorably with ERA and the results of Li et al. (2023).

The comparison of the cumulative energy transfers and vertical fluxes between the models within the upper troposphere and the lower stratosphere reveals that these two layers exhibit different dynamics at mesoscales. However, the models disagree on some important aspects: First, ICON successfully simulates the observed mesoscale $l^{-5/3}$ spectrum, while the IFS spectrum is between $l^{-5/3}$ to $l^{-3}$ at mesoscales. This characteristic of the IFS energy spectrum has been discussed in detail by Malardel and Wedi (2016), who showed that the steeper slopes are due to the impact of physical parametrizations on the resolved energy transfers. In particular, they showed that IFS can simulate a strong downscale energy cascade if the vertical diffusion scheme is turned off in the boundary layer and at the surface. In the case of ICON, vertical diffusion is parameterized with a prognostic turbulent kinetic energy (TKE) scheme. In contrast, the IFS uses a diagnostic eddy diffusivity scheme, which could explain the differences in the intensity of the mesoscale spectral transfer in the troposphere. The second main difference occurs in the lower stratosphere. The models simulate similar magnitudes of the downscale cascade with $\tilde{\Pi}_K \simeq 0.02 \ W \ m^{-2}$ and still display differences in HKE spectral slopes. The dominant contribution in this layer comes from the cumulative vertical fluxes, as shown in Fig. 4.3. Both models clearly show that the lower stratosphere is mainly energized by direct forcing due to upward propagating IGWs.

The direct forcing from IGWs in the upper troposphere is limited, and spectral transfers dominate the tropospheric HKE spectrum. The decomposition of the spectral energy budget into rotational and divergent components shows that nonlinear interactions involving rotational modes dominate the spectral energy transfer. Moreover, the normal mode decomposition of the atmospheric circulation into linear Rossby waves and IGWs of ERA5 and both simulations suggest that interactions between IGWs and the balanced flow explain the downscale energy cascade at mesoscales based on the fact that the complementary fluxes closely match the downscale HKE transfer at mesoscales. This result aligns with the hypotheses that explain the downscale cascade based on triad interactions between vortical and gravity wave modes (Lelong and Riley, 1991; Waite and Bartello, 2006; Kitamura and Matsuda, 2010; Kafiabad et al., 2019). The dominant interactions mediating the downscale cascade correspond to the WVV and VWW triads, which represent nonlinear interactions between vortical/geostrophic and gravity modes, in agreement with the idealized simulations of rotating stratified turbulence (Waite and Bartello, 2006; Kitamura and Matsuda, 2010). This result has not been reproduced before in realistic global high-resolution simulations of the atmosphere. However, our analysis does not allow for describing the exact nature of these interactions, and elucidating the dominant mechanism requires further investigation.

The spectral energy budget calculated from Rossby and IGW modes shows that the upscale HKE transfer at large scales is mainly associated with the balanced flow in the troposphere. In contrast, interactions between Rossby and IGWs are important in the lower stratosphere– the complementary transfer accounts for half the total upscale HKE transfer. The spectral HKE transfer calculated from IGW modes is negligible at all scales, which suggests that interacting wave modes do not contribute to the downscale energy transfer, challenging the hypothesis that the downscale cascade is due to weakly nonlinear interacting IGWs (Dewan, 1979; Smith et al., 1987). Whether or not wave-wave interactions shape the IGW spectrum in the atmosphere, our results suggest that these interactions are not necessary to explain the $\kappa^{-5/3}$ mesoscale spectrum in the simulations.

# 5 | CONCLUSION AND OUTLOOK

## 5.1 ANSWERING THE RESEARCH QUESTIONS

In this chapter, we proceed to answer the research questions posed in section 1.4 based on the results presented in chapters 3 and 4.

1. **What is the role of IGWs in the dynamic coupling of horizontal and vertical velocity wavenumber spectra?**

   The vertical kinetic energy spectrum investigated in global storm-resolving simulations is relatively flat across all resolved horizontal scales, with evidence of two peaks, one at synoptic scales ($\sim 2000$ km) and one at the smallest resolved scale ($\sim 20$ km). The results from partitioning the global circulation into linear IGW and balanced modes suggest that vertical motions are primarily attributed to the IGW field at most scales. Regardless of the model discrepancies in the underlying dynamics of horizontal winds, vertical motions seem consistent with quasi-linear dynamics. We presented semi-empirical models linking horizontal and vertical motion spectra based on hydrostatic IGW polarization relations, where the intrinsic frequencies are inferred from the linearized vorticity equation by quantifying the divergent to rotational kinetic energy ratio from the IGW modes. These simple models provide a quantitative prediction of the spectral slopes of vertical kinetic energy at large scales and mesoscales.

   The relationship between vertical and divergent kinetic energy spectra is best explained by mass continuity in the incompressible limit at scales $\sim 20$–$100$ km, and their ratio scales to a good approximation as $(h_e \kappa)^2$, where $h_e$ is effective height, as shown by Schumann, 2019. The effective height is approximately 2–4 km in all models, varying by 1 km between the troposphere and stratosphere. Redefining $h_e$ in terms of IGW properties showed its consistency with variations of the vertical wavelengths estimated from the gravity-wave dispersion relation. These results suggest that the properties of IGWs, namely the dominant vertical wavelength and the intrinsic frequency, control the magnitude of vertical kinetic energy at mesoscales and can be directly inferred from horizontal winds at single levels. This result could be validated since IGW properties can be estimated directly from observations of vertical wind profiles.

   At scales $> 100$ km, the isotropic incompressible scaling $\kappa^2$ breaks, and the magnitude and slope of the vertical kinetic energy are best explained by hydrostatic IGW modes in the mid-frequency limit. The estimates of intrinsic frequency from divergent to rotational IGW energies ratio are consistent with observations Geller and Gong, 2010. These results show that IGWs with frequencies of 1.5–$2.5f$ in the stratosphere and 2–$3f$ in the troposphere could explain vertical

velocity at intermediate scales (100–600 km). It is found that linear gravity wave theory could also predict the shapes and magnitude of the vertical kinetic energy spectrum at synoptic scales. However, as revealed in the analysis, the large-scale maximum of vertical kinetic energy appears consistent with QG scaling. Considering the limitations of linear normal mode decompositions of the atmospheric circulations– it prevents directly quantifying the nonlinear projection of balanced energy onto the IGW modes, our analysis does not allow for a definitive conclusion on the cause of the large-scale peak in the vertical kinetic energy spectrum.

2. **What is the role of resolved IGWs in the energy transfer processes shaping the mesoscale energy spectrum in global storm-resolving simulations?**

The spectral energy budget of the atmosphere investigated in global storm-resolving simulations provides insights into the dominant mechanism shaping the mesoscale spectrum. The analysis shows that the large-scale dynamics are consistent among the simulations and compare favorably with ERA. The analysis of cumulative energy conversions and vertical fluxes within the upper troposphere and the lower stratosphere reveals that these two layers exhibit different dynamics at mesoscales. The lower stratosphere is mainly energized by direct forcing due to vertically propagating IGWs– the models indicate a negligible HKE cascade and only a small direct forcing due to conversion from available potential energy to divergent kinetic energy. The models show similar magnitudes of spectral energy transfer, with vertical fluxes being more important in ICON than the IFS. This difference impacts the resulting energy spectrum, where ICON successfully simulates the observed mesoscale $l^{-5/3}$ spectra, while the IFS spectrum is closer to $l^{-3}$ at mesoscales.

The primary contribution to the kinetic energy spectrum in the troposphere is from spectral transfers redistributing energy across scales. The direct forcing of IGWs on the mesoscale energy spectra in the upper troposphere is limited according to both models. These findings align with Augier and Lindborg (2013), who suggested that the tropospheric mesoscale $l^{-5/3}$ spectrum conforms to predictions based on the presence of a cascade mediated by nonlinear interactions. The decomposition of the spectral energy budget into rotational and divergent components shows that nonlinear interactions of rotational modes dominate the spectral energy transfer. However, it is important to consider the limitations of the Helmholtz decomposition in discerning between different physical processes. The normal mode decomposition of the atmospheric circulation into linear Rossby waves and IGWs suggests that interactions between IGWs and the balanced flow explain the nonlinear downscale energy cascade at mesoscales. This result aligns with the hypotheses that explain the downscale cascade based on triad interactions between vortical and gravity wave modes (Lelong and Riley, 1991; Waite and Bartello, 2006; Kitamura and Matsuda, 2010; Kafiabad et al., 2019). Our results reveal that interacting wave modes do not contribute to the downscale energy transfer, challenging the hypothesis that the downscale cascade is due to weakly nonlinearly interacting IGWs (Dewan, 1979; Smith et al., 1987).

## 5.2 IMPLICATIONS AND OUTLOOK

This dissertation investigated atmospheric energy spectra and the spectral energy budget of global storm-resolving simulations of various state-of-the-art GCMs of the DYAMOND experiment with unprecedented horizontal resolution. The models are, therefore, expected to simulate mesoscale dynamics realistically. The results presented in chapters 3 and 4 highlight the importance of IGWs in shaping the mesoscale energy spectra of horizontal and vertical motions across several horizontal scales. In light of these results, we believe that a detailed analysis of the spectra of the physical tendencies in high-resolution simulations and their impacts on the representation of IGW sources is desirable to elucidate energy transfer between horizontal and vertical motions. Furthermore, as models begin to resolve convective scales explicitly, a moist non-hydrostatic formulation of the spectral energy budget could provide insights into the impact of moist convection on the mesoscale energy spectrum.

The analysis presented here has two main limitations that should be considered in future research. The first relates to the linearity of the Normal Mode decomposition used to determine wave modes from the highly nonlinear and multiscale atmospheric flow, given that nonlinearities can cause vertical motions coupled to the balanced flow that projects onto linear IGW modes. This problem is particularly relevant in the troposphere and at large scales. Future studies of global DYAMOND-like simulations on the impact of gravity waves should incorporate nonlinear corrections into the linear wave-vortex decompositions, as shown by Wang and Bühler (2020). Alternatively, employing Nonlinear Normal Mode methods to discern between balanced and unbalanced dynamics might be valuable to shed light on the dominant mesoscale mechanism. The second limitation relates to the vertical resolution of the simulations studied here, which is hundreds of meters in the upper troposphere and about one kilometer close to the stratosphere. This vertical resolution is insufficient for resolving the vertical structures of gravity waves and strongly stratified turbulence (Augier and Lindborg, 2013), which are the prevailing explanations for mesoscale dynamics. Increasing the vertical resolution is also important for statistical convergence of the atmospheric energy spectra in global simulations (Skamarock et al., 2019).

# ACKNOWLEDGMENTS

# BIBLIOGRAPHY

Alexander, MJ and JR Holton (2004). "On the spectrum of vertically propagating gravity waves generated by a transient heat source." In: *Atmospheric Chemistry and Physics* 4.4, pp. 923–932.

Allen, Simon J. and Robert A. Vincent (1995). "Gravity wave activity in the lower atmosphere: Seasonal and latitudinal variations." In: *Journal of Geophysical Research: Atmospheres* 100.D1, pp. 1327–1350. DOI: `https://doi.org/10.1029/94JD02688`. eprint: `https://agupubs.onlinelibrary.wiley.com/doi/pdf/10.1029/94JD02688`. URL: `https://agupubs.onlinelibrary.wiley.com/doi/abs/10.1029/94JD02688`.

Augier, Pierre and Erik Lindborg (2013). "A New Formulation of the Spectral Energy Budget of the Atmosphere, with Application to Two High-Resolution General Circulation Models." In: *Journal of the Atmospheric Sciences* 70.7, pp. 2293 –2308. DOI: `10.1175/JAS-D-12-0281.1`. URL: `https://journals.ametsoc.org/view/journals/atsc/70/7/jas-d-12-0281.1.xml`.

Bacmeister, Julio T., Stephen D. Eckermann, Paul A. Newman, Leslie Lait, K. Roland Chan, Max Loewenstein, Michael H. Proffitt, and Bruce L. Gary (1996). "Stratospheric horizontal wavenumber spectra of winds, potential temperature, and atmospheric tracers observed by high-altitude aircraft." In: *Journal of Geophysical Research: Atmospheres* 101.D5, pp. 9441–9470. DOI: `https://doi.org/10.1029/95JD03835`. eprint: `https://agupubs.onlinelibrary.wiley.com/doi/pdf/10.1029/95JD03835`. URL: `https://agupubs.onlinelibrary.wiley.com/doi/abs/10.1029/95JD03835`.

Baer, Ferdinand (1972). "An Alternate Scale Representation of Atmospheric Energy Spectra." In: *Journal of Atmospheric Sciences* 29.4, pp. 649 –664. DOI: `10.1175/1520-0469(1972)029<0649:AASROA>2.0.CO;2`. URL: `https://journals.ametsoc.org/view/journals/atsc/29/4/1520-0469_1972_029_0649_aasroa_2_0_co_2.xml`.

Bartello, Peter (1995). "Geostrophic Adjustment and Inverse Cascades in Rotating Stratified Turbulence." In: *Journal of Atmospheric Sciences* 52.24, pp. 4410 –4428. DOI: `10.1175/1520-0469(1995)052<4410:GAAICI>2.0.CO;2`. URL: `https://journals.ametsoc.org/view/journals/atsc/52/24/1520-0469_1995_052_4410_gaaici_2_0_co_2.xml`.

Bierdel, Lotte Beata (June 2017). "On the relevance of rotational and divergent modes of motion to mesoscale dynamics and upscale error growth." URL: `http://nbn-resolving.de/urn:nbn:de:bvb:19-209088`.

Bierdel, Lotte, Chris Snyder, Sang-Hun Park, and William C. Skamarock (2016). "Accuracy of Rotational and Divergent Kinetic Energy Spectra Diagnosed from Flight-Track Winds." In: *Journal of the Atmospheric Sciences* 73.8, pp. 3273 –3286. DOI: `10.1175/JAS-D-16-0040.1`. URL: `https://journals.ametsoc.org/view/journals/atsc/73/8/jas-d-16-0040.1.xml`.

Boer, G. J. and T. G. Shepherd (1983). "Large-Scale Two-Dimensional Turbulence in the Atmosphere." In: *Journal of Atmospheric Sciences* 40.1, pp. 164 –184. DOI: https://doi.org/10.1175/1520-0469(1983)040<0164:LSTDTI>2.0.CO;2. URL: https://journals.ametsoc.org/view/journals/atsc/40/1/1520-0469_1983_040_0164_lstdti_2_0_co_2.xml.

Bony, Sandrine and Bjorn Stevens (2019). "Measuring Area-Averaged Vertical Motions with Dropsondes." In: *Journal of the Atmospheric Sciences* 76.3, pp. 767 –783. DOI: 10.1175/JAS-D-18-0141.1. URL: https://journals.ametsoc.org/view/journals/atsc/76/3/jas-d-18-0141.1.xml.

Burgess, B. H., Andre R. Erler, and Theodore G. Shepherd (2013). "The Troposphere-to-Stratosphere Transition in Kinetic Energy Spectra and Nonlinear Spectral Fluxes as Seen in ECMWF Analyses." In: *Journal of the Atmospheric Sciences* 70.2, pp. 669 –687. DOI: 10.1175/JAS-D-12-0129.1. URL: https://journals.ametsoc.org/view/journals/atsc/70/2/jas-d-12-0129.1.xml.

Businger, Joost A (1973). "Turbulence transfer in the atmospheric surface layer." In: *Workshop on micrometeorology.* Amer. Meteor. Soc., pp. 67–100.

Callies, Jörn, Raffaele Ferrari, and Oliver Bühler (2014). "Transition from geostrophic turbulence to inertia–gravity waves in the atmospheric energy spectrum." In: *Proceedings of the National Academy of Sciences* 111.48, pp. 17033–17038. ISSN: 0027-8424. DOI: 10.1073/pnas.1410772111. eprint: https://www.pnas.org/content/111/48/17033.full.pdf.

Callies, Jörn, Oliver Bühler, and Raffaele Ferrari (2016). "The Dynamics of Mesoscale Winds in the Upper Troposphere and Lower Stratosphere." In: *Journal of the Atmospheric Sciences* 73.12, pp. 4853 –4872. DOI: 10.1175/JAS-D-16-0108.1. URL: https://journals.ametsoc.org/view/journals/atsc/73/12/jas-d-16-0108.1.xml.

Charney, Jule G. (1971). "Geostrophic Turbulence." In: *Journal of Atmospheric Sciences* 28.6, pp. 1087 –1095. DOI: 10.1175/1520-0469(1971)028<1087:GT>2.0.CO;2. URL: https://journals.ametsoc.org/view/journals/atsc/28/6/1520-0469_1971_028_1087_gt_2_0_co_2.xml.

Chen, Tsing-Chang and A. Wiin-nielsen (1975). "On the kinetic energy of the divergent and nondivergent flow in the atmosphere." In: *Tellus A* 28, pp. 486–498.

Cho, John Y. N. and Erik Lindborg (2001). "Horizontal velocity structure functions in the upper troposphere and lower stratosphere: 1. Observations." In: *Journal of Geophysical Research: Atmospheres* 106.D10, pp. 10223–10232. DOI: https://doi.org/10.1029/2000JD900814. eprint: https://agupubs.onlinelibrary.wiley.com/doi/pdf/10.1029/2000JD900814. URL: https://agupubs.onlinelibrary.wiley.com/doi/abs/10.1029/2000JD900814.

Cox, Michael R., Hossein A. Kafiabad, and Jacques Vanneste (2023). "Inertia-gravity-wave diffusion by geostrophic turbulence: the impact of flow time dependence." In: *Journal of Fluid Mechanics* 958, A21. DOI: 10.1017/jfm.2023.83.

Craig, G. C. and T. Selz (2018a). "Mesoscale Dynamical Regimes in the Midlatitudes." In: *Geophysical Research Letters* 45.1, pp. 410–417. DOI: https://doi.org/10.1002/2017GL076174. eprint: https://agupubs.onlinelibrary.wiley.com/doi/pdf/10.1002/2017GL076174. URL: https://agupubs.onlinelibrary.wiley.com/doi/abs/10.1002/2017GL076174.

Craig, G. C. and T. Selz (2018b). "Mesoscale Dynamical Regimes in the Midlatitudes." In: *Geophysical Research Letters* 45.1, pp. 410–417. DOI: https://doi.org/10.1002/2017GL076174.

Dewan, E. M. (1979). "Stratospheric Wave Spectra Resembling Turbulence." In: *Science* 204.4395, pp. 832–835. ISSN: 0036-8075. DOI: 10.1126/science.204.4395.832. eprint: https://science.sciencemag.org/content/204/4395/832.full.pdf.

Dewan, E. M. (1997). "Saturated-cascade similitude theory of gravity wave spectra." In: *Journal of Geophysical Research: Atmospheres* 102.D25, pp. 29799–29817. DOI: https://doi.org/10.1029/97JD02151. eprint: https://agupubs.onlinelibrary.wiley.com/doi/pdf/10.1029/97JD02151.

Dewan, E. M. and R. E. Good (1986). "Saturation and the "universal" spectrum for vertical profiles of horizontal scalar winds in the atmosphere." In: *Journal of Geophysical Research: Atmospheres* 91.D2, pp. 2742–2748. DOI: https://doi.org/10.1029/JD091iD02p02742. eprint: https://agupubs.onlinelibrary.wiley.com/doi/pdf/10.1029/JD091iD02p02742. URL: https://agupubs.onlinelibrary.wiley.com/doi/abs/10.1029/JD091iD02p02742.

Dritschel, David G. and William J. McKiver (2015). "Effect of Prandtl's ratio on balance in geophysical turbulence." In: *Journal of Fluid Mechanics* 777, 569–590. DOI: 10.1017/jfm.2015.348.

ECMWF (Oct. 2021). "IFS Documentation CY47R3 - Part III Dynamics and numerical procedures." In: *IFS Documentation CY47R3*. IFS Documentation 3. ECMWF. DOI: 10.21957/b18qsx663. URL: https://www.ecmwf.int/node/20197.

Ecklund, W. L., K. S. Gage, G. D. Nastrom, and B. B. Balsley (1986). "A Preliminary Climatology of the Spectrum of Vertical Velocity Observed by Clear-Air Doppler Radar." In: *Journal of Applied Meteorology and Climatology* 25.7, pp. 885 –892. DOI: https://doi.org/10.1175/1520-0450(1986)025<0885:APCOTS>2.0.CO;2. URL: https://journals.ametsoc.org/view/journals/apme/25/7/1520-0450_1986_025_0885_apcots_2_0_co_2.xml.

Fritts, David C. (1984). "Gravity wave saturation in the middle atmosphere: A review of theory and observations." In: *Reviews of Geophysics* 22.3, pp. 275–308. DOI: https://doi.org/10.1029/RG022i003p00275. eprint: https://agupubs.onlinelibrary.wiley.com/doi/pdf/10.1029/RG022i003p00275. URL: https://agupubs.onlinelibrary.wiley.com/doi/abs/10.1029/RG022i003p00275.

Fritts, David C. and M. Joan Alexander (2003). "Gravity wave dynamics and effects in the middle atmosphere." In: *Reviews of Geophysics* 41.1. DOI: https://doi.org/10.1029/2001RG000106. eprint: https://agupubs.onlinelibrary.wiley.com/doi/pdf/10.1029/2001RG000106. URL: https://agupubs.onlinelibrary.wiley.com/doi/abs/10.1029/2001RG000106.

Gage, K. S. (Oct. 1979). "Evidence for a k to the -5/3 law inertial range in mesoscale two-dimensional turbulence." In: *Journal of Atmospheric Sciences* 36, pp. 1950–1954. DOI: 10.1175/1520-0469(1979)036\textless5{}1950:EFALIR\textgreater{}2.0.CO;2.

Gao, X. and J. W. Meriwether (1998). "Mesoscale spectral analysis of in situ horizontal and vertical wind measurements at 6 km." In: *Journal of Geophysical Research: Atmospheres* 103.D6, pp. 6397–6404. DOI: https://doi.org/10.1029/97JD03074. eprint: https://agupubs.onlinelibrary.wiley.com/doi/pdf/10.1029/97JD03074. URL: https://agupubs.onlinelibrary.wiley.com/doi/abs/10.1029/97JD03074.

Gardner, Chester S. (1996). "Testing theories of atmospheric gravity wave saturation and dissipation." In: *Journal of Atmospheric and Terrestrial Physics* 58.14. Invited Review Articles from the 1995 CEDAR Workshop, pp. 1575–1589. ISSN: 0021-9169. DOI: https://doi.org/10.1016/0021-9169(96)00027-X. URL: https://www.sciencedirect.com/science/article/pii/002191699600027X.

Gardner, Chester S., Steven J. Franke, Weimin Yang, Xin Tao, and J. R. Yu (1998). "Interpretation of gravity waves observed in the mesopause region at Starfire Optical Range, New Mexico: Strong evidence for nonseparable intrinsic (m, w) spectra." In: *Journal of Geophysical Research: Atmospheres* 103.D8, pp. 8699–8713. DOI: https://doi.org/10.1029/97JD03428. eprint: https://agupubs.onlinelibrary.wiley.com/doi/pdf/10.1029/97JD03428. URL: https://agupubs.onlinelibrary.wiley.com/doi/abs/10.1029/97JD03428.

Geller, Marvin A. and Jie Gong (2010). "Gravity wave kinetic, potential, and vertical fluctuation energies as indicators of different frequency gravity waves." In: *Journal of Geophysical Research: Atmospheres* 115.D11. DOI: https://doi.org/10.1029/2009JD012266. eprint: https://agupubs.onlinelibrary.wiley.com/doi/pdf/10.1029/2009JD012266. URL: https://agupubs.onlinelibrary.wiley.com/doi/abs/10.1029/2009JD012266.

George, Geet, Bjorn Stevens, Sandrine Bony, Marcus Klingebiel, and Raphaela Vogel (2021). "Observed Impact of Mesoscale Vertical Motion on Cloudiness." In: *Journal of the Atmospheric Sciences* 78.8, pp. 2413 –2427. DOI: 10.1175/JAS-D-20-0335.1. URL: https://journals.ametsoc.org/view/journals/atsc/78/8/JAS-D-20-0335.1.xml.

Hamilton, Kevin, Yoshiyuki O. Takahashi, and Wataru Ohfuchi (2008). "Mesoscale spectrum of atmospheric motions investigated in a very fine resolution global general circulation model." In: *Journal of Geophysical Research: Atmospheres* 113.D18. DOI: https://doi.org/10.1029/2008JD009785. eprint: https://agupubs.onlinelibrary.wiley.com/doi/pdf/10.1029/2008JD009785. URL: https://agupubs.onlinelibrary.wiley.com/doi/abs/10.1029/2008JD009785.

Holton, JR, JH Beres, and X Zhou (2002). "On the vertical scale of gravity waves excited by localized thermal forcing." In: *Journal of the atmospheric sciences* 59.12, pp. 2019–2023.

Holton, James R. (2004). *An introduction to dynamic meteorology.* Ed. by Renata Dmowska and James R. Holton. 4th ed. International Geophysics Series. Burlington, MA: Elsevier Academic Press, p. 535. ISBN: 9780123540157.

Kafiabad, Hossein A., Miles A. C. Savva, and Jacques Vanneste (2019). "Diffusion of inertia-gravity waves by geostrophic turbulence." In: *Journal of Fluid Mechanics* 869, R7. DOI: 10.1017/jfm.2019.300.

Kasahara, A. (2020). *3D Normal Mode Functions (NMFs) of a Global Baroclinic Atmospheric Model.* Modal View Of Atmospheric Variability: Applications Of Normal-Mode Function Decomposition in Weather and Climate Research. N. Žagar and J. Tribbia, Eds., Springer, Mathematics of Planet Earth Series, Vol.8.

Kasahara, A. and K. Puri (1981). "Spectral representation of three-dimensional global data by expansion in normal mode functions." In: *Mon. Wea. Rev.* 109, pp. 37–51. DOI: 10.1175/1520-0493(1981)109<0037:SROTDG>2.0.CO;2.

Kitamura, Y. and Y. Matsuda (2010). "Energy cascade processes in rotating stratified turbulence with application to the atmospheric mesoscale." In: *Journal of Geophysical Research: Atmospheres* 115.D11. DOI: https://doi.org/10.1029/2009JD012368.

eprint: `https : / / agupubs . onlinelibrary . wiley . com / doi / pdf / 10 . 1029 / 2009JD012368`. URL: `https://agupubs.onlinelibrary.wiley.com/doi/abs/ 10.1029/2009JD012368`.

Klocke, Daniel, Matthias Brueck, Cathy Hohenegger, and Bjorn Stevens (Dec. 2017). "Rediscovery of the doldrums in storm-resolving simulations over the tropical Atlantic." In: *Nature Geoscience* 10.12, pp. 891–896. ISSN: 1752-0908. DOI: `10.1038/ s41561-017-0005-4`. URL: `https://doi.org/10.1038/s41561-017-0005-4`.

Kolmogorov, A. (Jan. 1941). "The Local Structure of Turbulence in Incompressible Viscous Fluid for Very Large Reynolds' Numbers." In: *Akademiia Nauk SSSR Doklady* 30, pp. 301–305.

Koshyk, J., K. Hamilton, and J. Mahlman (1999). "Simulation of the k-5/3 mesoscale spectral regime in the GFDL SKYHI general circulation model." In.

Lambert, Steven J. (1984). "A global available potential energy-kinetic energy budget in terms of the two-dimensional wavenumber for the FGGE year." In: *Atmosphere-Ocean* 22.3, pp. 265–282. DOI: `10.1080/07055900.1984.9649199`.

Lelong, M-Pascale and James J Riley (1991). "Internal wave—vortical mode interactions in strongly stratified flows." In: *Journal of Fluid Mechanics* 232, pp. 1–19.

Li, Qiang and Erik Lindborg (2018). "Weakly or Strongly Nonlinear Mesoscale Dynamics Close to the Tropopause?" In: *Journal of the Atmospheric Sciences* 75.4, pp. 1215 –1229. DOI: `10.1175/JAS-D-17-0063.1`. URL: `https://journals. ametsoc.org/view/journals/atsc/75/4/jas-d-17-0063.1.xml`.

Li, Zongheng, Jun Peng, and Lifeng Zhang (2023). "Spectral Budget of Rotational and Divergent Kinetic Energy in Global Analyses." In: *Journal of the Atmospheric Sciences* 80.3, pp. 813 –831. DOI: `https://doi.org/10.1175/JAS-D-21-0332.1`. URL: `https://journals.ametsoc.org/view/journals/atsc/80/3/JAS-D-21- 0332.1.xml`.

Lilly, D. (1983). "Stratified Turbulence and the Mesoscale Variability of the Atmosphere." In: *Journal of the Atmospheric Sciences* 40, pp. 749–761.

Lindborg, Erik (1999). "Can the atmospheric kinetic energy spectrum be explained by two-dimensional turbulence?" In: *Journal of Fluid Mechanics* 388, 259–288. DOI: `10.1017/S0022112099004851`.

Lindborg, Erik (2006). "The energy cascade in a strongly stratified fluid." In: *Journal of Fluid Mechanics* 550, 207–242. DOI: `10.1017/S0022112005008128`.

Lindborg, Erik (2015). "A Helmholtz decomposition of structure functions and spectra calculated from aircraft data." In: *Journal of Fluid Mechanics* 762, R4. DOI: `10. 1017/jfm.2014.685`.

Lorenz, E. N. (1969). "The predictability of a flow which possesses many scales of motion." In: *Tellus* 21.3, pp. 289–307. DOI: `https://doi.org/10.1111/j.2153- 3490.1969.tb00444.x`.

Lorenz, Edward N. (1955). "Available Potential Energy and the Maintenance of the General Circulation." In: *Tellus* 7.2, pp. 157–167. DOI: `https://doi.org/ 10 . 1111 / j . 2153 - 3490 . 1955 . tb01148 . x`. eprint: `https : / / onlinelibrary . wiley.com/doi/pdf/10.1111/j.2153-3490.1955.tb01148.x`. URL: `https:// onlinelibrary.wiley.com/doi/abs/10.1111/j.2153-3490.1955.tb01148.x`.

Lorenz, Edward N. (1960). "Energy and Numerical Weather Prediction." In: *Tellus* 12.4, pp. 364–373. DOI: `https://doi.org/10.1111/j.2153-3490.1960.tb01323.x`. eprint: `https://onlinelibrary.wiley.com/doi/pdf/10.1111/j.2153-3490.`

1960.tb01323.x. URL: https://onlinelibrary.wiley.com/doi/abs/10.1111/
j.2153-3490.1960.tb01323.x.

Malardel, Sylvie and Nils P. Wedi (2016). "How does subgrid-scale parametrization influence nonlinear spectral energy fluxes in global NWP models?" In: *Journal of Geophysical Research: Atmospheres* 121.10, pp. 5395–5410. DOI: https://doi.org/10.1002/2015JD023970. eprint: https://agupubs.onlinelibrary.wiley.com/doi/pdf/10.1002/2015JD023970. URL: https://agupubs.onlinelibrary.wiley.com/doi/abs/10.1002/2015JD023970.

Marques, C. A. F. and J. M. Castanheira (2012). "A Detailed Normal-Mode Energetics of the General Circulation of the Atmosphere." In: *Journal of the Atmospheric Sciences* 69.9, pp. 2718–2732. DOI: https://doi.org/10.1175/JAS-D-11-0324.1. URL: https://journals.ametsoc.org/view/journals/atsc/69/9/jas-d-11-0324.1.xml.

McIntyre, M. E. (2008). "Potential-vorticity inversion and the wave-turbulence jigsaw: some recent clarifications." In: *Advances in Geosciences* 15, pp. 47–56. DOI: 10.5194/adgeo-15-47-2008. URL: https://adgeo.copernicus.org/articles/15/47/2008/.

McIntyre, M.E. (2015). "DYNAMICAL METEOROLOGY | Balanced Flow." In: *Encyclopedia of Atmospheric Sciences (Second Edition)*. Ed. by Gerald R. North, John Pyle, and Fuqing Zhang. Second Edition. Oxford: Academic Press, pp. 298–303. ISBN: 978-0-12-382225-3. DOI: https://doi.org/10.1016/B978-0-12-382225-3.00484-9. URL: https://www.sciencedirect.com/science/article/pii/B9780123822253004849.

Morfa, Yanmichel A. and Claudia C. Stephan (2023). "The Relationship between Horizontal and Vertical Velocity Wavenumber Spectra in Global Storm-Resolving Simulations." In: *Journal of the Atmospheric Sciences* 80.4, pp. 1087–1105. DOI: https://doi.org/10.1175/JAS-D-22-0105.1. URL: https://journals.ametsoc.org/view/journals/atsc/80/4/JAS-D-22-0105.1.xml.

Müller, S. K., Elisa Manzini, Marco Giorgetta, Kaoru Sato, and Tomoe Nasuno (2018). "Convectively Generated Gravity Waves in High Resolution Models of Tropical Dynamics." In: *Journal of Advances in Modeling Earth Systems* 10.10, pp. 2564–2588. DOI: https://doi.org/10.1029/2018MS001390. eprint: https://agupubs.onlinelibrary.wiley.com/doi/pdf/10.1029/2018MS001390.

Nastrom, G. D. and K. S. Gage (1985). "A Climatology of Atmospheric Wavenumber Spectra of Wind and Temperature Observed by Commercial Aircraft." In: *Journal of Atmospheric Sciences* 9.42, pp. 950–960.

Nastrom, G. D., K. S. Gage, and W. H. Jasperson (July 1984). "Kinetic energy spectrum of large-and mesoscale atmospheric processes." In: *Nature* 310.5972, pp. 36–38. ISSN: 1476-4687. DOI: 10.1038/310036a0.

Peltier, L. J., J. C. Wyngaard, S. Khanna, and J. O. Brasseur (1996). "Spectra in the Unstable Surface Layer." In: *Journal of Atmospheric Sciences* 53.1, pp. 49–61. DOI: 10.1175/1520-0469(1996)053<0049:SITUSL>2.0.CO;2. URL: https://journals.ametsoc.org/view/journals/atsc/53/1/1520-0469_1996_053_0049_situsl_2_0_co_2.xml.

Polichtchouk, Inna, Nils Wedi, and Young-Ha Kim (2022). "Resolved gravity waves in the tropical stratosphere: Impact of horizontal resolution and deep convection parametrization." In: *Quarterly Journal of the Royal Meteorological Society* 148.742, pp. 233–251. DOI: https://doi.org/10.1002/qj.4202. eprint: https://

rmets.onlinelibrary.wiley.com/doi/pdf/10.1002/qj.4202. URL: https://rmets.onlinelibrary.wiley.com/doi/abs/10.1002/qj.4202.

Putman, William M. and Max Suarez (2011). "Cloud-system resolving simulations with the NASA Goddard Earth Observing System global atmospheric model (GEOS-5)." In: *Geophysical Research Letters* 38.16. DOI: https://doi.org/10.1029/2011GL048438. eprint: https://agupubs.onlinelibrary.wiley.com/doi/pdf/10.1029/2011GL048438. URL: https://agupubs.onlinelibrary.wiley.com/doi/abs/10.1029/2011GL048438.

Satoh, M., T. Matsuno, H. Tomita, H. Miura, T. Nasuno, and S. Iga (2008). "Non-hydrostatic icosahedral atmospheric model (NICAM) for global cloud resolving simulations." In: *Journal of Computational Physics* 227.7. Predicting weather, climate and extreme events, pp. 3486–3514. ISSN: 0021-9991. DOI: https://doi.org/10.1016/j.jcp.2007.02.006. URL: https://www.sciencedirect.com/science/article/pii/S0021999107000654.

Schaeffer, Nathanaël (2013). "Efficient spherical harmonic transforms aimed at pseudospectral numerical simulations." In: *Geochemistry, Geophysics, Geosystems* 14.3, pp. 751–758. DOI: https://doi.org/10.1002/ggge.20071. eprint: https://agupubs.onlinelibrary.wiley.com/doi/pdf/10.1002/ggge.20071. URL: https://agupubs.onlinelibrary.wiley.com/doi/abs/10.1002/ggge.20071.

Schumann, U. (2019). "The Horizontal Spectrum of Vertical Velocities near the Tropopause from Global to Gravity Wave Scales." In: *Journal of the Atmospheric Sciences* 76, pp. 3847–3862.

Selz, Tobias, Lotte Bierdel, and George C. Craig (2019). "Estimation of the Variability of Mesoscale Energy Spectra with Three Years of COSMO-DE Analyses." In: *Journal of the Atmospheric Sciences* 76.2, pp. 627 –637. DOI: 10.1175/JAS-D-18-0155.1.

Shutts, Glenn (2005). "A kinetic energy backscatter algorithm for use in ensemble prediction systems." In: *Quarterly Journal of the Royal Meteorological Society* 131.612, pp. 3079–3102. DOI: https://doi.org/10.1256/qj.04.106. eprint: https://rmets.onlinelibrary.wiley.com/doi/pdf/10.1256/qj.04.106. URL: https://rmets.onlinelibrary.wiley.com/doi/abs/10.1256/qj.04.106.

Simmons, A. J. and D. M. Burridge (1981). "An Energy and Angular-Momentum Conserving Vertical Finite-Difference Scheme and Hybrid Vertical Coordinates." In: *Monthly Weather Review* 109.4, pp. 758 –766. DOI: 10.1175/1520-0493(1981)109<0758:AEAAMC>2.0.CO;2. URL: https://journals.ametsoc.org/view/journals/mwre/109/4/1520-0493_1981_109_0758_aeaamc_2_0_co_2.xml.

Skamarock, William C. (2004). "Evaluating Mesoscale NWP Models Using Kinetic Energy Spectra." In: *Monthly Weather Review* 132.12, pp. 3019 –3032. DOI: 10.1175/MWR2830.1.

Skamarock, William C. and Joseph B. Klemp (2008). "A time-split nonhydrostatic atmospheric model for weather research and forecasting applications." In: *Journal of Computational Physics* 227.7. Predicting weather, climate and extreme events, pp. 3465–3485. ISSN: 0021-9991. DOI: https://doi.org/10.1016/j.jcp.2007.01.037. URL: https://www.sciencedirect.com/science/article/pii/S0021999107000459.

Skamarock, William C., Sang-Hun Park, Joseph B. Klemp, and Chris Snyder (2014). "Atmospheric Kinetic Energy Spectra from Global High-Resolution Nonhydrostatic Simulations." In: *Journal of the Atmospheric Sciences* 71.11, pp. 4369 –4381. DOI: 10.1175/JAS-D-14-0114.1.

Skamarock, William C., Chris Snyder, Joseph B. Klemp, and Sang-Hun Park (2019). "Vertical Resolution Requirements in Atmospheric Simulation." In: *Monthly Weather Review* 147.7, pp. 2641 –2656. DOI: 10.1175/MWR-D-19-0043.1. URL: https://journals.ametsoc.org/view/journals/mwre/147/7/mwr-d-19-0043.1.xml.

Smith, Steven, David Fritts, and Thomas Vanzandt (June 1987). "Evidence for a Saturated Spectrum of Atmospheric Gravity Waves." In: *Journal of the Atmospheric Sciences* 44. DOI: 10.1175/1520-0469(1987)044<1404:EFASSO>2.0.CO;2.

Stephan, C. C. and A. Mariaccia (2021a). "The signature of the tropospheric gravity wave background in observed mesoscale motion." In: *Weather and Climate Dynamics* 2.2, pp. 359–372. DOI: 10.5194/wcd-2-359-2021. URL: https://wcd.copernicus.org/articles/2/359/2021/.

Stephan, C. C. and A. Mariaccia (2021b). "The signature of the tropospheric gravity wave background in observed mesoscale motion." In: *Weather and Climate Dynamics* 2.2, pp. 359–372. DOI: 10.5194/wcd-2-359-2021. URL: https://wcd.copernicus.org/articles/2/359/2021/.

Stephan, C. C., S. Schnitt, H. Schulz, H. Bellenger, S. P. de Szoeke, C. Acquistapace, et al. (2021a). "Ship- and island-based atmospheric soundings from the 2020 EUREC$^4$A field campaign." In: *Earth System Science Data* 13.2, pp. 491–514. DOI: 10.5194/essd-13-491-2021. URL: https://essd.copernicus.org/articles/13/491/2021/.

Stephan, C.C., J. Duras, L. Harris, D. Klocke, W.M. Putman, M. Taylor, N.P. Wedi, N. Žagar, and F. Ziemen (2022). "Atmospheric Energy Spectra in Global Kilometre-Scale Models." In: *Tellus A: Dynamic Meteorology and Oceanography* 74, 280 – 299. DOI: 10.16993/tellusa.26.

Stephan, Claudia C., Nedjeljka Žagar, and Theodore G. Shepherd (2021b). "Waves and coherent flows in the tropical atmosphere: New opportunities, old challenges." In: *Quarterly Journal of the Royal Meteorological Society* 147.738, pp. 2597–2624. DOI: https://doi.org/10.1002/qj.4109. eprint: https://rmets.onlinelibrary.wiley.com/doi/pdf/10.1002/qj.4109. URL: https://rmets.onlinelibrary.wiley.com/doi/abs/10.1002/qj.4109.

Stevens, B., S. Bony, D. Farrell, F. Ament, A. Blyth, C. Fairall, et al. (2021). "EUREC$^4$A." In: *Earth System Science Data* 13.8, pp. 4067–4119. DOI: 10.5194/essd-13-4067-2021. URL: https://essd.copernicus.org/articles/13/4067/2021/.

Stevens, Bjorn, Masaki Satoh, Ludovic Auger, Joachim Biercamp, Christopher S. Bretherton, Xi Chen, et al. (Sept. 2019). "DYAMOND: the DYnamics of the Atmospheric general circulation Modeled On Non-hydrostatic Domains." In: *Progress in Earth and Planetary Science* 6.1, p. 61. ISSN: 2197-4284. DOI: 10.1186/s40645-019-0304-z.

Tanaka, Hiroshi (1985). "Global energetics analysis by expansion into three-dimensional normal mode functions during the FGGE winter." In: *Journal of the Meteorological Society of Japan. Ser. II* 63.2, pp. 180–200.

Terasaki, K., H. Tanaka, and M. Satoh (2009). "Characteristics of the Kinetic Energy Spectrum of NICAM Model Atmosphere." In: *Sola* 5, pp. 180–183.

Terasaki, K., H. Tanaka, and N. Žagar (2011). "Erratum: Energy spectra of Rossby and gravity waves." In: *SOLA* 7, pp. 45–48.

Tong, Chenning and Khuong X. Nguyen (2015). "Multipoint Monin–Obukhov Similarity and Its Application to Turbulence Spectra in the Convective Atmospheric

Surface Layer." In: *Journal of the Atmospheric Sciences* 72.11, pp. 4337 –4348. DOI: 10.1175/JAS-D-15-0134.1. URL: https://journals.ametsoc.org/view/journals/atsc/72/11/jas-d-15-0134.1.xml.

Tung, Ka Kit and Wendell Welch Orlando (2003). "The k-3 and k-5/3 Energy Spectrum of Atmospheric Turbulence: Quasigeostrophic Two-Level Model Simulation." In: *Journal of the Atmospheric Sciences* 60.6, pp. 824 –835. DOI: 10.1175/1520-0469(2003)060<0824:TKAKES>2.0.CO;2.

Untch, A. and M. Hortal (Apr. 2003). "A finite-element scheme for the vertical descretization in the semi-Lagrangian version of the ECMWF model." In: 382, p. 27. DOI: 10.21957/h70dda68e. URL: https://www.ecmwf.int/node/12873.

VanZandt, T. E. (1982). "A universal spectrum of buoyancy waves in the atmosphere." In: *Geophysical Research Letters* 9.5, pp. 575–578. DOI: https://doi.org/10.1029/GL009i005p00575. eprint: https://agupubs.onlinelibrary.wiley.com/doi/pdf/10.1029/GL009i005p00575.

Vogel, Raphaela, Sandrine Bony, and Bjorn Stevens (2020). "Estimating the Shallow Convective Mass Flux from the Subcloud-Layer Mass Budget." In: *Journal of the Atmospheric Sciences* 77, pp. 1559–1574. URL: https://api.semanticscholar.org/CorpusID:197504244.

Waite, MICHAEL L. and PETER Bartello (2004). "Stratified turbulence dominated by vortical motion." In: *Journal of Fluid Mechanics* 517, 281–308. DOI: 10.1017/S0022112004000977.

Waite, MICHAEL L. and PETER Bartello (2006). "Stratified turbulence generated by internal gravity waves." In: *Journal of Fluid Mechanics* 546, 313–339. DOI: 10.1017/S0022112005007111.

Waite, Michael L. (2016). "Dependence of Model Energy Spectra on Vertical Resolution." In: *Monthly Weather Review* 144.4, pp. 1407 –1421. DOI: 10.1175/MWR-D-15-0316.1.

Waite, Michael L. (2020). "Untangling waves and vortices in the atmospheric kinetic energy spectra." In: *Journal of Fluid Mechanics* 888, F1. DOI: 10.1017/jfm.2019.1060.

Waite, Michael L. and Chris Snyder (2013). "Mesoscale Energy Spectra of Moist Baroclinic Waves." In: *Journal of the Atmospheric Sciences* 70.4, pp. 1242 –1256. DOI: 10.1175/JAS-D-11-0347.1. URL: https://journals.ametsoc.org/view/journals/atsc/70/4/jas-d-11-0347.1.xml.

Wang, Han and Oliver Bühler (2020). "Ageostrophic corrections for power spectra and wave–vortex decomposition." In: *Journal of Fluid Mechanics* 882, A16. DOI: 10.1017/jfm.2019.815.

Wang, Shihong, Zhiliang Liu, and Chongguang Pang (2015). "Geographical distribution and anisotropy of the inverse kinetic energy cascade, and its role in the eddy equilibrium processes." In: *Journal of Geophysical Research: Oceans* 120.7, pp. 4891–4906. DOI: https://doi.org/10.1002/2014JC010476. eprint: https://agupubs.onlinelibrary.wiley.com/doi/pdf/10.1002/2014JC010476. URL: https://agupubs.onlinelibrary.wiley.com/doi/abs/10.1002/2014JC010476.

Wedi, Nils P. (2014). "Increasing horizontal resolution in numerical weather prediction and climate simulations: illusion or panacea?" In: *Philosophical Transactions of the Royal Society A: Mathematical, Physical and Engineering Sciences* 372.2018, p. 20130289. DOI: 10.1098/rsta.2013.0289. eprint: https://

royalsocietypublishing.org/doi/pdf/10.1098/rsta.2013.0289. URL: https://royalsocietypublishing.org/doi/abs/10.1098/rsta.2013.0289.

Young, William R. (2021). "Inertia-gravity waves and geostrophic turbulence." In: *Journal of Fluid Mechanics* 920, F1. DOI: 10.1017/jfm.2021.334.

Zhang, S. D., C. M. Huang, K. M. Huang, Y. H. Zhang, Y. Gong, and Q. Gan (2017). "Vertical wavenumber spectra of three-dimensional winds revealed by radiosonde observations at midlatitude." In: *Annales Geophysicae* 35.1, pp. 107–116. DOI: 10.5194/angeo-35-107-2017. URL: https://angeo.copernicus.org/articles/35/107/2017/.

Zängl, Günther, Daniel Reinert, Pilar Rípodas, and Michael Baldauf (2015). "The ICON (ICOsahedral Non-hydrostatic) modelling framework of DWD and MPI-M: Description of the non-hydrostatic dynamical core." In: *Quarterly Journal of the Royal Meteorological Society* 141.687, pp. 563–579. DOI: https://doi.org/10.1002/qj.2378. eprint: https://rmets.onlinelibrary.wiley.com/doi/pdf/10.1002/qj.2378. URL: https://rmets.onlinelibrary.wiley.com/doi/abs/10.1002/qj.2378.

Žagar, N., A. Kasahara, K. Terasaki, J. Tribbia, and H. Tanaka (2015). "Normal-mode function representation of global 3-D data sets: open-access software for the atmospheric research community." In: *Geoscientific Model Development* 8.4, pp. 1169–1195. DOI: 10.5194/gmd-8-1169-2015. URL: https://gmd.copernicus.org/articles/8/1169/2015/.

Žagar, Nedjeljka, Damjan Jelić, Marten Blaauw, and Peter Bechtold (2017). "Energy Spectra and Inertia–Gravity Waves in Global Analyses." In: *Journal of the Atmospheric Sciences* 74.8, pp. 2447 –2466. DOI: 10.1175/JAS-D-16-0341.1. URL: https://journals.ametsoc.org/view/journals/atsc/74/8/jas-d-16-0341.1.xml.

# EIDESSTATTLICHE VERSICHERUNG

Hiermit erkläre ich an Eides statt, dass ich die vorliegende Dissertationsschrift selbst verfasst und keine anderen als die angegebenen Quellen und Hilfsmittel benutzt habe.

I hereby declare upon oath that I have written the present dissertation independently and have not used further resources and aids than those stated.

*Hamburg, August 2023*

Yanmichel Alejandro Morfa Avalos

# Hinweis / Reference

Die gesamten Veröffentlichungen in der Publikationsreihe des MPI-M
„Berichte zur Erdsystemforschung / Reports on Earth System Science",
ISSN 1614-1199

sind über die Internetseiten des Max-Planck-Instituts für Meteorologie erhältlich:
**https://mpimet.mpg.de/forschung/publikationen**

*All the publications in the series of the MPI -M*
*„Berichte zur Erdsystemforschung / Reports on Earth System Science",*
*ISSN 1614-1199*

*are available on the website of the Max Planck Institute for Meteorology:*
***https://mpimet.mpg.de/en/research/publications***